Estimation Method of Sea Spray Concentration and Evaluation of Momentum Transfer at the Sea Surface Under Stormy Conditions

Hiroki Okachi

Graduate School of Engineering

Hokkaido University

A thesis submitted for the degree of

Doctor of Philosophy

2021 September

In recent years, Japan has experienced frequent river flooding and landslide disasters caused by heavy rainfall brought by typhoons. Typhoons also cause storm surges and salt damage. As progress of climate change, the location of typhoon genesis in the Northwest Pacific Ocean is predicted to shift toward the northeast. Also, a decrease in central pressure of typhoon and an increase in wind speed and rainfall caused by typhoon are projected. These projections mean that stronger typhoon generates near Japan area. One of the important factors to predict typhoon strength is friction between the air and sea, which is described by drag coefficient. To achieve disaster mitigation, more accurate prediction of typhoon strength is required in the future projection that typhoon will become stronger.

The drag coefficient can be estimated by observing the vertical distribution of horizontal wind speed. However, there are few cases of observations under typhoons, and the drag coefficient under high wind conditions has not been settled yet, although many studies have been conducted. This study consists of field observations, tunnel experiments and numerical simulations of the surface layer of the atmosphere including sea spray generated from breaking waves, under typhoon conditions and analytical methods. The vertical profiles of sea spray concentrations and horizontal wind speeds were estimated from the observations using ship radar and other instruments. This will contribute to the understanding of the interaction between the air and sea under storm conditions.

In Chapter 2, the author summarizes the previous studies on friction between the sea surface and the air under typhoons with various wind speeds and rainfall intensities. It is suggested that the drag coefficient may increases or decreases due to the effects of wind speed, waves, sea sprays and raindrops near the sea surface. The effect of wind speed, waves, droplets, and raindrops on the drag coefficient was examined, and the results showed that rainfall also had certain effects on the drag coefficient. However, the concentration of sea spray distributed on the sea surface is still not sufficiently known. Therefore, in the next chapter, the author conducted the observation of sea spray in the field.

In Chapter 3, the author conducted field observations at the observation tower of Shirahama Oceanographic Observatory, located 1.8 km off the coast

of Wakayama Prefecture, using a disdrometer, anemometer, and wave height meter. The disdrometer can detect particles with a diameter of less than 1 mm. The instruments were installed at a height of 15 m in the observation tower, and the observation of strong wind events without rainfall was collected. The number density of sea spray as a function of the wind speed was formulated.

In Chapter 4, observations of sea spray and rain using a radar capable of observing vertical cross-section with high spatio-temporal resolution were achieved for typhoon events that passed near the observation sites, such as typhoons 20, 21, and 24 (CIMARON, JEBE, and TRAMI) in 2018. The radar measured the event when the 10-minute averaged wind speed is 39.5 ms^{-1} during these events. Detailed information about advections of sea spray and rain distributed near the sea surface during extreme wind conditions was obtained. In this chapter, the author propose a method to convert the radar images into backscattering radar cross sections, which is a physical quantity that represents the properties of sea spray and rainfall to electromagnetic waves. Specifically, the method extracts the time when the wind direction coincides with the radar observation direction, removes noise, converts the image to received power, corrects the electromagnetic attenuation according to the distance, and estimates the radar gain by calibration using nearby meteorological radar. The vertical distribution of the horizontal wind speed was estimated from the horizontal movement speed of rain and sea spray observed by the radar, hypothesizing that the horizontal wind speed to be similar to horizontal velocity of rain and sea spray. The drag coefficient was estimated from the vertical profile of the horizontal wind speed.

In Chapter 5, the author proposed a method for estimating the number density and mass concentration of sea spray with respect to their drop size using the results of backscattering radar cross sections obtained in Chapter 4. The method represents the scattering by multiple particles in a unit volume (volume scattering) by combining individual scattering in a unit volume expressed by Mie scattering theory. It is shown that the existing mass concentration distribution equation for suspended sediment can be applied to the obtained vertical distribution of mass concentration of sea spray. At the same time, this thesis proposes an equation for the vertical distribution of mass concentration of droplets depending on the wind speed. Furthermore, by using the vertical distribution of the mass

concentration, the amount of droplets generated from the sea surface, which cannot be captured by radar due to sea clutter, is estimated and shown as a function of wind speed.

In this thesis, detailed quantitative information on the mixed conditions of sea spray and rain on the sea surface was generated. This thesis highlights the potential of using radar observation to obtain method for estimating the vertical distribution of wind speed and the vertical distribution of sea spray mass concentration. It will lead us to derive a new parameterization of drag coefficient, and hence provide highly significant information on detailed spatial distribution of multi-phase flow with sea spray and rain in the surface boundary layer. This line of investigation could improve the understanding of the vertical distribution of wind speed and the vertical distribution of sea spray mass concentration under strong wind conditions like typhoons.

Acknowledgements

The study presented in this thesis has been performed under the direction of Associate Professor Tomohito Yamada, Faculty of Engineering, Hokkaido University.

I would like to express my appreciation to him for thinking, analyzing, re-analyzing my results, teaching, expressing his unbiased opinions and engaging in comprehensive discussions during my PhD program. His continuous guidance and instructions, encouragement and invaluable suggestions for this study and for my life my 6 years and more stay in this laboratory made me passionate for research in civil engineering field. This journey is very long and hard but my respected supervisor Associate Professor Tomohito Yamada introduced me to many opportunities arousing curiosity in me to think about civil engineering for benefit of human society. The joy to pursue my research and the excitement to learn from the peer group during my stay in the laboratory shaped my personality as a young researcher. I would like to thank Associate Professor Tomohito Yamada again and owe my deepest gratitude to him for his indefinite support and assistance.

Second, I would like to thank my committee members: Professor Norihiro Izumi, Professor Yasunori Watanabe, Professor Yasuyuki Shimizu and Professor Yasushi Fujiyoshi for all of their invaluable help, guidance and knowledge. Their constant comments and advice enabled me to make my research idea lucid, thereby improving my presentation delivery. They all helped this thesis come into being and I want to take a moment to thank each of them for being part of my committee.

I am grateful to all of my past and present members from River and Watershed Laboratory. Especially, I am grateful to members; Ms. Keiko Sugao, Dr. Tsuyoshi Hoshino, Dr. Shrivastava Sourabh, Dr. Cheng Daiwei, Dr. Keita Shimizu, Mr. Yuta Ohya, Ms. Maki Miyamoto, Mr. Kotaro Miyazaki, Mr. Dan Hashimoto, Mr. Abhinav Dengri, Mr. Kazuma Aoki for all kinds of supports.

I would also like to extend my sincere thanks to all members supporting my observation in Shirahama, Wakayama Prefecture. Especially I would like to thank Associate Professor Yasuyuki Baba and Mr. Teruhiko Kubo for their special supports for planning and maintaining the observations.

In addition, I would like to extend my sincere thanks to Professor Tadashi Yamada, Chuo University for opportunities to present my research and their thoughtful comments reflected in this thesis. Also, I would like to thank to all members of Yamada Laboratory, especially Ms. Shiori Terai and Dr. Naoki Koyama.

Last but not least, I would like to thank my wife Misa, my son Kohki, my parents and all my families.

They have been an amazing pillar of strength for me during this process. I thank them for constantly giving me words of encouragement and cheering me on. They have no idea how much that meant to me, and how special they make me feel. This work would not have been possible without their contributions.

Hiroki Okachi

Contents

List of Figures

LIST OF FIGURES

List of Tables

1

Introduction

1.1 Surface boundary layer under severe wind conditions

Floods and landslides caused by heavy rains occur frequently in Japan. Having discussed the impact of climate change on the frequency and intensity of heavy rainfall, the Fifth Assessment Report (AR5) of the Intergovernmental Panel on Climate Change (IPCC) clearly suggested that there is no doubt that the climate system is warming. Flood risk assessment and its response plan are considered to be an urgent issue.

In the case of Japan, the Ministry of Land, Infrastructure, Transport and Tourism (MLIT) has organized the "Technical Study Group on Flood Control Planning in Climate Change" since 2018, and developed its recommendations in October 2019. In line with this, analysis of d4PDF (detailed later) on precipitation changes was performed, to determine the extent of the future climate relative to the past climate, and the result was 1.15 times higher in the entire area of Hokkaido and 1.1 times higher in other areas with under 2 degrees of warming by the 2040s. The warming represents an increase in global temperature since the pre-industrial era (the 1600s). Since the beginning of 1600s, the temperature has increased by about 1 degree. The d4PDF is a large ensemble climate dataset released as the Database for Policy Decision Making for Future Climate Change,

which consists of several thousand years of simulation with both a historical climate and climates following the progression of global warming (Mizuta et al. (2017) (1)).

Prior to the study by MLIT, mutual discussion by MLIT's Hokkaido Development Bureau and Hokkaido prefecture was made immediately after the heavy rainfall disaster caused by four kinds of typhoons in August 2016 to exchange views on future flood control measures in relation to climate change. In 2009, the Hokkaido branch of MLIT launched the "Study Committee on Flood Prevention Measures in the Severe Rainfall Disaster in Hokkaido in August 2016," implying that "Hokkaido should take the lead in implementing measures for the climate change, as the impact of climate change associated with warming has become evident." Thereby, the committee has been working to assess flood risks in detail and develop adaptation measures. This has been executed by analyzing rainfall data using the climate model in the form of "physically possible rainfall data, so to speak, quasi-observables," which is not based on the extrapolation of existing observational data.

In a study of two river basins in Hokkaido, rainfall at the planning scale was predicted to increase by a factor of 1.3 to 1.4 under climatic conditions where the temperature increased by 4 degrees above pre-industrial levels. The results showed that the frequency and amount of heavy rainfall caused by typhoons increased, and that the intensity of rainfall was higher when the typhoon approached southwestern Hokkaido, where the rainfall tended to be abundant during the 4-degree increase experiment. Nonetheless, there is a need to improve the accuracy of weather forecasts for extreme phenomena such as typhoons. By the Japan Meteorological Agency (JMA), accuracy is evaluated using two elements: the path and intensity of the typhoon. In the case of a typhoon, the forecast error for 24-120-hour forecasts has decreased from the 1980s to present. Moreover, the error for the intensity of typhoons has remained almost unchanged since the 2000s.

1.1.1 Surface drag between the air and sea under tropical cyclone

This study investigates friction between the air and sea, as it is the major contributing factors for a typhoon's strength. The surface boundary layer is the lowest part of the atmospheric boundary layer, which ranges from the surface to approximately 1 km below the surface. Within the surface layer, air turbulence is generated and transfers various fluxes; sensible heat, latent heat and water, which are expressed by bulk equations using bulk coefficients. These parameters are The maximum potential intensity (MPI) theory developed by Emanuel (1995)(23) suggested that the ratio of the enthalpy of the bulk transfer coefficient to drag coefficient must be in the range of 0.75-1.25 when estimating the realistic intensity of tropical cyclones. However, in a previous study, the ratio of observed values was between 0.6 and 0.7 at moderate wind speeds (Black et al., 2007)(15) whose upper limit was 30 ms^{-1} as it is technically difficult to simultaneously measure wind speed beyond 30 ms^{-1} and drag coefficient and the occurrence of high velocity winds are rare near the sea surface. The ratio is well below 0.7 at speeds more than 40 ms^{-1} in the case that the bulk enthalpy transfer and drag coefficients in today's meteorological model are applied. This difference could be because the coefficients have not considered the effect of sea spray (Fairall et al., 2009) (16). Numerical simulation studies have highlighted that parameterizations considering the presence of sea spray decrease drag and enhance heat flux and increase the cyclone intensity, which is associated with an increased maximum surface wind speed by 1.7 times and a decreased minimum sea surface pressure by 0.96 times (Bao, 2011) (36). The simulations were based on the Monin-Obukhov similarity theory, which invokes the parameterizations of air-sea fluxes. In practice, a meteorological model owned by the Australian Bureau of Meteorology considering the sea spray effects has started to be adapted (48).

1.1.2 Relationship between storm surge and drag coefficient

Flux exchanges are sensitive indicators of climate variability and affect storm surges. A storm surge is an increase in the sea level beneath a storm and is caused by the following: i) atmospheric pressure drop by sucking up the sea surface and ii) winds blowing offshore by pushing the seawater toward the shore. In Japan, a storm surge hitting the Ise Bay was caused by the Ise Bay Typhoon in 1959. The typhoon made landfall in western Cape Shionomisaki around 6 p.m. on 26 September with a central pressure of 930 hPa and moved north-northeastward, passing just west of the Ise Bay and passing through the Toyama Bay at midnight on the next day. It was an extremely large typhoon; therefore, the entire Ise Bay was contained within the danger semicircle, with sustained southerly winds more than 30ms^{-1}. A tide gauge, a tool for determining water-level trends, at the Port of Nagoya recorded an increase in water level of 3.90 m above the Tokyo Peil (T.P.) and a meteorological anomaly of 3.55 m. The Ise Bay Typhoon has significantly affected populations: to date, there are 4,697 dead, 38,921 injured, 401 missing, 38,921 houses destroyed, 113,052 houses partially destroyed, and 4,703 flooded houses. The largest typhoon characterized by the lowest central pressure at landfall was the Second Muroto Typhoon. It made landfall on the west side of Cape Muroto in the Kochi Prefecture at 925 hPa. As a side note, a map of the estimated storm surge inundation area for the largest typhoon in history is available in the 2020 Storm Surge Inundation Area Mapping Guide. The map was created based on the return period, and the periods for three major bays - Osaka Bay, Ise Bay, and Tokyo Bay - for instance, are set as 1/500 and 1/1000. When simulating, there are three or more different directions along the path of the typhoon heading to these bays, and the paths can be shifted by each 10 and 20 km in parallel. Such typhoon track simulations are critically important to develop countermeasures against a storm surge. The drag coefficient was thought to increase with wind speed, but since the 2000s, the coefficient has been reviewed due to saturated or reduced cases being found under severe weather conditions including heavy rains and typhoons. Thus, the behavior of the coefficient is regarded as an important element for the investigation of storm surges.

1.2 Fluid dynamics with sea spray

1.2.1 Turbulence in the surface boundary layer

This section provides more information on the Monin-Obukhov similarity theory with reference to turbulence properties in the surface boundary layer and highlights the position of this theory in our study. Specifically, the surface boundary layer is regarded as the constant stress layer of which the vertical fluxes of momentum and heat are considered to be equal to the fluxes at the sea surface. One of the controlling factors of meteorological phenomena is vertical fluxes. The amount of flux exchanged between the atmosphere and the sea surface affects the development of meteorological phenomena. Rainfall often accompanies a storm, generating sea spray at the sea surface. One of the purpose of this study was to observe the concentration of sea spray under rainfall.

Turbulent conditions reflect the surface boundary layer; therefore, meteorological factors such as wind speed and temperature are subject to complex spatial and temporal variations. Russian meteorologists Monin and Obukhov identified such seemingly chaotic situations and proposed the Monin-Obukhov similarity theory in 1954. It states that the mean values of wind speed and temperature in turbulent conditions are expressed with respect to physical quantities of frictional stress and vertical heat flux at the ground surface, $\tau/\rho(\equiv -\overline{u'w'})[\mathrm{m^2 s^{-2}}]$, $H_0/(C_p\rho)(\equiv \overline{\theta'w'} \equiv Q_0)$ $[\mathrm{Kms^{-1}}]$, and buoyancy parameters, g/Θ_0 $[\mathrm{ms^{-2}K^{-1}}]$, assuming a steady and horizontally uniform situation in turbulent conditions. This theory is universally accepted and is still used today. It also serves as the boundary layer theory of many advanced meteorological models.

1.2.2 Review of sea spray studies

This section discusses the historical aspect of sea spray based on the reviewed papers (Andreas et al., 1995(9) and F. Veron, 2015(86)) and our investigation. Researchers Bortkovskii, Borisenkov, Wu, and Ling are pioneers in examining the net effect of sea spray on sensible and latent heat transfer. Flux of sea spray from sea to air is an important aspect of the air-sea interaction, yet much remains

unknown about the surface layer profiles of temperature and humidity. During the 1980s and 1990s, three types of sea spray were identified during the observations of different sea spray concentrations, as shown in **Figure 1.1**. The two of these are film and jet droplets, which emerge when the bubbles in whitecaps burst. The whitecap coverage is the percentage of the sea surface covered by white foam generated when waves break. A film droplet is typically a few μm while a jet droplet is less than 20 μm in size. In contrast to these two droplets, another kind of droplet, a spume droplet, emerges when a wave breaks and is larger in size. The critical wind speed at which spume droplets are generated has been actively discussed. According to Andreas et al. (1995)(9), the wind speed threshold for spume production is 7-11 ms^{-1}.

The bubbles at the sea surface are directly related to production of bubble-mediated sea spray. As the area of each whitecap decreases exponentially with time, the ratio of whitecap area to the total area of sea surface is directly proportional to the instantaneous fraction of the sea surface covered by whitecaps. Sea spray generation functions have not been clarified even in the 2010s and are still being discussed. The same applies to the spume droplet production rate. However, tremendous progress has been made in exploring the sea spray generation function for small and medium-sized droplets, as shown in Figure 6 (Veron, 2015(86)).

In the context of spray droplet microphysics, the rate of spray-mediated fluxes of sensible and latent heat has been determined (Andreas, 1989, 1990) using equations typically used in cloud physics (Pruppacher and Klett, 1978). Fairall et al. (1990)(25) highlighted the properties of sea spray followed by the Monin-Obukov similarity theory and provided an overview of sea spray, the atmospheric boundary layer, and related laboratory and field observations(25). This is based on the Humidity Exchange Over the sea (HEXOS) project(40), which is a research project using a combination of numerical model studies, field measurements, and wind tunnel simulations by HEXIST (ST denotes the Simulation Tunnel at the IMST Laboratoire de Luminy near Marseille, France). The tunnel is 40 m long with a maximum depth of 1.5 m; it is designed to detect particles in a range from 0.5 to 15 μm as well as from 10 to 150 μm, along with profiles of wind speed, temperature, and water vapor density. Fairall et al. (1994)(26)

examined the effects of the microphysics of sea spray on tropical cyclones using an analytical model. The results showed that sea spray rapidly exchanges sensible heat with the surrounding air when it is ejected into the air-sea surface. Assuming that the temperature of sea surface is warmer than that of air, sea spray warms the air and subsequently evaporates followed by the phase change, resulting in the removal of latent heat from the atmosphere. Successively, the energy of evaporation of the sea spray must come from the atmosphere. In addition, Lighthill (1999)(46) noted that the energy at which sea spray evaporated would come from the atmosphere. Therefore, the net sensible heat from sea spray can be calculated as a difference between its sensible heat and latent heat, in the form of the 'feedback effect'.

In the 2000s and 2010s, considering the impact of sea spray on drag, the CB-LAST project was carried out for wind speed observations in hurricanes using dropsonde. According to Powell et al. (2003)(62), the drag coefficient - an indicator of drag between the atmosphere to ocean - decreases at the high wind speed of 33 ms^{-1}. Subsequently, over the last two decades, numerous studies have attempted to explain the causal relationship between reduced drag coefficient and wind speed (see Chapter 2).

Several studies have attempted to describe the leveling off and saturation of the coefficient. We lack knowledge of why the coefficient decreases, and little is known about how much sea spray exists under such situations because it is difficult to observe sea spray under rainfall. Thus, this study attempted to observe sea spray under well-mixed conditions with rainfall (see Chapter 3 to 5).

1.2.3 Drop size distribution of sea spray

The basic physical quantity in this study is the concentration of sea spray. Commonly, the concentration of sea spray is referred to as the drop size distribution, which is measured as the diameter increment per area per second. Previous drop size distributions have been obtained from field observations, wind tunnel experiments, and numerical experiments. The droplets can be classified into three particle diameter scales. Particle diameter ranges from approximately 10^{-5} to 1 mm. 10^{-5} to 10^{-3} are film droplets, 10^{-3} to 10^{-2} are jet droplets, and 10^{-2} to

10^0 are spume droplets. The diameter scale is widely spread and each diameter varies by 2 or 3 orders, especially in spume droplets.

The first observation of sea spray was made by Monahan (1986)(56). In their study, they determined that the amount of spray generated is proportional to the whitecap coverage based on the experimental results. The whitecap coverage is the percentage of the sea surface covered by white foam generated when waves break. Wu observed the amount of spray generated by a kite attached to a ship at sea. Andreas (1998)(5), using the observations of Wu (1993)(88) and Smith et al. (1993)(75), proposed a droplet particle size distribution that includes all particle size ranges up to a wind speed of 32 ms^{-1}. Conversely, Fairall (1994)(26) proposed a particle size distribution for spume droplets.

Based on this background, this study conducted three types of marine observations. Direct observations with a disdrometer were conducted at a marine tower under rainfall (see Chapter 3). Furthermore, radar observation was performed; the methods and results are reported in Chapters 4 and 5. Obtaining information near the sea surface remains elusive because signals from the sea surface are contaminated. Thus, observation near the sea surface has proven difficult.

1.3 Structure of this study

Following the Introduction in Chapter 1, Chapter 2 highlights the investigation of friction between the air and sea under typhoon-like conditions. Several models have been previously proposed to explain the leveling off and saturation of the drag coefficient. With understanding that, active discussions have been conducted for a few decades. In this chapter the author summarized parameterizations and explore effects of sea spray and rain was conducted based on one model.

As discussed in Chapter 3, a series of field observations were conducted at an observational tower lying 1.8 km off the coast of the Wakayama Prefecture, Japan. Two types of optical disdrometers were equipped to detect different particle sizes, which were installed at the 15-m height of the tower. At wind speeds more than 10 ms^{-1}, the amount of sea spray with a diameter less than 1 mm increased in the

absence of rain according to the meteorological radar and tipping bucket located near the tower. Another disdrometer obtained information on two rainfall events, one of which was the typhoon KROSA in 2019. It showed an increased amount of rain droplets with a diameter less than 1 mm along with an increased wind speed. This phenomenon could be associated with an increased amount of sea spray because the rainfall intensity remained constant. It also highlighted the amount of sea spray at various hourly wind speeds (up to 20 ms^{-1}), which may provide better radar estimates of rainfall over the open ocean. A equation for number of sea spray as a function of wind speed is proposed.

Chapter 4 discusses simultaneous radar observations that have the advantage of high time-spatio resolution for a vertical cross section. These allowed us to observe the dynamic structures of multiphase flow with sea spray and rain over the ocean under the typhoons CIMARON, JEBE, and TRAMI in 2018. However, it only included qualitative data due to the technical radar specifications. Therefore, a method was proposed to explore quantitative data that serves as a radar cross section representing the electromagnetic properties of materials. Specifically, the estimation was achieved by the following several proposed methodologies: noise removal, conversion to reflected power, correction based on density of electromagnetic wave, estimation of radar gain, and sea clutter height estimation. The author also proposed a method to estimate profiles of horizontal wind speed and drag coefficient based on radar observation data.

Chapter 5 introduces the conversion methods that were used to convert the radar cross section into the drop size distribution and concentration of sea spray in reference to the results in Chapter 4. This radar observation was based on scattering phenomena in the mixed conditions of sea spray and raindrops: Mie scattering or Rayleigh scattering, and single scattering or multiple scattering. These phenomena differ from each other in the particle size, number, and salinity. Given the drop size distributions of sea spray and rain at different wind speeds and rainfall intensities, sensitivity analysis was conducted to examine the scattering characteristics. This analysis confirmed that scattering by sea spray and rain packed in unit volume was Mie scattering and single scattering, respectively. The proposed two methods enable radar to observe profiles of concentration and wind speed near surface layer simultaneously.

Chapter 6 is the concluding chapter that explains the significance and implications of our findings as well as the contribution of our study to the existing literature.

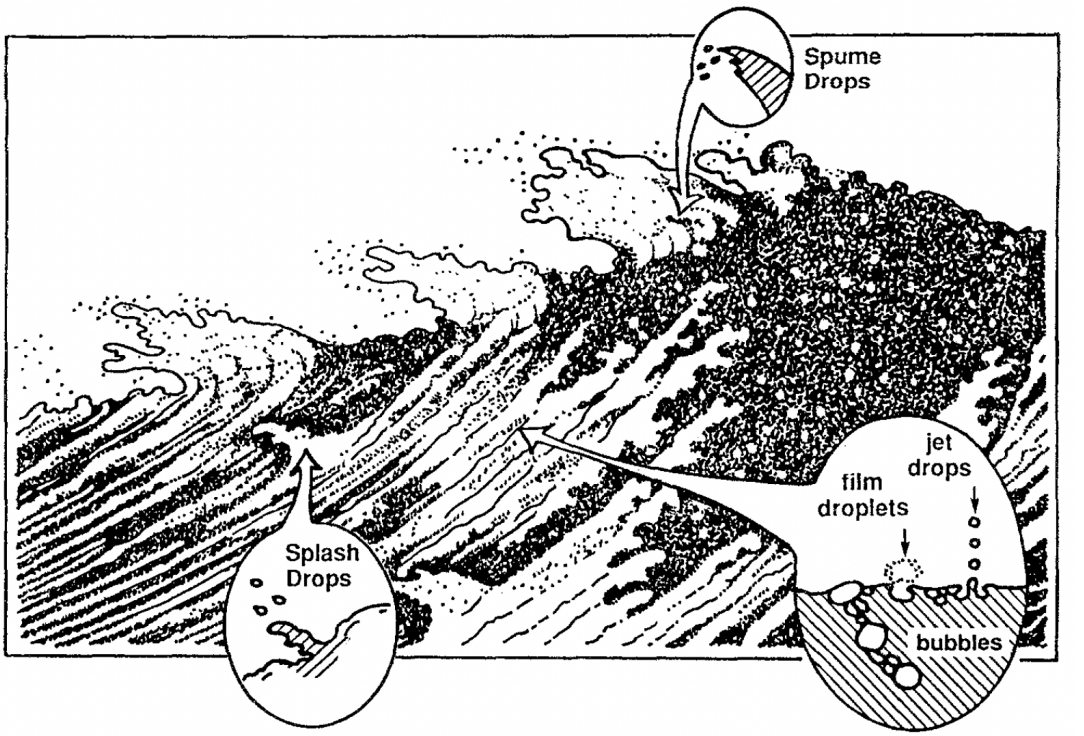

Figure 1.1: Origins of various kinds of sea spray droplets. - Cited from Andreas et al., 1995(9) and based on an illustration by Hokussai (c. 1833).

2

Drag coefficient over the ocean surface

2.1 Introduction

In recent years, typhoons are expected to become more powerful due to the climate change, and there is concern about the increase in damage caused by heavy rains, storm surges, and strong winds. Drag, sensible heat, and latent heat at the air-sea interface are essential variables to influencing the typhoons. In this chapter, several drag coefficients proposed previously is introduced.

Using the drag coefficient at 10 m height C_{DN10} (where D is drag and N is the neutral atmospheric stability), the shear stress of the atmosphere (drag from the sea on air) at 10 m height from the sea surface is defined as

$$\tau \equiv \rho_a u_*^2 = \tau_a = \rho_a C_{DN10} U_{10}^2, \tag{2.1}$$

where ρ_a is the atmospheric density [kg m^{-3}] and U_{10} is the horizontal wind speed at 10 m height [ms^{-1}]. Assuming the horizontal wind speed (hereafter referred to as wind speed) is governed by the logarithmic law,

$$U(z) = \frac{u_*}{\kappa}\Big[\log\big(\frac{z}{z_0}\big) - \psi\big(\frac{z}{L}\big)\Big]. \tag{2.2}$$

Here, $U(z)$ is the horizontal wind speed at height z, κ is von-Karman's constant (κ=0.4), z_0 is the roughness length [m], ψ is universal function, and L is the Monin-Obkhov length. Assuming neutral stability ($\psi = 0$ in **Eq**.(2.2)), the drag coefficient at the height of 10 m is

$$C_{DN10} = \left[\frac{u_*}{U_{10}}\right]^2 = \left[\frac{\kappa}{\ln(10/z_0)}\right]^2, \tag{2.3}$$

Sensible and latent heat fluxes were obtained using the scholar coefficients C_H and C_E.

$$H = \rho_a C_p C_H U(T_s - T_a)$$

$$E = \rho_a C_E L_v U(q_s - q).$$

Here, H is sensible heat flux [Wm^{-2}], C_p is specific heat at constant pressure [$\mathrm{Jkg}^{-}1\mathrm{K}^{-}1$], T_s is the sea surface temperature [K], T_a is the air temperature [K], E is the latent heat flux [Wm^{-2}], L_v is the vaporization heat [Jkg^{-1}], q_s is the saturated specific humidity [kgkg^{-1}], and q is the specific humidity [kgkg^{-1}]. The roughness length is the height at which the wind speed becomes 0 ms^{-1} by vertically extrapolating the wind speed distribution downward in the boundary layer.

The roughness length is commonly expressed as follows.

$$z_0 = \alpha \frac{u_*^2}{g}, \tag{2.4}$$

Here, α is a universal constant, and g is the gravity acceleration [m s^{-2}]. **Eq**.(2.4) is known as Charnock's equation, in which the roughness is non-dimensionalized using the gravitational acceleration g, friction velocity of the wind, and the relationship between the non-dimensional roughness and the constant gz_0/u_*^2 is proposed. This equation does not contain the effect of wave-breaking and sea spray. A further study from Smith (1988)(76) showed that the roughness length for a smooth surface is influenced by the kinematic viscosity of air ν and the friction velocity. Thus, the roughness length formula in **Eq**.(2.4) can be updated to

$$z_0 = \alpha \frac{u_*^2}{g} + 0.11 \frac{\nu}{u_*},$$

The drag coefficient C_{DN10} in **Eq**.(2.3) has been treated as a constant increased monotonically with the increase of wind speed(43); however, the range of wind speed that has been confirmed by both field observations and laboratory experiments is up to approximately 20 ms^{-1}. Powell et al. (2003)(62) flew into the typhoon and then observed the vertical distribution of wind speed using a drop sonde. The wind speed observed at a certain height was used as a reference to classify the observation datasets, and the drag coefficient was estimated based on the vertical distribution of horizontal wind speed obtained by arithmetic averaging, and pointed out that the drag coefficient levels off at wind speeds above 30 ms^{-1}. This behavior is contrary to surface flux parameterizations that are currently used in various modeling applications, including hurricane risk assessment and prediction of hurricane track and intensity, waves, and storm surges. This difference under strong wind conditions leads active discussion and currently many researchers proposed saturated drag coefficient. This trend has caused serious concern in researchers. For example Andreas (2004)(6) explained the effect of sea spray on darg as follows; the sea spray generated by wave breaking in a storm is accelerated by the wind blowing near the sea surface. At this time, the sea spray is considered to be synchronized with the wind speed in the lower layer, which means that it is accelerated in the upper layer. Since the sea spray have mass, they take momentum from the wind. When the sea spray falls to the sea surface, the shear stress of the sea spray is transported to the sea surface.

Fairall et al. (1994)(26) concluded that the effect of droplets on the total shear stress accounted for about 10% at a wind speed of 50 ms^{-1}, and about 1% at a wind speed of 20 ms^{-1}. The distribution of droplets with respect to the drop size used here depends on the wind speed. Andreas (2004)(6) showed that droplets account for about 10 % of the total shear stress at a wind speed of approximately 30 ms^{-1}, and all the shear stress at a wind speed of approximately 60 ms^{-1}. Soloviev and Lukas (2010)(77) investigated a two-layer transition layer consisting of droplets and bubbles between the atmospheric and oceanic surfaces and the Kelvin-Helmholtz instability theory; they found that the lower limit of

the drag coefficient is determined by the collapse of the interface under high wind speeds.

The effect of droplets on the heat exchange between the atmospheric and oceanic surfaces has also been addressed. The sea spray moves within the atmosphere while undergoing phase change. In this process, droplets absorb latent heat from the surrounding atmosphere. Lighthill(46) theorized that the cooling effect on the lowest level of the atmosphere is due to the phase change of droplets and argued the importance of revision to atmospheric boundary layer parameterization. Barenblatt (2005)(13) proposed theoretical approaches to quantify the influence of sea spray on momentum using renormalization theory. Bao et al. (2011)(36) focused on parameterizing the effect of sea spray at hurricane-strength winds on the drag and heat fluxes in weather prediction models using the Monin-Obukhov similarity theory, which is a common framework for the parameterizations of air-sea fluxes. As the wind speed increases, the mean droplet size and the mass flux of sea-spray increase, rendering an increase of stability in the marine surface boundary layer and a leveling-off of the surface drag. Soloviev et al. (2014)(78) introduced a new parameterization for the air-sea interaction based on Soloviev and Lukas (2010)(77) and suggested that the new parameterization predicts a local peak of the ratio of the enthalpy coefficient against the drag coefficient for the wind speed range around 60 ms^{-1}. Emanuel(23) expressed the vertical mixing in the atmospheric boundary layer based on the ratio of the drag coefficient to the heat exchange coefficient. This indicates that the drag and heat exchange between the air-sea surfaces affect convection of cumulus clouds and suggests the importance of the effect of droplet-derived shear stress on the drag coefficient.

Considering Powell et al. (2003)(62), the presence of sea spray has been highlighted as one of the possible factors for drag coefficient decrease. The other possible explanation is the development of the sea foam layer at the air-sea interface, which is created with streaks of bubbles on the sea surface. These streaks are formed by surface wind reaching hurricane strength and combined with patches of 20–50 m widely spread foam. As the wind speed reaches 50 ms^{-1}, the sea surface is covered by a layer of foam and becomes a smooth interface. The purpose of

this chapter is to evaluate the effects of both sea spray and raindrops on the drag coefficient; thus, recent studies are comprehensively introduced.

2.2 Drag coefficient with various explanations

In this chapter, drag coefficients suggested by previous studies were introduced . As mentioned in the previous chapter, these coefficients have been treated as constant, or linear. The linear relationship is based on the Monin-Obkhov similarity theory assuming neutral stability. Then, **Eq**(2.3) is obtained. This coefficient is validated by observations and a wind tunnel experiment up to 20 ms^{-1}. However, this coefficient levels off at hurricane-like wind speeds around 30 to 40 ms^{-1} (62). This means that the friction between the air and sea becomes weaker. Consequently, typhoon keeps its energy. This huge difference of understanding of the drag leads active discussions and currently, many researchers proposed saturated drag coefficient. The characteristics are summarized in the **Figure 2.1**.

The real situation under typhoon is shown in **Figure 2.2**. As time goes on (a) to (b) and (c), there are more wave breaking occurred and becomes foggy. From (d) to (e) and (f), the situation becomes messy and complexed due to sea spray and rainfall, and in (d) still wave breaking is captured. This is the real situation under typhoon.

The **Figure 2.3** shows the concept the air-sea interactions. The interactions are drag, sensible heat transfer and latent heat transfer. These can be affected by phenomena like rainfall, sea spray, waves, wind and so on. Several studies proposed various parameter to represent the interactions considering effects of phenomena. Following subsections introduce these parameterizations. The main concepts of these are explained in **Figure 2.4**. The relationship between wind, wave and sea spray generations is shown in Case 1. The situations of sea surface varies by wind like high wave, wave breaking and generation of sea spray. Enough wave breaking leads to smooth sea surface. These three situations have impacts on the drag coefficient. Case 2 shows the effect of rainfall on the surface drag. Case 3 shows the situations with third layer of sea spray on the sea surface. Case 4

shows the relationship between wind direction and direction of wave propagation. These are considered in following parameterizations.

2.2.1 Shear stress from sea spray

Andreas and Emanuel (2001)(8) suggested that wave-induced stress could be subjected to a damping impact by the re-entrant spray into the ocean when the wind speed is high. The momentum from the re-entrant spray could vertically redistribute, causing a decrease in the effective stress, as postulated in Andreas (2004)(6). It obtained the following equation based on the assumption of a constant stress layer, where the shear stress τ is composed of two terms: the shear stress due to the atmosphere $\tau_a(z)$ and the shear stress due to droplets $\tau_{sp}(z)$. Furthermore, the total amount τ is conserved, obtaining the following equation.

$$\tau \equiv \tau_a(z) + \tau_{sp}(z) = \rho_a C_{DN10,sp} u_{10}^2 + \tau_{sp}(z),$$

The constant stress layer means that the total stress in the surface layer is not influenced by height. At sea level $z = 0$,

$$\rho_a u_*^2 = \rho_a C_{DN10,sp} u_{10}^2 + \tau_{sp}(0), \tag{2.5}$$

Here, $C_{DN10,sp}$ is the drag coefficient with the effect of sea spray. When solving **Eq**.(2.5) for $C_{DN10,sp}$, then

$$C_{DN10,sp} = \frac{u_*}{U_{10}^2} - \frac{\tau_{sp}(0)}{\rho_a U_{10}^2}, \tag{2.6}$$

The shear stress of sea spray on the sea surface can be obtained,

$$\tau_{sp} = \frac{4\pi}{3} \rho_w u \int_{r_{lo}}^{r_{hi}} r_0^3 \frac{dF}{dr_0} dr_0, \tag{2.7}$$

where ρ_w is the density of sea spray [kgm^{-3}], and here we use the same value for rain. u is the wind speed at an averaged significant wave height because breaking waves generate sea spray. The range of integration, r_{lo} and r_{hi}, are 1 and 500 μm, respectively. r_0 is the radius of sea spray [μm]. Since F is the amount of sea spray per unit area and unit time, a unit of dF/dr_0 is the number of particles per unit

area, unit radius, and unit time [$m^{-2}\mu m^{-1}s^{-1}$]. $4\pi/3\rho_w r_0^3 dF/dr_0$ is the mass flux of sea spray with radius r_0. Andreas (1998)(5) assumed that u is proportional to u_*. If wave breaking is caused by the energy received from the wind, the energy lost when breaking is equivalent to it. The work of the wind per unit area is expressed by the shear stress τ and the wind speed u, which are expressed by the equation **Eq**.(2.1). In addition, dF/dr_0 is proportional to u_*^3. Furthermore, Andreas and Emanuel (2001)(8) assumed that the shear stress of the atmosphere is equal to that of sea spray when the wind speed reaches typhoon strength, and obtained the following equation.

$$\tau_{sp} = 6.2 \times 10^{-5} \rho_w u_*^4, \tag{2.8}$$

Vertical profile of wind speed assuming the atmospheric stability is neutral,

$$U(z) = \frac{u_*}{\kappa} \ln(z/z_0), \tag{2.9}$$

The following equation is obtained by substituting **Eq**.(2.6) for **Eq**.(2.8) and **Eq**.(2.9) and deriving the drag coefficient of $C_{DN10,sp}$.

$$C_{DN10,sp} = \left[1 - 6.2 \times 10^{-5} \left(\frac{\rho_w}{\rho_a}\right) u_*^2\right] \left[\frac{\kappa}{\ln(\frac{10}{z_0})}\right]^2. \tag{2.10}$$

The above equation shows that the wind speed increases up to 10∼15 ms^{-1} with increasing Z_0 in the Charnock(21) relation. Furthermore, $C_{DN10,sp}$ has a peak at 30∼40 ms^{-1}. This is because the shear stress of sea spray increases with wind speed, which indirectly shows that the roughness height z_0 decreases due to the breakup caused by the impact of the spray on the sea surface. The drag coefficient expressed by equation **Eq**.(2.10) does not consider wave breaking caused by sea spray. This coefficient highly depends on sea spray stress shown in **Eq**.(2.8) derived from **Eq**.(2.7). That is why the sea spray generation function plays an important role in characterizing sea spray regarding its dragging effect on the near-sea surface wind as well as its capacity in transferring shear stress to the sea surface. However, the functions reported by previous studies vary significantly(86). Wan et al. (2019)(87) proposed a new generation function based on the windsea-Reynolds number as well as a new drag coefficient based on the function.

2.2.2 Roughness length and sea spray

It has been commonly recognized that the wave state has an important impact on the wind shear stress(81). By analyzing and synthesizing numerous field and laboratory observations, SCOR workgroup 101(39) presented a relationship between the Charnock parameter α in **Eq**.(2.4) and wave age β.

$$z_0 = \begin{cases} 0.03\beta \exp\left(-0.14\beta\right), & \sim 0.35 < \beta < 35 \\ 0.008, & 35 < \beta. \end{cases} \tag{2.11}$$

Wave age β is defined as c_p/U_{10}, and the corresponding drag coefficient can be calculated through iteration. This relationship is determined mainly from observations under low-to-moderate wind conditions without consideration of other factors such as sea spray. Liu et al. (2012)(47) proposed a new parameterization of sea surface aerodynamic roughness as follows:

$$z_0^l = \begin{cases} (0.085\beta_*^{3/2})^{1-1/\omega}\left(0.03\beta_* \exp\left(-0.14\beta_*\right)\right)^{1/\omega}, & (\sim 0.35 < \beta_* < 35) \\ 17.60^{1-1/\omega}(0.008)^{1/\omega}, & (\beta_* \geq 35) \end{cases} \tag{2.12}$$

Powell et al.(62, 63) estimated the drag coefficient from the vertical distribution of the observed horizontal wind speed, which begins to decrease when the wind speed reaches 33 ms^{-1} ($u_* = 1.55$). Makin(49) estimated the wind speed at which the droplets begin to affect the wind speed distribution to be 33 ms^{-1}, and the fall speed of the droplets to be 0.64 ms^{-1} from equation **Eq**.(2.12). ω in **Eq**.(2.12) shows an effect of sea spray on the following logarithmic profile,

$$U(z) = \frac{u_*}{\kappa\omega}\ln(z/z_0^l).$$

This equation is based on Barenblatt (1979), which is a solution to turbulent kinetic energy balance for the airflow in the part of the sea surface layer that is saturated with suspended sea spray: the third fluid in Lighthill (1999)(46). Here, z_0^l is the local roughness, ω is positive and satisfies the condition that $\omega = a/\kappa u_* < 1$, and a is the terminal fall velocity of the droplets. The following explanation is from Barenblatt (1996)(11).

The friction velocity u_* is proportional to the mean square velocity fluctuation. Thus, if the fluctuation is large, so that during the time in which a fluid mass is lifted up by the turbulent fluctuation the heavy particles inside it have no time to fall (the velocity a of free fall being relatively small), the particles come into the main core of the flow and become suspended in it. In the opposite case, the particles are transported by the flow in the bottom layer, do not reach the main core of the flow, and do not influence the flow dynamics in the main part of the stream.

This means that suspended particles accelerate the flow and decrease the turbulent drag. Under these conditions, the von Karman constant apparently decreases, which has been observed by experimentalists (Vanoni, 1946; Einstein and Ning Chen, 1955). This phenomenon is not only for the surface boundary layer in the atmosphere but also for river flow with suspended sand particles. This logarithmic law and a neutral one (**Eq**.(2.9)) are connected to each other at the height of the sea spray suspension layer, h_l. Makin (2005)(49) derived the residence law of the sea surface at hurricane winds. It can be written as the logarithmic law and the SCOR relation (**Eq**.(2.11)) were combined to obtain the following relationship.

$$\frac{gz_0}{u_*^2} = \begin{cases} C_l^{1-\frac{1}{\omega}} \left[0.03\beta_* \exp\left(-0.14\beta_*\right)\right]^{1/\omega}, & (\sim 0.35 < \beta_* < 35) \\ C_l^{1-\frac{1}{\omega}} (0.008)^{1/\omega}, & (\beta_* \geq 35) \end{cases} \tag{2.13}$$

Here, β_* is

$$\beta_* = \frac{c_p}{u_*},$$

Here, c_p is the phase velocity of the wave [ms^{-1}]. c_l is the non-dimensional significant wave height, thus

$$c_l = \frac{1}{10}\frac{gH_s}{u_*^2}, \tag{2.14}$$

Here, H_s is the significant wave height [m] using the empirical equation of Toba (1972)(82).

$$H_* = BT_*^{3/2}, B = 0.0062, \tag{2.15}$$

Here, H_* is the non-dimensional wave height gH_s/u_*^2 and T_* is the non-dimensional significant frequency gT_s/u_*. Combining **Eq**.(2.14), (2.15),

$$c_l = 0.0062\left(\frac{gT_s}{u_*}\right)^{3/2},$$

The peak frequency is derived from the significant frequency.

$$T_s = 0.91T_p,$$

The phase velocity of a wave c_p is a function of gravity acceleration and peak frequency T_p,

$$c_p = \frac{gT_p}{2\pi},$$

The wave age, which is an indicator of wave development is,

$$\beta_* = \frac{c_p}{u_*} = \frac{gT_p}{2\pi u_*},$$

Then, inserting **Eq**.(2.17), (2.18), (2.19) into *Eq*.(2.13),

$$z_0 = \begin{cases} (0.085\beta_*^{3/2})^{1-1/\omega}\left(0.03\beta_*\exp\left(-0.14\beta_*\right)\right)^{1/\omega}, & (\sim 0.35 < \beta_* < 35) \\ 17.60^{1-1/\omega}(0.008)^{1/\omega}, & (\beta_* \geq 35) \end{cases} \tag{2.20}$$

The series of equations assumes that the terminal fall velocity of sea spray is 0.64 ms^{-1}, because 33 ms^{-1} ($u_* = 1.55$) is a critical value of the wind speed(62). The particle diameter for this falling velocity is 80 μm, which is consistent with the representative particle diameter of 80$\sim$200 μm in the particle diameter distribution of droplets, proposed in previous studies. Given the wave age and wind speed at a height of 10 m, the drag coefficient is calculated using **Eq**.(2.6) and **Eq**.(2.20) through iteration. This is one example in which the effect of sea spray is described by roughness length.

2.2.3 Lighthill's sandwich model

This concept proposed by Sir James Lighthill (12, 22), who was a chair of the Department of Applied Mathematics and Theoretical Physics (DAMPT), University of Cambridge as a Lucasian Professor of Mathematics in his last published research. He suggested that parameterizations of the surface boundary layer, such as drag on the air and exchanges of latent and sensible heat, should be revisited. In his research, "spray cooling" due to phase change of sea spray is estimated by algebraic equations. The detailed derivation is in Appendix. His concept was named as "Sandwich model" by Barenblatt et al. (2005)(13). G. I. Barenblatt(14) suggested that the von-Karman constant varied with the Reynolds number. This breakthrough has versatility because this concept can be applied for turbulent flow laden by particles such as sediment flow in a river or dust devils on Mars.

2.2.4 Sea spray generation function

In this section, previous drop size distributions are introduced suggested by previous researchers. The previous drop size distributions have been obtained from field observations, wind tunnel experiments, and numerical experiments in previous researches. The droplets can be classified into three particle size scales. The particle size range is approximately 10^{-5} to 1 mm. 10^{-5} to 10^{-3} are film droplets, 10^{-3} to 10^{-2} are jet droplets, and 10^{-2} to 10^{0} are spume droplets.

The first observation of spray was made by Monahan et al. (1968)(56) In the study, they determined that the amount of sea spray generation is proportional to the whitecap coverage. The white wave coverage is the percentage of the sea surface covered by white foam generated when waves break. Wu observed the amount of sea spray generated by a kite attached to a ship at sea. Andreas (1992)(3), using the observations of Wu (1987), proposed a droplet particle size distribution that includes all particle size ranges up to a wind speed of 32 ms^{-1}. In contrast, Fairall et al. (1994)(26) proposed a drop size distribution for spume droplets. Andreas and Decosmo (2002)(7) examined many drop size distributions and found that they strongly depend on the wind speed. Wan et al. (2019)(87) used the following sea spray generation based on the wind-sea Reynolds number

R_B proposed by Toba (1961):

$$R_B = \frac{u_*^2}{\omega_p \nu}, \tag{2.21}$$

where ω_p is the spectral peak angular frequency. Through the function, the influence of wave states, which is described by the wind-sea Reynolds number at the air-sea interface and the sea spray generation function, was investigated, which suggested that the effect of ocean waves should be considered when studying the influence of droplets on the sea surface drag coefficient. A new generation function used in this paper is as follows:

$$\frac{dF}{dr_0} = \begin{cases} 1.43 \times 10^{-3} R_B^{1.5} r_0^{-0.5}, & 10 < r_0 \leq 30 \\ 7.84 \times 10^{-3} R_B^{1.5} r_0^{-1}, & 30 \leq r_0 \leq 75 \\ 4.41 \times 10^{1} R_B^{1.5} r_0^{-3}, & 75 \leq r_0 \leq 200 \\ 1.41 \times 10^{13} R_B^{1.5} r_0^{-8}. & 200 \leq r_0 \leq 500 \end{cases}$$

In **Figure 2.5**, previous functions are shown. These functions are under windy situations at a wind speed of 15 ms^{-1}. Those functions have different and narrow diameter ranges. The drop size distribution proposed by Wan et al. (87) is shown in **Figure 2.6**. Using this drop size distribution, change of drag coefficient is investigated. The figure shows the relationship between the drag coefficient and friction velocity. From this figure, an increase in drop size distribution causes a decrease in the drag coefficient. The drop size distributions described above are only a part of the equation; various other proposals have been made and are summarized in **Figure 2.5**. In this figure, the wind speed at a height of 10 m is 15 ms^{-1}. The drop size distribution shown is the result of field observation and a wind-tunnel experiments. Aerosol particles are defined as particles with a diameter is less than10 μm, and seas spray are defined as particles with a diameter is 10 $\sim$100 μm or more. The number of drops differs from the aerosol particles by two to four orders of magnitude.

2.3 Dependence of parameterization of drag coefficient on the drop size distribution of sea spray

In this section, the dependence of the drag coefficient on sea spray functions is investigated based on Andreas (2004)(6). It has been indicated that sea spray with radius up to 500 μm could quickly reach at the wind speed within only 1 second when the wind speed is greater than 10 ms^{-1}. This indicates that all sea spray ejected from the sea surface can extract momentum from the air and slow the near-surface wind before returning to the sea. After sea spray falls, the shear stress of sea spray is transferred to the sea surface. This assumes that a droplet's speed is less than the wind speed at the generation height. Troitskaya et al. (2016)(83) suggested a stochastic model of the life cycle of the droplets injected from the sea surface to the air. This model contains both situations in which sea spray delivers and gains the momentum, leading to sea spray decelerating the air flow and increasing the drag coefficient.

Moreover, the effect is significantly larger at higher wind speeds. The dependence of the drag coefficient on the sea spray generation function was investigated in Wan et al. (2019)(87). Wan et al. (2019)(87) used the following sea spray generation based on the wind-sea Reynolds number R_B proposed by Toba (1961):

$$R_B = \frac{u_*^2}{\omega_p \nu} \tag{2.22}$$

where ω_p is the spectral peak angular frequency. A new generation function used in this paper includes the following equations:

$$\frac{dF}{dr_0} = \begin{cases} 1.43 \times 10^{-3} R_B^{1.5} r_0^{-0.5} & 10 < r_0 \leq 30 \\ 7.84 \times 10^{-3} R_B^{1.5} r_0^{-1} & 30 \leq r_0 \leq 75 \\ 4.41 \times 10^{1} R_B^{1.5} r_0^{-3} & 75 \leq r_0 \leq 200 \\ 1.41 \times 10^{13} R_B^{1.5} r_0^{-8} & 200 \leq r_0 \leq 500 \end{cases}$$

The drop size distribution is shown in **Figure 2.6**. Through **Eq**.(2.22), the influence of wave states, which is described by the wind-sea Reynolds number at the air-sea interface and the sea spray generation function, was investigated and suggested that the effect of ocean waves should be considered when studying the influence of droplets on the sea surface drag coefficient. **Figure 2.7** shows the relationship between wind speed and the drag coefficient. The black line shows the ordinal drag coefficient, which increases monotonically with an increase in wind speeds. The dashed line shows the drag coefficient proposed by Andreas (2004). Red lines indicate the drag coefficient with various sea spray drop size distributions. The other dots are the results from airplane observations (Powell et al., (2003) and Powell, (2007)). The range of drag coefficient widely spreads at the higher wind speeds. This parameterization can represent the observed drag coefficient. However, it is difficult to determine the drop size distribution is correct or not.

2.4 Shear stress of rainfall and drag coefficient

Since raindrops exist under stormy conditions, raindrops can also be cited as a factor. The relationship between the shear stress near the sea surface due to raindrops and the wind speed distribution was discussed by Caldwell and Elliott(17, 18). Raindrops falling on the field of shear stress change their horizontal velocity as they fall.

Following the paper, it is hypothesized that the wind and the raindrop are horizontally moving together at certain height. Below this level, the wind is presumed to be given by a logarithmic wind profile. Assuming the horizontal direction of wind and rain is always together, horizontal speed of rain at the sea surface is obtained. As a result of that, shear stress from the ocean to the atmosphere possibly varies. Hypothesizing that velocity of ocean surface current is zero and shear stress of rain drops generates velocity of that, consequently relative velocity between wind and ocean current becomes smaller and drag becomes smaller too. Noted that this hypothesis is limited conditions. Drag coefficients obtained by field observations are estimated from profiles of horizontal wind speeds. The wind

speed profile is an end results of complex phenomena like wave development, wave breaking, rain drop, sea spray, relationship between wind direction and direction of wave propagation. With understanding that, ratio of shear stress of rain drops on the ocean surface against the total shear stress of the air to sea is investigated.

The shear stress due to rain τ_R on the ocean surface is described as

$$\tau_R = r_t \rho_w R u_{10} \tag{2.23}$$

where r_t is the horizontal velocity of a raindrop falling on the sea surface divided by the 10 m height wind speed, ρ_w is the density of the raindrop [kg m^{-3}], and R is the rainfall intensity [mmh^{-1}]. When the rainfall intensity is several tens of mmh^{-1} and the wind speed is 10∼20 ms^{-1}, the shear stress of raindrops τ_R is 20∼30 % of the shear stress of the atmosphere τ_a.

The horizontal velocity of a raindrop falling in a shear stress field does not change immediately. The shear stress of a raindrop τ_R is expressed by the equation **Eq.** (2.23). Caldwell and Elliot(17, 18) set r_t to be 0.85 regardless of rainfall intensity. In this study, r_t is set to vary with raindrop diameter and wind speed. The model considers the terminal fall velocity of rain against wind speed. Force against rain is shown in **Figure 2.8**. F_G, F_x, F_z are friction force and the horizontal/vertical elements of it, respectively. w_a, w are the diagonal relative speed and vertical element. v is the horizontal speed of rain, u is the horizontal wind speed, and α is the angle between w_a and w. Friction force against particle F_G is described as follows:

$$F_G = \frac{1}{2} C_{DR} \rho_a w_a^2 \frac{\pi}{4} d^2$$

C_{DR} is the drag coefficient depending on radius, and d is the rain drop diameter. w_a is described as

$$w_a^2 = w^2 + \big(v - u\big)^2$$

Horizontal and vertical equations of motion for rain are described as follows:

$$-\frac{1}{2} C_{DR} \rho_a w_a^2 \frac{\pi}{4} d^2 \sin\alpha = \frac{\pi}{6} d^3 \rho_w a_h \tag{2.24}$$

$$\begin{aligned} \frac{1}{2} C_{DR} \rho_a w_a^2 \frac{\pi}{4} d^2 \cos\alpha = &-\frac{\pi}{6} d^3 \rho_w a_v \\ &+ \frac{\pi}{6} d^3 \big(\rho_w - \rho_a\big) g, \end{aligned} \tag{2.25}$$

where a_h and a_v are the acceleration of raindrops in the horizontal and vertical directions, respectively. The second term on the right-hand side of **Eq**.(2.25) represents the difference between the gravitational and buoyancy forces. When the raindrop reaches terminal velocity, a_v becomes zero as an approximation. Assuming that $w_a^2\alpha$ is constant, the left-hand side of **Eq**.(2.25) is constant. **Eq**.(2.25) becomes

$$\frac{1}{2}C_{DR}\rho_a w_a^2 \frac{\pi}{4}d^2 \cos\alpha \approx \frac{\pi}{6}d^3\big(\rho_w - \rho_a\big)g. \tag{2.26}$$

If the difference in the horizontal speed of rain and wind speed is relatively small, then $\cos\alpha \approx 1$, $w_a \approx w$. **Eq**.(2.26) becomes,

$$\frac{1}{2}C_{DR}\rho_a w^2 \frac{\pi}{4}d^2 \approx \frac{\pi}{6}d^3\big(\rho_w - \rho_a\big)g \tag{2.27}$$

Here, the terminal fall velocity of rain w is converted into $-dz/dt$, and $\tan\alpha$ is $\big(v-u\big)/w$. From **Eq**.(2.24) and (2.27), we obtain

$$-\tan\alpha = \frac{\rho_w a_h}{\big(\rho_w - \rho_a\big)g} = -\frac{v-u}{w}. \tag{2.28}$$

Solving **Eq**.(2.27) for w^2,

$$w^2 = \frac{\frac{\pi}{6}d^3\big(\rho_w - \rho_a\big)g}{\frac{1}{2}C_{DR}\rho_a\frac{\pi}{4}d^2} = \frac{4d\big(\rho_w - \rho_a\big)g}{3C_{DR}\rho_a} \tag{2.29}$$

Multiplying **Eq**.(2.28) and **Eq**.(2.29)

$$-\big(v-u\big)w\frac{3C_{DR}\rho_a}{4d\rho_w} = a_h. \tag{2.30}$$

Using $a_h = dv/dt$, $w = -dz/dt$, **Eq**.(2.30) is

$$\frac{3C_{DR}\rho_a}{4d\rho_w}\big(v-u\big) = \frac{dv}{dz} \tag{2.31}$$

Solving **Eq**.(2.31) numerically, the horizontal wind speed of rain is obtained. **Figure 2.9** shows the results of this.

Solving **Eq**.(2.27) for C_{DR}, the following **Eq**.(2.32) is obtained.

$$C_{DR} = \frac{4d\big(\rho_w - \rho_a\big)g}{3\rho_a w^2}. \tag{2.32}$$

The terminal fall velocity was estimated from the equation of Gunn and Kinzer(33). In this process, the ratio r_t of the horizontal speed of rain and horizontal wind speed at a 10-m height is obtained. Using the horizontal velocity of raindrops at the roughness length obtained from the same analysis, it is possible to estimate the shear stress brought to the sea surface by raindrops with a certain drop size. In addition, the number of raindrops with respect to the drop size at a given rainfall intensity can be expressed by using the Marshall and Palmer distribution (52) to estimate the shear stress of raindrops on the sea surface at a given rainfall intensity. In this chapter, a ratio between the shear stress against the shear stress of the atmosphere is investigated, which can be obtained from the ordinal drag coefficient using the wind speed at 10 m height and the drag coefficient based on **Eq.** (2.1) and (2.3).

2.5 Results

Figure 2.9 shows vertical profiles of horizontal wind (black solid line) and raindrops (red soil line) speed when rainfall intensity is between 30 to 100 mmh^{-1} at every 40 mmh^{-1}. Here, horizontal wind speed at 10-m height is 40 ms^{-1}. Here air density is 1.29 kgm^{-3} and the roughness height is 0.005 m to correspond to the wind condition. Raindrops have initially have equivalent horizontal speed as surrounding winds but gradually have larger speed compared to winds with decrease of height. Raindrops for every rainfall intensity still have horizontal component of speed at the roughness height such as approximately 34 ms^{-1} for 100 mmh^{-1}.

Figure 2.10 shows the ratio of rain shear stress on the ocean surface. To calculate this ratio, the ordinal drag coefficient defined as **Eq.**(2.3) is used. The color shows the ratio and white area is the proportion over 50 %. Up to a certain wind speed below 30 ms^{-1}, shear stress is dominated by the effect of raindrops. However, ratio gradually decreases with increase of wind speed. On the other hands, ratio gradually increase with increase of rain intensity.

2.6 Summary and conclusions

The drag coefficient reaches a peak between wind speeds of 30 ∼40 ms^{-1} (62) or becomes constant (63) contrary to expectation. The trends lead active discussions by many researchers. There are several parameterizations considering phenomena shown in this chapter: wave breaking, sea spray making third smooth layer, relationship between wind direction and direction of wave propagation and shear stress of rainfall on the sea surface.

The purpose of this chapter was to investigate dependence of parameterization based on Andreas (2004)(6) on drop size distribution referred to Wan et al. (2019)(87). Variety of drop size distribution leads various drag coefficient which can represent the observed drag coefficient.

The effect of raindrops on the drag coefficient at a 10-m height is proposed by Caldwell and Elliot(17, 18). The shear stress of each raindrop size on the ocean surface is estimated based on its model, but in this thesis, number of drops in each diameter is considered using drop size distribution of Marshall and Palmer (1948)(52). The effect of raindrops becomes larger with increase of rainfall intensity; however, the effect decreases with increase of wind speed.

Because of the complexity of phenomenon, the model is suitable for making it simple and understanding that proportion of rainfall shear stress to the total shear stress varies with wind speed and rainfall intensity. However, the multi-interactions between the air and raindrop is not considered. This means that the interactions affect the raindrop velocity but not the wind field. Shapiro (2005)(73) suggested the two-way coupling model that the coupled equations of motion for the air and raindrops together with a mixing length representation for the turbulent stress were solved iteratively. As a result of that, profile of horizontal wind speed was found to deviate only slightly from the logarithmic wind profile, even when it is heavy rainfall.

More detailed observations of the vertical profile of wind speed are needed to determine whether the shear stress caused by rainfall would change the drag coefficient, and hence the vertical profile of wind speed, so that the effect of rainfall on the drag coefficient would become apparent.

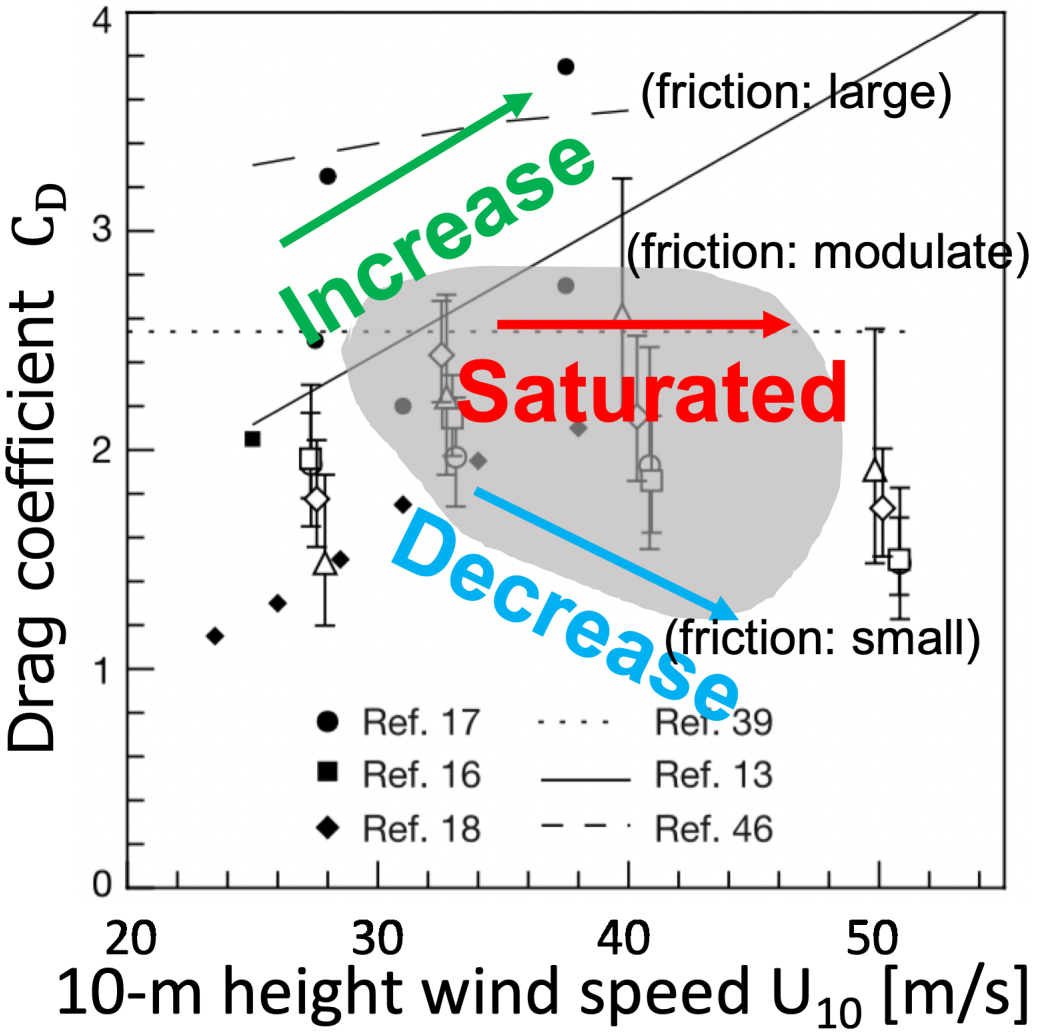

Figure 2.1: Relationship between drag coefficient and horizontal wind speed at 10-m height - This figure is cited from Powell et al., (2003)(62) and modified by the author.

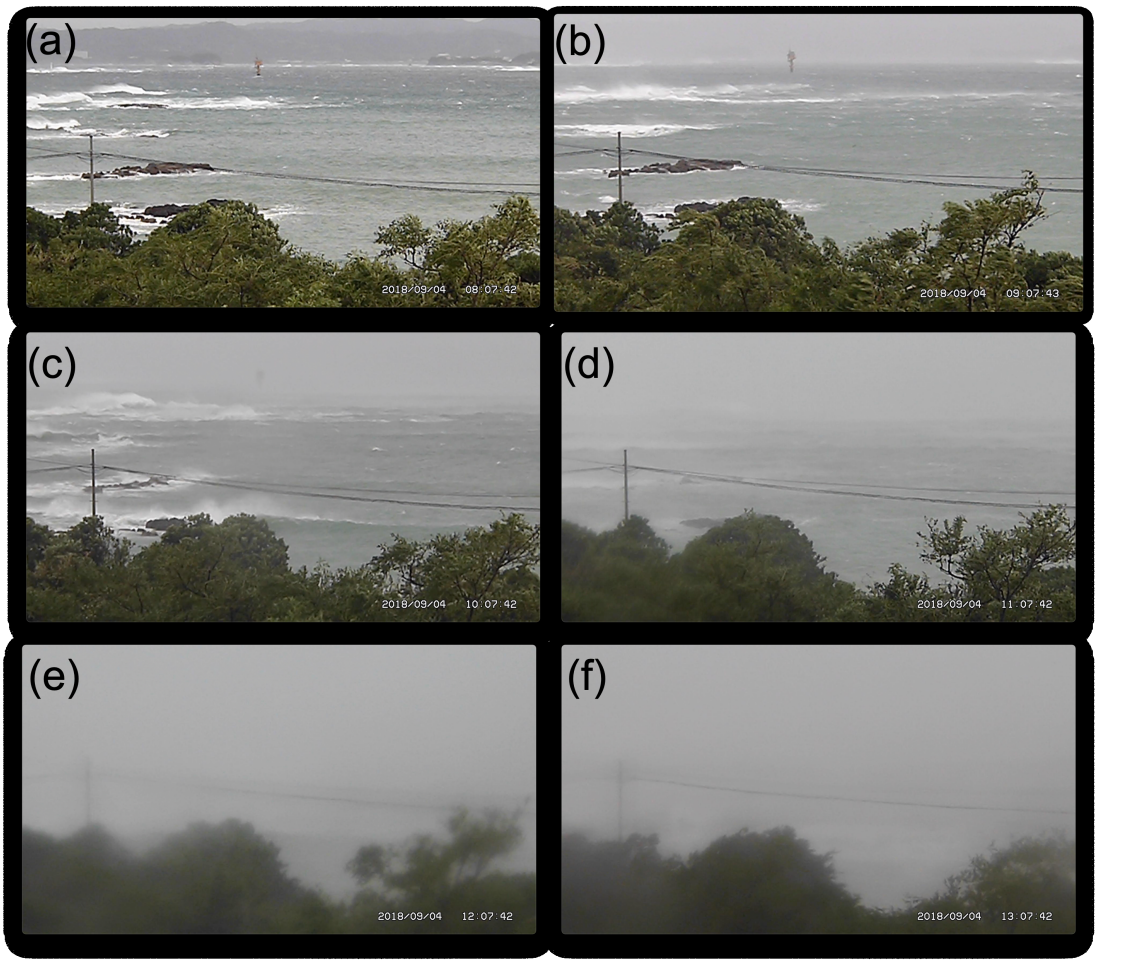

Figure 2.2: Photos under typhoon 21st (JEBI) of 2018 at Shirahama, Wakayama Prefecture. - Photos are taken at Nanki-Shirahama. (a)-(f) are taken at each 1 hour from 08:07 to 13:07 on September 4th, 2018.

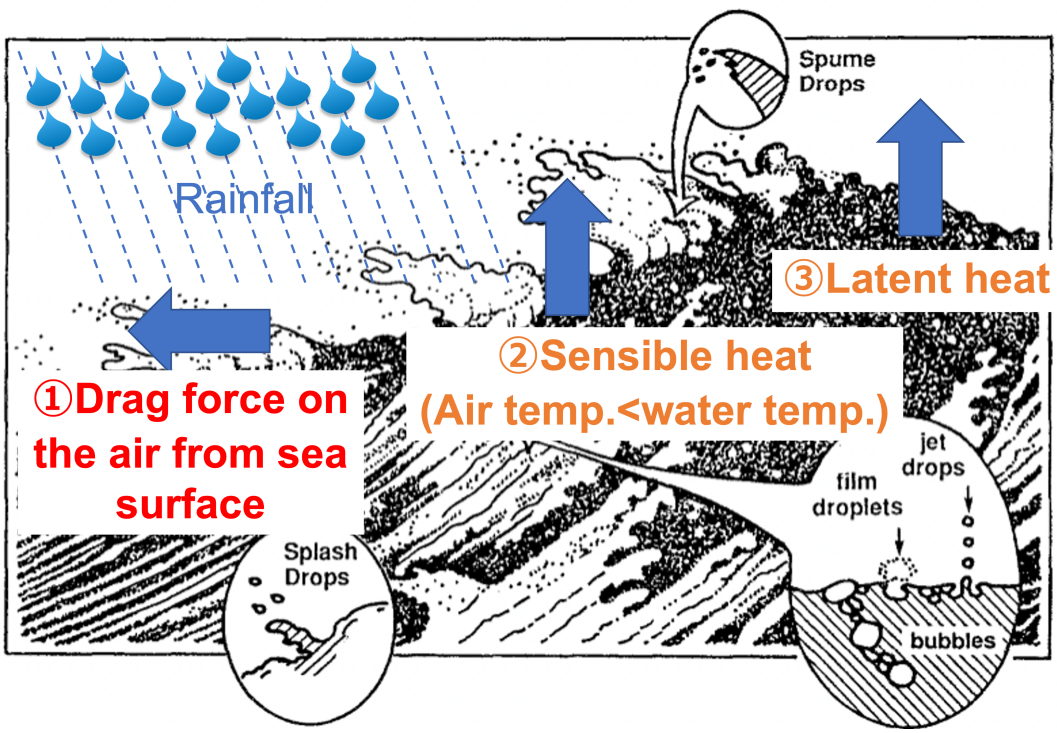

Figure 2.3: Air-sea interactions with rainfall and sea spray under severe wind conditions. - Three types of sea spray are generated. This figure is cited from Andreas et al. (1995)(9) and modified by the author.

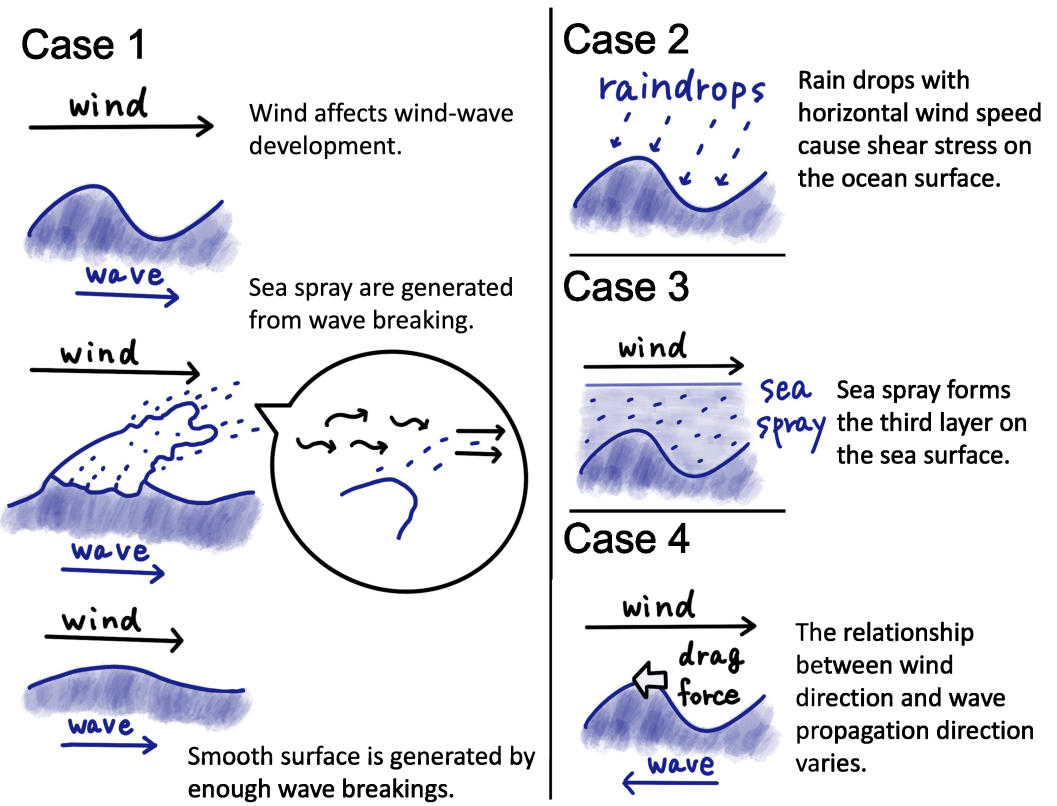

Figure 2.4: Air-sea interactions with several phenomena. - There are mainly four situations.

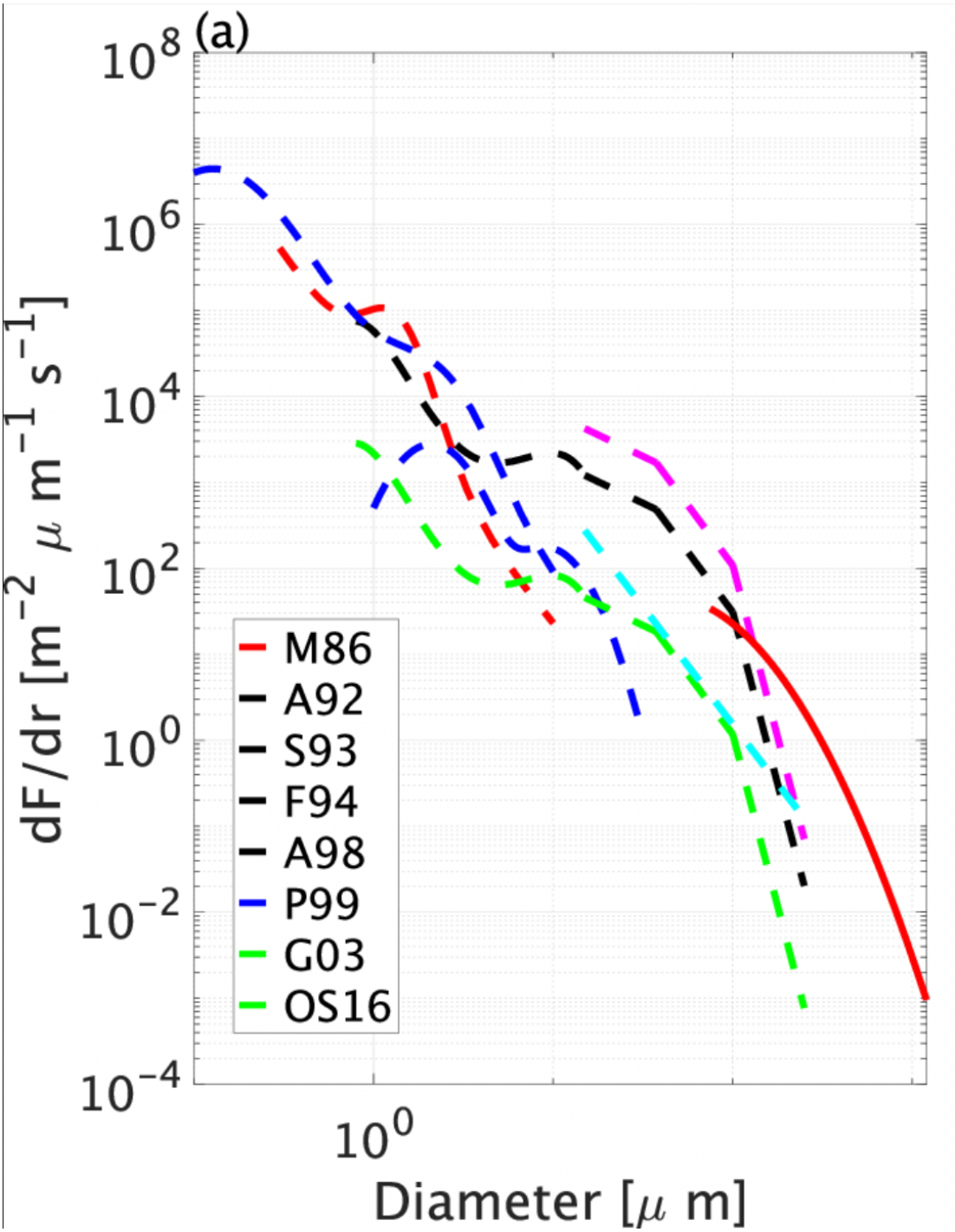

Figure 2.5: Drop size distribution of sea spray in previous studies. - M86: Monahan et al. (1986), A92: Andreas (1992), S93: Smith et al. (1993), F94: Fairall et al. (1994), A98: Andreas (1998), P99: Pattison and Belcher (1999), G03: Gong (2003), OS16: Oritiz-Suslow et al. (2016).

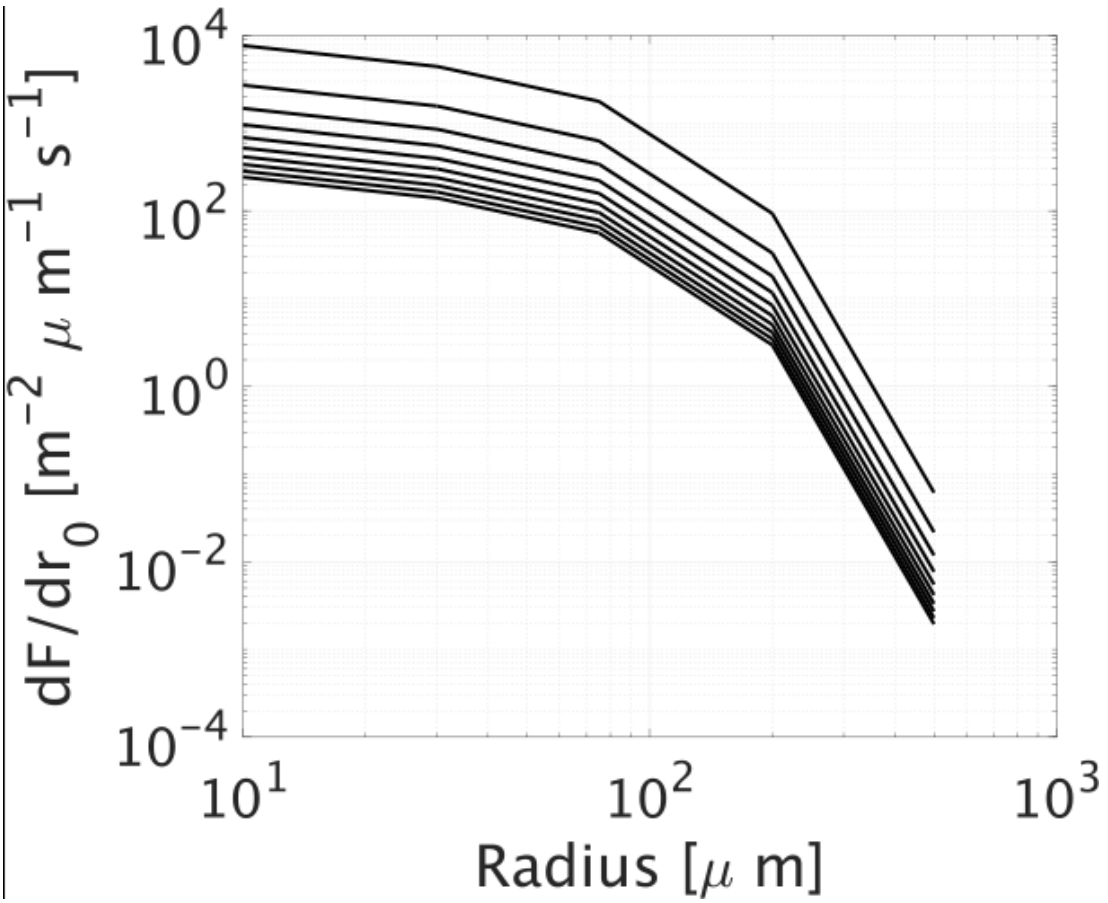

Figure 2.6: Drop size distribution of sea spray proposed by Wan et al. (2019) -

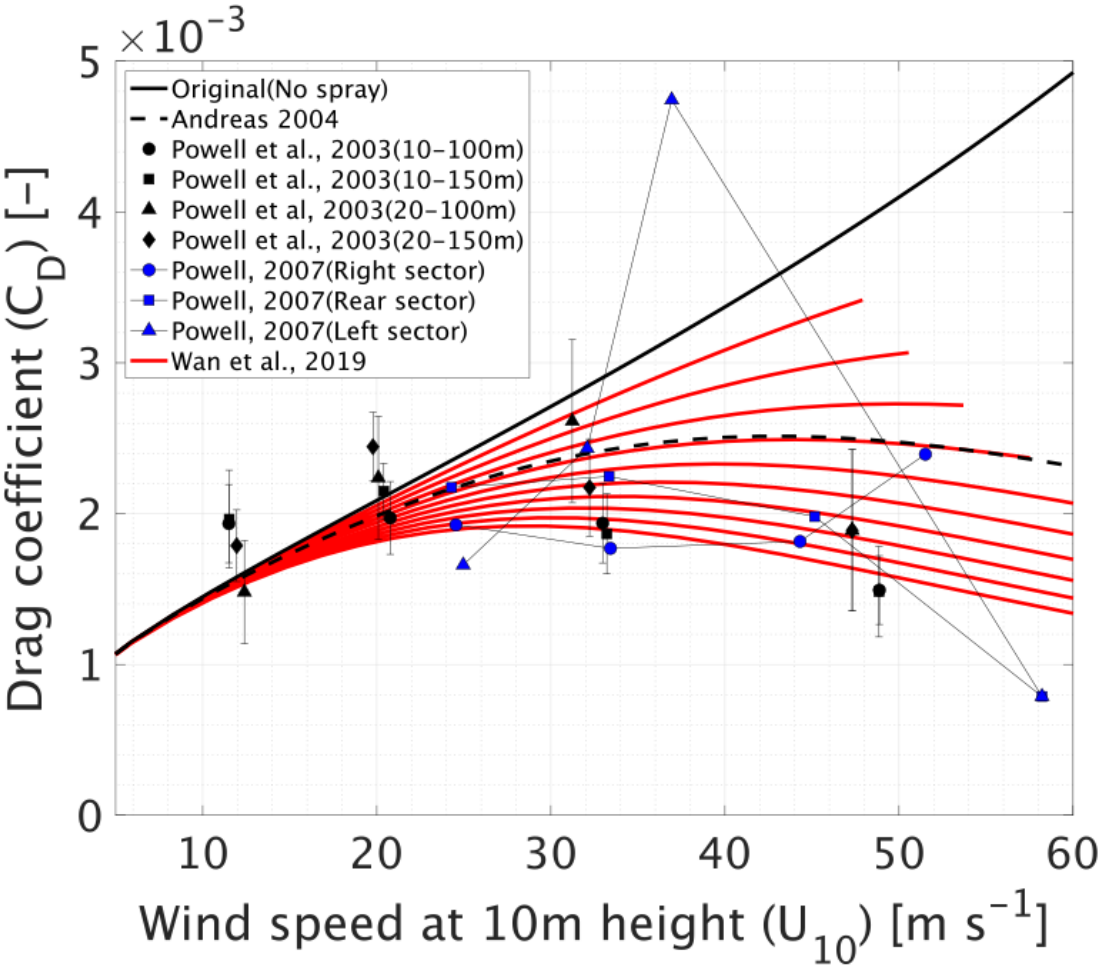

Figure 2.7: Relationship between the drag coefficient and friction velocity. - Black, Red and dashed lines are drawn based on parameterization. The other plots are observation results.

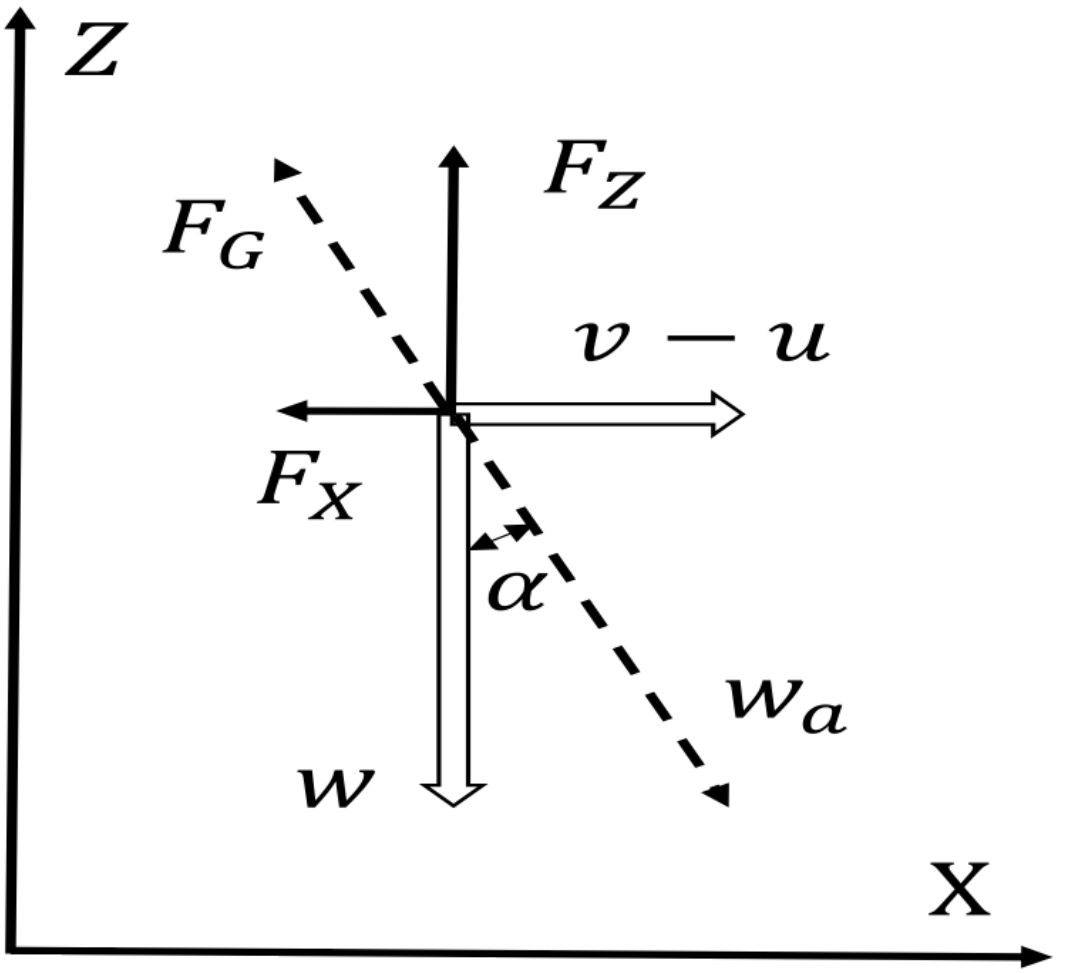

Figure 2.8: Force on a falling raindrop, velocity of the raindrop, and wind speed (Hogh-Schmidt, K. and Brogard, S., 1975). - F_G, F_x, F_z denote the frictional force on the raindrop and its horizontal and vertical components, respectively. w_a, w denote the oblique relative velocity of raindrops and its vertical component. v represents the horizontal velocity of raindrops, u represents the horizontal wind speed, and α represents the angle between w_a and w.

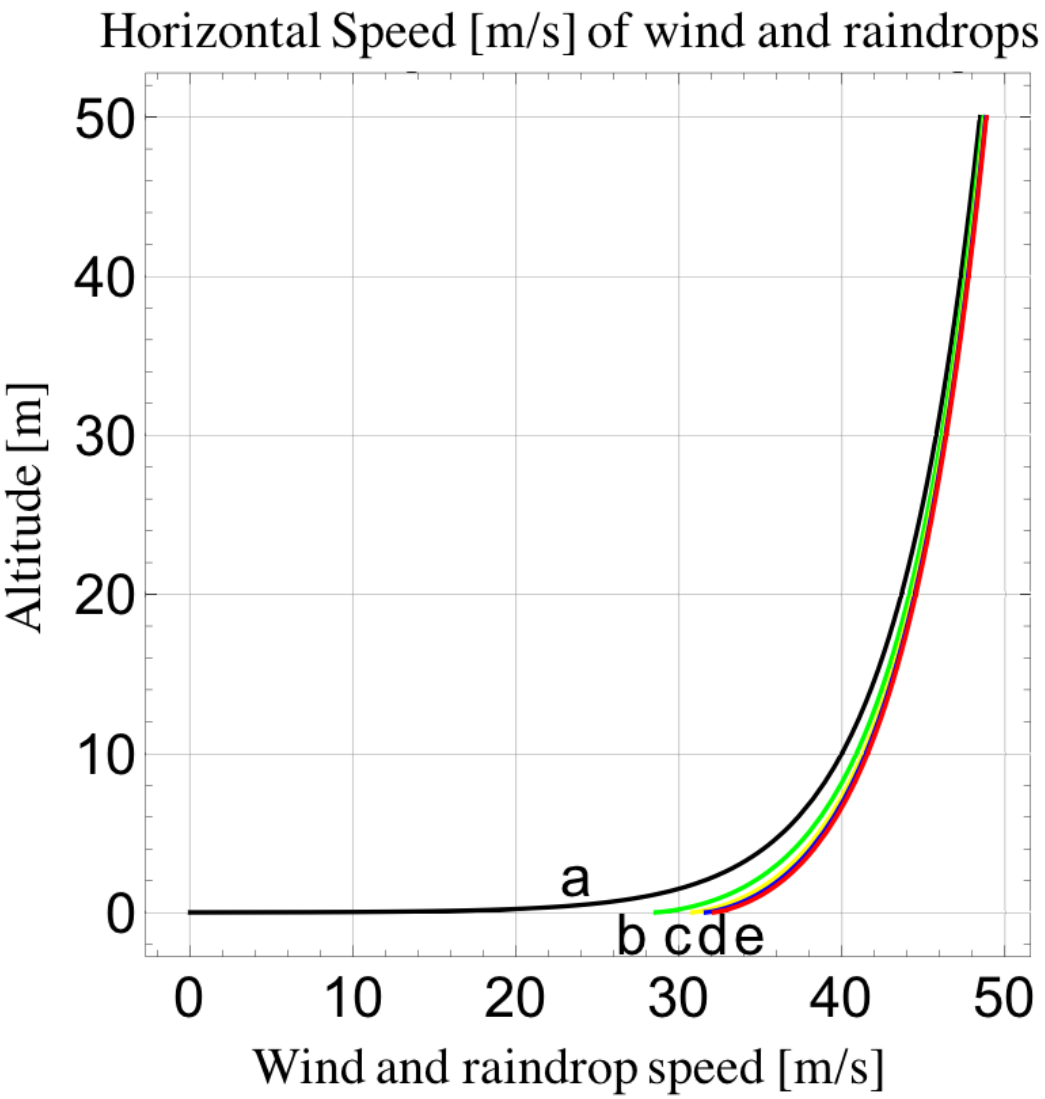

Figure 2.9: Vertical profile of the horizontal wind speed (black line) and horizontal velocity of raindrops by rainfall intensity - green: 10 mmh^{-1}, yellow: 40 mmh^{-1}, blue: 70 mmh^{-1}, red: 100 mmh^{-1}. Curve a shows the vertical profile of the horizontal wind speed, and curves b, c, d, and e show the horizontal velocity of raindrops by rainfall intensity (b: 10 mmh^{-1}, c: 40 mmh^{-1}, d: 70 mmh^{-1}, and e: 100 mmh^{-1}).

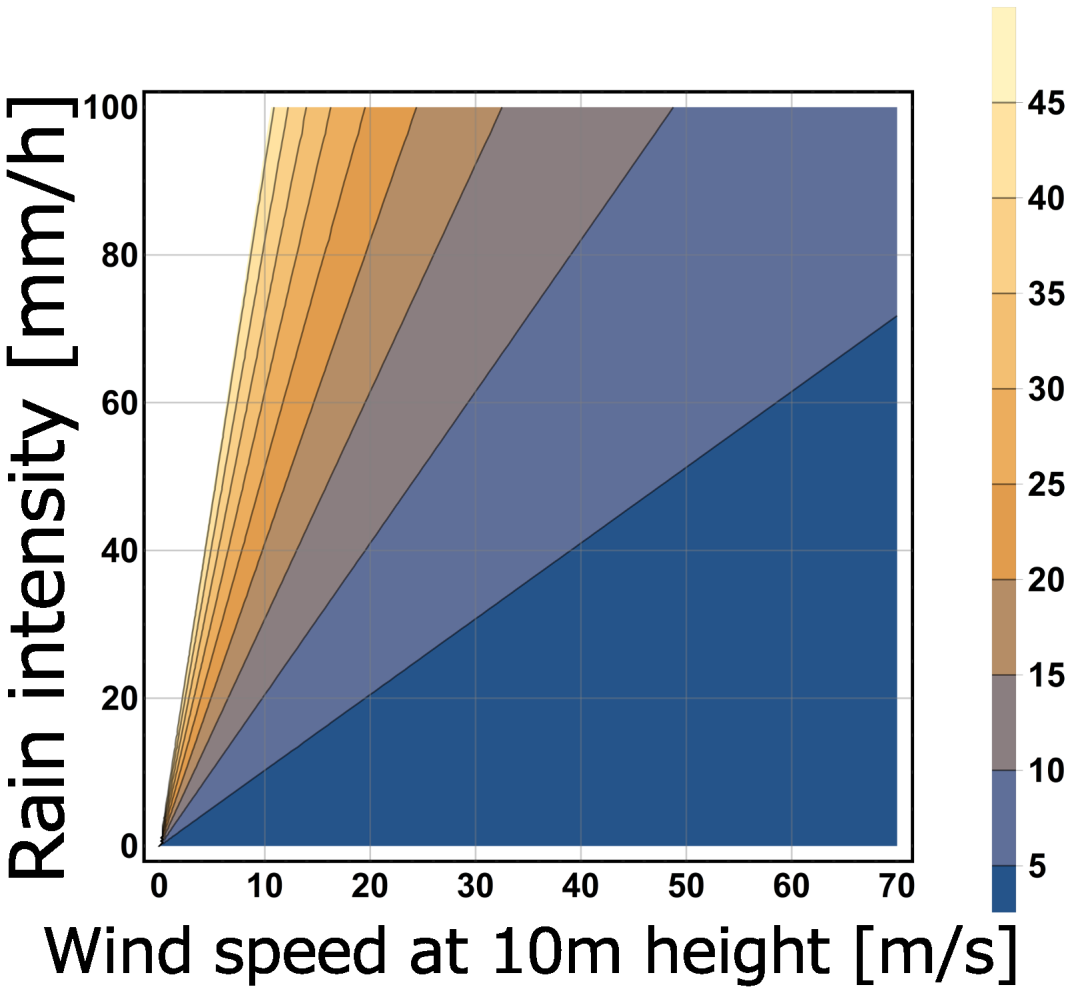

Figure 2.10: Relationship between wind speed, rainfall intensity and ratio of shear stress of rain against total shear stress - The relationship calculated from the ordinal drag coefficient (**Eq.** (2.3)).

3

Classification method of drop size distribution of sea spray and rain

3.1 Introduction: First observation

Rainfall observation using ground rain gauges and radars has been widely used for flood control plans, disaster prevention, and weather forecasting. The Japan Meteorological Agency (JMA) and the Ministry of Land, Infrastructure, Transport and Tourism (MLIT) have established approximately 2,500 observation sites in Japan using tipping buckets. In addition to rainfall observations, radar observations are used to estimate rainfall. The main radar rain gauges are the JMA C-Band meteorological radar with a temporal resolution of 10 minutes and a spatial resolution of 1 km, and the MLIT C-Band meteorological radar with a temporal resolution of 5 min and a spatial resolution of 1 km. Nowadays, these radars are replaced with multi-doppler radars and a state-of-art radar called a phased array radar. In rainfall observations using a meteorological radar, rainfall intensity is estimated from the radar reflectivity. The following equation, called the Z-R relation, is used for this estimation.

$$Z = 10 \log_{10} \sum_i N(D)_i D_i^6 \Delta D_i,$$

3. CLASSIFICATION METHOD OF DROP SIZE DISTRIBUTION OF SEA SPRAY AND RAIN

$$R = 3.6 \times 10^{-3} \frac{\pi}{6} \sum_i N(D)_i D_i^3 V(D)_i \Delta D_i,$$

where Z is the reflection intensity [dBZ], $N(D)_i$ is the number of particles of the ith particle size [$\mathrm{m^{-3}mm^{-1}}$], D_i is the particle size of the ith particle [mm], ΔD_i is the width of the ith particle size class [mm], R is the rainfall intensity [$\mathrm{mmh^{-1}}$], and $V(D)_i$ is the vertical terminal fall velocity of the particle [$\mathrm{ms^{-1}}$] for the i-th particle size. The estimated rainfall intensity varies depending on the number of particles relative to the particle size (henceforth referred to as drop size distribution: DSD). In recent years, with the introduction of multi-parameter radar, rainfall intensity has been estimated using the K_{DP}-R relation. A radar that can transmit and receive both horizontal and vertical polarizations simultaneously and can observe the inter-polarization phase difference is called a multi-parameter radar. The inter-polarization phase difference per unit distance is K_{DP} [$^{\mathrm{o}}\mathrm{km^{-1}}$]. Particle size distribution was expressed by Marshall & Palmer(52) using the following equation with two parameters.

$$N(D) = N_0 \exp(-\lambda D), \tag{3.1}$$

Here, N_0=0.08 [$\mathrm{cm^{-4}}$] and $\lambda = 41/R^{0.21}$[$\mathrm{mm^{-1}}$]. Ulbrich(85) describes this as the following:

$$N(D) = N_0 D^{\mu} \exp(-\lambda D). \tag{3.2}$$

Here, μ can be any positive or negative value, and the unit of the coefficient N_0 is[$\mathrm{m^{-3}cm^{-1-\mu}}$]. The raindrop drop size distribution varies with the parameter μ in the range of a particle size less than 1 mm, even when the rainfall intensity is constant, and the variation becomes smaller when the particle size is larger than 1 mm. The drop size distribution also varies with the collision and merging processes in cloud physics, and with cold and warm rain.(64).

The drop size distribution affects not only the rainfall itself but also the flux exchange in the atmospheric boundary layer. Theoretical analysis has investigated whether the momentum exchanged between the atmosphere and the ocean varies with wind speed and rainfall intensity due to the presence of raindrops and sea spray generated from the sea surface during storm conditions. This theory

extends the discussion of momentum exchange coefficients to include the effects of droplets proposed by Andreas(6) and allows the effects of raindrops and sea spray to be discussed simultaneously.

Friedrich et al.(28) conducted field observations using a disdrometer called Parsivel, which can measure raindrop size distributions. The disdrometer can measure the size, velocity, and number of particles that pass through the laser range of detection. However, the relationship between raindrop size and terminal fall velocity deviates when the wind speed exceeds approximately 10∼20 ms^{-1} (28). There are two possibilities for why raindrop diameter and terminal velocity deviate from the relationship when observed with a disdrometer. The first is that a particle passes through the edge of the detection range. The second is that the particle hits the instrument and is detected at a smaller size than it should be(35). Friedrich et al.(28) proposed a method to remove both data based on the relationship between raindrop termination fall velocity and particle size. At that time, observed data with wind speeds of 10 ms^{-1} or higher were excluded from the analysis because of their large deviations. However, typhoons, hurricanes, and other phenomena that cause strong rainfall have wind speeds of 10 ms^{-1} or higher. The accurate determination of the particle size distribution is important for rainfall estimation in radar observations.

In this study, we analyzed data that included observation results of wind speeds of 10 ms^{-1} and higher. The characteristics of the particle size distribution are presented. Section 2 presents an overview of the field observations, and Section 3 describes the change in the mass of raindrops removed based on the relationship between the terminal fall velocity of falling raindrops and the particle size. In Section 4, the dependence of the particle size distribution on the wind speed is described, and Section 5 provides a summary.

3.2 Drop size distribution of sea spray

This section describes the existing drop size distributions for sea spray. Previous drop size distributions have been obtained from field observations, wind tunnel experiments, and numerical experiments. Based on these observations,

droplets can be classified into three particle size scales. The particle size range is approximately 10^{-5} to 1 mm. 10^{-5} to 10^{-3} are film droplets, 10^{-3} to 10^{-2} are jet droplets, and 10^{-2} to 10^{0} are spume droplets.

The first observation of spray was made by Monahan (1986)(56). In their study, they determined that the amount of spray generation is proportional to the whitecap coverage. The white wave coverage is the percentage of the sea surface covered by white foam generated when waves break. Wu observed the amount of spray generated by a kite attached to a ship at sea. Andreas (1998)(5), using the observations of Wu (1993)(88) and Smith et al. (1993)(75), proposed a droplet particle size distribution that includes all particle size ranges up to a wind speed of 32 ms^{-1}. In contrast, Fairall (1994)(26) proposed a particle size distribution for spume droplets. The particle size distributions described above are only a part of the existing literature; various other proposals have been made and are summarized in **Figure 2.5**. In this figure, the wind speed at a height of 10 m is 15 ms^{-1}. As shown in this figure, the number of particles with a radius greater than 20 μm varies greatly. Andreas (2002) examined many particle size distributions and found that they strongly depend on the wind speed.

3.3 Marine observations

The field observations were carried out at an observation tower located 2 km off the Tanabe Bay in the southern Wakayama Prefecture. The observations were conducted using a robust disdrometer (OTT Parsivel; OTT HydroMet, Loveland, CO, USA) which can observe raindrops. The disdrometer uses a laser with a wavelength of 780 nm and a laser emission range of 27 mm depth, 180 mm width, and 1 mm height. The droplet diameter and velocity of the raindrop passing through the laser range are detected. The range of particle sizes and velocities that the disdrometer can detect are 0.062 ∼24.5 mm and 0.05 ∼20.8 ms^{-1}, respectively. The particle size and velocity are classified into 32 classes.

The map showing the observation location, whole view of the observation tower, and installation of the disdrometer is shown in **Figure 3.1**. **Figure 3.1** (a) is a map showing the locations of the observation towers (marked with stars).

Figure 3.1 (b), (c) show the whole appearance of the tower in the Tanabe bay and the installation of the disdrometer, respectively. In this study, the same disdrometer was installed at 10 and 15 m above sea level on the south side of the observation tower. Since the tower is 23 m above sea level and the installation position is lower than the top of the tower, there is a possibility that water droplets attached to the tower could fall and be detected by the disdrometer. Therefore, only the period when the wind is blowing from the south was used in this analysis. The southerly direction is defined as 45 ∼315 degrees when the angle is defined clockwise with north at 0 degrees. The observation periods were August 27, 2013 ∼November 27, 2013 (92 days) and July 22, 2014 ∼October 30, 2014 (100 days).

In 2013, 31 typhoons occurred in the North Pacific Ocean, and typhoons 17 and 18 approached the observation tower during the observation period. In 2014, there were 23 typhoons in the North Pacific, and typhoons 18 and 19 approached the observation tower during the observation period. A propeller-type anemometer is installed at a height of 23 m above the sea surface in the observation tower. A maximum wind speed of 26.2 ms^{-1} and a maximum significant wave height of 6.5 m were observed on October 6, 2014, when Typhoon Phanfone (No.18) approached. The observed data from 2013 is included in this analysis.

A time series of (a) hourly wind speed, (b) significant/maximum wave height and significant wave period (b), and (c) rainfall intensity estimated from the Radar-AMeDAS reanalysis data and disdrometer at both heights from September 14–17 is shown in **Figure 3.2**. During this period, Typhoon 18 passed the observation site. The maximum wind speed at this time was approximately 20 ms^{-1}, and the maximum wave height reached approximately 5 m. The Radar-AMeDAS reanalysis data has a 1 km mesh spatial resolution and 30-minute averages of the rainfall before 1 h obtained by combining AMeDAS rain gauge observations and meteorological radar observations. Rainfall is indicated by discrete representation, e.g., a value of 0 mmh^{-1} indicates rainfall between 0 mmh^{-1} and 0.4 mmh^{-1}. As shown in this figure, the timing and values of the analyzed rainfall and the rainfall intensity obtained from the disdrometer are generally consistent. In addition, **Figure 3.2** (a), (c) shows that the peaks of wind speed and rainfall shifted. The ratio of the time when the disdrometer showed no rainfall to the time when

the analyzed rainfall was less than 0.4 mmh^{-1} was 95.3 %. Therefore, the rainfall data and the disdrometer can be used to estimate the rainfall at this location. Histograms of wind speed and wave height are shown in **Figure 3.3**. **Figure 3.3** (a) shows the maximum and average wind speed, **Figure 3.3** (b) shows the maximum and average wind speed observed in the absence of rainfall, **Figure 3.3** (c) shows the maximum and significant wave height, and **Figure 3.3** (c), (d) shows the frequency distributions of the maximum wave height and the significant wave height, respectively. The histograms show that there were strong wind speeds and high wave heights even when our analysis was conducted only during a no-rainfall period.

3.4 Impact of high wind speeds on the disdrometer

The disdrometer used in this observation may shift in relation to the particle size and the velocity of the falling raindrop under high wind conditions.(29)**.** Since some of the observations deviated from the drop size distribution when the wind speed is higher than 10 ms^{-1}, Friedrich et al., (2013)(29) removed the data at that time. The horizontal axis shows the diameter, vertical axis is the terminal fall velocity, and gray scale shows the number of particles in **Figure 3.4**. The curved line shows the relationship between the diameter and terminal fall velocity(33)**.** **Figure 3.4** (a) shows the one-hour average of the number of particles observed when the wind speed was below 10 ms^{-1} observed by the propeller anemometer installed in the observation tower. **Figure 3.4** (b) is the same as (a) but with wind speeds above 10 ms^{-1}. A comparison between the two shows that particles observed at wind speeds of 10 ms^{-1} or higher are classified as deviating significantly from the relationship between particle size and fall velocity. The same characteristics were obtained in the 2014 observation results. Based on previous studies, we can estimate the following three situations. (i) Misclassification by high wind speed, (ii) when a particle passes through the edge of the laser detection range, the particle is detected as smaller than its original size, and (iii) when particles collide with an instrument and small split particles

are detected.

To remove the second and third situations, in a previous study, only the particles classified within ± 60 % of the relationship between the particle size and the terminal velocity of raindrops were included in the analysis(29). Jaffrain and Berne(37) verified the amount of rainfall removed due to the particles eliminated by the above method against the total observed rainfall. In this study, 3.5 % of the total rainfall was removed during the period of 15 months. Conversely, when comparing the results of the disdrometer and the tipping bucket, the total rainfall of the former was 4.3 % lower than that of the latter. Therefore, the removal of particles due to the deviation from the relationship has little effect on the reduction of rainfall intensity.

Friedrich et al.(29) removed cases above 10 ms^{-1} to remove the effect of high wind speeds. However, in this study, the same method was applied to wind speeds of 10 ms^{-1} or higher because of the importance of the drop size distribution at high wind speeds. The following analysis was conducted to examine the threshold for the terminal velocity. The hourly rate of volume conducted of particles classified within the range of ±20 %, ±40 %, ±60 %, ±80 % of the terminal fall velocity against the whole observed volume was calculated for each wind speed. The results are shown in **Figure 3.5**. The horizontal axis shows wind speed [ms^{-1}], and the vertical axis shows the rate ((a) ± 20 %, (b)±40 %, (c)±60 %, (d)±80 %) The white circles are mean values. The dashed line is 80 %; all mean values except (a) exceed 80%. This analysis shows that the method of Friedrich et al.(29) is applicable at up to 14 ms^{-1} wind speed. In this study, we extracted particles that are within ±60 % of the relation between the particle size and the fall velocity, as in Friedrich et al.(29)

3.5 Impact of wind speed on drop size distribution

3.5.1 Classification method based on the slope of the drop size distribution of rain

In this section, after extracting the data using the method described in the previous section, the dependence of the drop size distribution on the wind speed is discussed. The following equation was used to convert the observed data into the number of particles per unit volume and particle size $N(D)$.

$$N(D,v)_{ij} = \sum_{ij} 10^6 \frac{n(D,v)_{ij}}{180 \times (30 - 0.5D_i)v_j \Delta D_i \Delta t}$$

where, $n(D,v)_{ij}$ is the number of particles classified into the representative size and velocity observed by the disdrometer, D_i is the representative size of the i-th bin [mm], ΔD_i is the width of the i-th bin [mm], v_j is the representative velocity of the j-th bin, and Δt is the observation unit time, 3600 s(28). The drop size distribution for each wind speed when radar-AMeDAS reanalysis shows 2 mmh^{-1} is illustrated in **Figure 3.6**.

The legend indicates the observation height, and (**a**)∼(**d**) indicates the wind speed of 0∼5, 5∼10, 10∼15, and 15∼20 ms^{-1}. For both disdrometers installed at a height lower than the top of the observation tower, water droplets attached to the tower may fall and be detected. Therefore, the possibility was eliminated by analyzing only the period when the wind was blowing from the south. When the wind speed was 0∼5 ms^{-1}, the number of particles was the same, but when the wind speed was 15∼20 ms^{-1}, the number of particles at 10 m height was larger than 0.687 mm in diameter.

The raindrop particle size distribution was expressed by Marshal& Palmer(52) using two parameters. In addition , Ulbrich(85) used three parameters as shown in **Eq.** (3.2). μ is an arbitrary real number. The raindrop particle size distribution varies depending on μ in the range of particle size less than 1 mm, even when the rainfall intensity is constant, and the variation disappears when the

particle size is larger than 1 mm. Therefore, we classified the data obtained by observation considering that the variation is small in the range of particle sizes larger than 1 mm. We calculated the volume of particles detected in the range of 1∼3 mm in diameter and classified the data according to the obtained values. The distribution of particle size by wind speed is shown in **Figure 3.7**. The figure shows that the number of particles increased at a wind speed of 10∼20 ms^{-1} from 0∼10 ms^{-1}. This feature was more pronounced for particles smaller than 1 mm in diameter. This difference changes the parameter μ of the function representing the raindrop size distribution in **Eq.** (3.2). For fitting to the existing Ulbrich's equation, the obtained parameter μ of the raindrop size distribution varies from -0.85 to 72.9. In the Z-R relation of radar observation, the former is the rainfall intensity and the latter is the rainfall intensity even if the same reflection intensity Z is obtained. In addition, the range of particle size less than 1 mm partially overlaps with the range of particle size of wave breaking spray generated from the sea surface. Previous studies have shown that the particle size scale of wave breaking splashes exists in the 10^{-2}∼10^{0}mm scale, which was superimposed on the present analysis. The observations made in this study were made at sea, and this may be why the number of particles with a diameter of less than 1 mm increases when the wind speed is high. Therefore, when considering the raindrop size distribution at sea, it is necessary to account for the mixture of breaking waves and droplets. In the next section, the dependence of the raindrop size distribution on the wind speed is shown in the absence of rainfall estimated using the analytical rainfall.

3.5.2 Classification method based on the radar-AMeDAS reanalysis rainfall data set

In this section, we used the radar-AMeDAS analyzed rainfall to estimate the no-rain time during the observation period and investigate the dependence of the particle size distribution on the wind speed. This method extracts the grid data of the observation tower, and defines the no-rainfall time as the time when the rainfall rate is less than 0.5 mmh^{-1}. After estimating the no-rainfall time, the particle size distribution by wind speed [$m^{-3}mm^{-1}h^{-1}$] was calculated

using the particle size, particle number, and wind speed data observed by the disdrometer during that time. The results are shown in **Figure 3.8**. The figure shows that the number of particles increased with the increase in wind speed. In addition, as in the previous section, the parameter μ in Ulbrich's equation changes from -0.85 to 76.9(72). In the Z-R relation, the former is mmh^{-1} and the latter is mmh^{-1} for the same reflection intensity. The number of particles with a diameter of less than 1 mm increased significantly at a wind speed of 10∼20 ms^{-1}. The number of particles for the particle size obtained in this observation showed a characteristic of increasing with wind speed. In addition, the particle size distribution of particles with a diameter of less than 1 mm showed a remarkable feature.

3.6 Summary

The field observations in this study were carried out at an observation tower located 2 km off the Tanabe Bay in the southern Wakayama Prefecture. The tower was equipped with two disdrometers, one at a height of 10 m and the other at 15 m above the sea surface. A comparison of the results obtained from the two instruments showed that the number of particles with a diameter of less than 1 mm detected at a height of 10 m was higher. By removing any particles that deviate from the relationship between the particle size and the terminal velocity of raindrops as described by Friedrich et al.(29), it is possible to eliminate (i) the effects of particles that break up on impact with the instrument, (ii) particles that pass through the edge of the detection area, and (iii) misclassifications that are observed in high winds. In this study, we confirmed that the applicability of the method can be extended to wind speeds of 14 ms^{-1}. Calculating the rainfall intensity conducted within ± 60 % of the raindrop terminal velocity results in a rainfall intensity that is approximately 80 % of the total rainfall intensity calculated from all particles detected by the disdrometer. The drop size distribution can be expressed by **Eq.** (3.1) and **Eq.** (3.2) proposed by Marshall and Palmer(52) and Ulbrich(85), respectively. The shape of the drop size distribution in the range of 1 mm or less in diameter changes depending on the parameter μ.

The number of particles with a diameter of 1 mm or more is relevantly constant for a given rainfall intensity, regardless of the parameter in the particle size distribution of equation (3.2). After classifying the data using this feature, the particle size distribution by wind speed was calculated. The number of particles with a diameter of 1 mm or less is larger at a wind speed of 10∼20 ms^{-1} than at a wind speed of 0∼10 ms^{-1}. The same characteristics were obtained by calculating the distribution of raindrop size by wind speed only during the no-rainfall period. In other words, wind speed changes the parameter μ in raindrop size distribution. In addition, this variation is likely to be due to the detection of particles other than raindrops. Since the observation was made at sea, it may be sea spray generated by breaking waves from the sea surface. Therefore, it is necessary to consider the variation of the drop size distribution depending on the wind speed, because observations at sea may detect wave breaking droplets originating from the sea surface. Furthermore, it is difficult to directly observe wave breaking droplets at sea, and the amount of droplet generation is not yet known; however, the results of this study suggest the possibility of direct observation of droplets in this field. In the future, it is necessary to examine the particle size distribution considering the mixing of droplets shown in this study. In addition, direct observation of droplets at sea should be continued to establish the dependence of droplets on wind speed and the separation method from raindrops, and to clarify the particle size distribution of both.

3.7 Introduction: second observation

Rainfall measurement over the open ocean plays a leading role in our understanding of the global hydrological cycle, and validates satellite precipitation and global climate models (90)-(34). During storms, rainfall intensities measured by tipping-bucket rain gauges over the open ocean (e.g., on ships) are addressed by including both rain droplets and sea spray ((74)). Remarkably, sea spray exists even on land; however, during severe typhoons (e.g., TRAMI of 2018, associated with a maximum instantaneous wind speed of 42 ms^{-1} at Choshi in the Kanto region of Japan), tiny droplets of sea spray have been blown to Tsukuba city,

located 50 km from the Pacific coast, resulting in salt damage (89). Notably, sea spray affects momentum as well as latent and sensible heat fluxes within the context of air-sea interactions (62)-(10), and rain droplets play an indispensable role in flux exchanges (17), (18).

Small rain and large sea spray droplets co-exist in the diameter class of less than 1 mm, and this has made distinguishing them difficult in practice. To estimate the proportion of sea spray to total rainfall, salinity measurements of water collected in a rain gauge have been performed (74). Yet, this observation underlined the limitation of rain containing dissolved dry salt (reviewed in (90)). Thereby, the gauge was placed at least 16 m above the water level so that the proportion of sea spray was minimized. Alternatively, the proportion of sea spray was minimized by placing the gauge at least 16 m above the water level (reviewed in (90)).

To distinguish between sea spray and rain droplets, the characteristics of rainfall intensity and the number of rain droplets of various diameters (the drop size distribution [DSD]) needs to be analyzed. It is important to clarify the relationship between rainfall and the number of rain droplets of various diameters, e.g., the drop size distribution (DSD). DSD is used in conjunction with multi-doppler polarization systems to estimate rainfall intensity from radar reflectivity data, using the Z-R relationship for weak rainfall and the Kdp-R relationship for heavy rainfall. It highlights the correlations between rain intensity and Z (radar reflectivity), as well as between rain intensity and Kdp (specific differential phase shift of radar). The first and most well-known DSD model, the Marshall-Palmer distribution (52), was used for the DSD first proposed in (85). The Marshall-Palmer distribution was derived from observations of rain droplets with diameters 0.1 to 5 mm spreading on dyed filter papers. Later, other equations were developed to characterize DSD denoted by log-normal, Weibull, exponential, and gamma and general gamma distributions (including log-normal, Weibull, exponential, and gamma and general gamma distributions). The latter usefully describes the drizzle mode and distributional tail of large droplets (54)-(80). Among them, the Ulbrich distribution (85) is known as a special case of the general gamma distribution and has been widely used to analyze rainfall, as it allows for DSD flexibility when the diameters are less than 1 mm. At certain

rainfall intensities, the number of droplets less than 1 mm in diameter varies significantly compared to that of larger droplets. Such variations reflect the type of rainfall and the seasonality ((72)-(67)). The DSD of Ulbrich (85) features a shape parameter μ, and f. For an open-ocean rainfall measurement, μ indicates the probability that the DSD variation of small-diameter droplets is affected by sea spray.

The Ulbrich distribution is expressed as:

$$N(D) = N_0 D^{\mu} \exp(-\lambda D), \tag{3.3}$$

where N(D) is the number of droplets in diameter D (cm), N0 is 8×10^4 expressed in $m^{-3}cm^{-1-\mu}$, and μ (non-dimensional) and Λ [cm^{-1}] are shape parameters. Λ varies by the rainfall intensity R mmh^{-1} and is therefore assigned to; here , it is set to $\Lambda = 4.1 \times R^{-0.21}$. These two parameters N_0 and Λ are selected from Marshall and Palmeter (1948)(52). When $\mu = 0$, the equation is equivalent to the Marshall-Palmer distribution. Previous studies recorded variations in the diameter range, as well as seasonal changes in the DSD shape parameters μ and Λ. For example, one study reported that μ varies from -0.85 to 76.9 (although it is generally positive) and Λ ranges from 3.3 to 591.5 cm^{-1} (72). When the shape parameter μ varies from -1 through 0 to 1, we proposed two cases to investigate the proportion of small droplets (0.072 to 1.000 mm; this range corresponds to the detection limit of the disdrometer) with respect to the total rainfall intensity. First , as the total rainfall intensity reached 10 mmh^{-1}, the proportions of small droplets were 72%, 17%, and 2%, as determined by **Eq**.(3.3). Second, as the total rainfall intensity reached 50 mmh^{-1}, the proportions of small droplets were 40%, 6%, and 0.8%. The results revealed that light rainfall intensity was dominated by small droplets. This indicated that small droplets were associated with light rainfall intensity.

Sea spray observation over the open ocean was first described in (56). Several studies have highlighted the significance of sea spray generation at the air-sea interface by investigating the effect of rainfall on sea spray generation (50), (20); however, these results have been contradictory. Some believe that sea spray is generated predominantly by rainfall (50), while others note that heavy rainfall can suppress significant wave height (20), suggesting the suppression of sea spray

generation by rainfall. Moreover, wet and dry deposition and scavenging efficiency can be influenced by rain and sea spray (45). Following this line of research, not only the effect of rainfall but also the whitecap formation time, decay time (19), and sea state (59) may have an impact on the generation of sea spray. Sea water temperature could be a key element according to laboratory experiments showing that high temperatures lead to low production of sea spray (68). Moreover, there is a relationship between whitecap formation time and decay time with sea spray generation (45), and between sea state and sea spray production (19). Laboratory experiments have revealed that higher sea water temperatures lead to low sea spray production (59). Remarkably, wind-tunnel experiments have been carried out at high horizontal wind speeds, ranging from 36 to 54 ms^{-1} (68). A new observation system proposed in (51) provides an overview of the relationship between surface-generation noise and sea spray aerosols. These findings may help better understand the potential role of sea spray in the air-sea interaction; however, details of these studies are beyond the scope of our study.

Sea spray generally has three types of droplets: film droplets (0.00001 ∼0.1 mm), jet droplets (0.001∼0.1 mm), and spume droplets (0.01∼1 mm) (86). Here, we focused on spume droplets, although the size class of 0.072 to 1.000 mm is exceptional in (51). Compared to the other types of droplets, spume droplets facilitate a greater transfer of heat and moisture across the air-sea interface in a rapid manner. A wind speed over approximately 7-11 ms^{-1} is typically required to generate such droplets (4), which are ripped off wave crests by wind, principally via the bag-breakup fragmentation first described in (32). The DSDs of sea spray have been extensively studied (4), (3), while one review considered the DSDs of spume droplets (figure 6 of (4)) at a wind speed of 15 ms^{-1}. The DSDs were obtained at a wind speed of 15 ms^{-1}. From the figure, the number of spume droplets spanned two orders of magnitude. The review paper(86) introduces three types of DSDs of spume droplets (57) (5). One of them was proposed by observational data and the others were based on results obtained from theoretical analysis and a wind-tunnel experiment, although all publications mentioned that there was still a lack of data describing DSDs of spume droplets.

The diameter of rain droplets ranges from approximately 0.1 to 5 mm and the diameter of large sea spray droplets ranges from 0.01 to 1 mm. Thus, in

the diameter range below 1 mm, both droplets co-exist. Here, we performed a series of observations using a state-of-the-art disdrometer at a marine tower off the coast of the Wakayama Prefecture in Japan. The observational period ran from August to October in 2019, including a day during which a typhoon passed nearby. The proportions of sea spray to total rainfall measured by a tipping-bucket rain gauge were used to derive sea spray DSDs as a function of horizontal wind speeds. In Section 2, our observations, the use of the disdrometer, and the data correction methodology are described. The results of our observations are presented and discussed in Section 3, and a summary of our findings is presented in Section 4.

3.8 Methods

3.8.1 Site and data collection

A series of observations were conducted using a disdrometer called an SPC (Niigata Electric (42)), an anemometer, a time-lapse camera, and a tipping-bucket rain gauge installed on an observational tower maintained by the Disaster Prevention Research Institute of Kyoto University (33 ° 42'32"N, 135 ° 19'58"E) at a vertical height of 15 m above sea level. This height is higher than the one set in (50), so we did not consider the increase of sea spray generation by rainfall. The tower lies 1.8 km from off the coast (see the two-headed arrow in **Figure 3.9** (a)). We validated all wind speed and rainfall measurements by comparing them with data obtained from an automated meteorological data acquisition system (AMeDAS) weather station, which was located 4 km south of the tower; this station is maintained by the Japan Meteorological Agency ((38)). This station was equipped with a tipping-bucket rain gauge with resolution, 0.5 mmh^{-1}. We conducted continuous observations during two rainfall events, from August 14 to 16 and October 17 to 19, 2019. These periods included the extreme event of Typhoon Krosa.

3.8.2 Disdrometer

Disdrometers were initially used to detect snow particles(70). The disdrometer used in this study was modified by Niigata Electric (42) to detect water droplets with both vertical and horizontal trajectories. Here, the history and the modification of the disdrometer are introduced based on the reviewed paper (58). The first-generation disdrometer from 1977 (42) detected snow particles. With reference to the conventional approach, a small tungsten lamp with a hood emitted light in one arm, and another arm with two phototransistors was fixed on the same optical axis, where snow particles passed through the area between the emitter and the receiver. Moreover, the phototransistors output signals reflecting particle sizes (assuming that the particle is a sphere) in a spherical form (42). This allowed the disdrometer to detect not only snow (79), (69) but also sand (55) and water droplets on the upper deck of an icebreaker (61), (60). However, this underestimated snow particle numbers by 20% compared to a fabric trap (71). Thus, the disdrometer we used featured a self-steering wind vane with a super-luminescent diode sensor to enable stable output signals. Each signal was classified into 1 of 64 diameter classes between 0.072 and 1 mm every second to deduce the size of the particles passing through the sampling area (3×25×1 mm). To calibrate the disdrometer, thin wires with different diameters were passed vertically through the sampling area in accordance with a previous study (69). The calibration pointed out a measurement error related to the diameter sizes ± 15 μ m but not to the number of droplets, which was not reported in previous studies (79),(60). In addition, the raw data contained systematic errors, due to ambient temperature and detector lens pollution by dust; however, water particles, including rain and sea spray, were successfully detected. The maximum and minimum threshold droplet numbers were set to 1000 s^{-1} and 10 h^{-1}, respectively, and thereafter the DSD was calculated as follows:

$$N(D_i) = n(D_i)/(A \times \Delta t \times v(D_i) \times \Delta D_i). \tag{3.4}$$

where $n(Di)$ represents the number of raindrops in diameter class i, D_i represents the mean of diameter class i, A represents the sampling area of the particle counter surface (= 0.000025 m^2), dt represents the sampling time (= 3600 s), $v(Di)$ is

the terminal fall velocity of rain with diameter, and D_i is the diameter interval between the two successive classes, i and i+1. Following this calculation, the rainfall intensity contributed by small droplets (hereafter, R_{SPC}) was determined. Using this DSD, we calculated the rainfall intensity contributed by small droplets detected by the disdrometer (hereafter, R_{SPC}).

3.8.3 Data correction for tipping bucket

Errors associated with the rainfall measurements included wetting loss, evaporation, splashing of water into and out of the rain gauge, and wind-induced undercatch. Undercatch occurs due to deformation of the local wind field by the rain gauge, resulting in changes in raindrop trajectory; the effect of this phenomenon (examined by comparing reference gauges - installed in pits to minimize wind deformation - with above-ground gauges) is typically 2%–10%. The reference gauges were installed in pits to minimize wind deformation. The rain gauge data was adjusted using a commonly used empirical model followed by a later modification (27), as shown below.

$$R_{ctb} = k \times R_{tb}.$$

where a (= -0.042303), b (= 0.00101), c (= 0.018177), and d (= 0.043931) are empirical parameters (27) and R_{tb}, R_{ctb}, and u are the rainfall intensity yielded by the rain gauge, corrected rainfall intensity, and horizontal wind speed, respectively. This method is conventionally used to reduce the wind-induced effect.

3.8.4 Estimation methods

We first calculated the rainfall intensity of small droplets (diameter, 0.072–1.000 mm) using the empirical function of **Eq**.(3.3) and compared this to the R_{SPC}. In this analysis, the parameters of **Eq**.(3.3) were set to $N_0 = 8 \times 10^4$ [$\mathrm{m}^{-3}\mathrm{cm}^{-1-\mu}$ and $\Lambda = 41 \times R^{-0.21}$. To calculate the parameter $\Lambda(= 4.1 \times R^{-0.21}$, R_{tb} and R_{ctb} were substituted into R. The results followed the $Rr(D < 1)$ and $Rc(D < 1)$ values of **Figure 3.10** in which the shape parameter μ was set to -1, 0, and 1. Here, $Rr(D < 1)$ and $Rc(D < 1)$ reflect the calculation results of

rainfall intensity contributed by small droplets using different rainfall data sets (R_{tb} and R_{ctb}), respectively.

Our second analysis evaluated the properties of parameters Λ and μ in **Eq**(3.3). μ was estimated using the least-squares method as shown in **Figure 3.11**. N_0 was set to $8 \times 10^4 \mathrm{m}^{-3}\mathrm{cm}^{-1-\mu}$. Afterwards, a time series of the shape parameter from Eq (3.3) was obtained. The root mean squared error between this equation and the observation data was 7.4x106. The root mean logarithmic error and the coefficient of determination were 77.4 and 0.63, respectively.

Furthermore, the DSDs of rain and sea spray were calculated based on the collected disdrometer data. Although Eq (3.4) was utilized to calculate the DSD of rain, the following equation was used for the sea spray calculation.

$$F(D_i) = \frac{n(D_i)}{A \times \Delta t \times \Delta D_i},$$

The unit of F(Di) is $\mathrm{m}^{-2}\mathrm{s}^{-1}\mathrm{cm}^{-1}$.

3.8.5 Results and Discussion

The present experiments were conducted using a disdrometer, which was specially designed to detect water droplets over the open ocean. The experimental design is visibly illustrated in **Figure 3.9** (see Methods for more details). Time series data of rainfall intensity and cumulative rainfall were plotted based on the observations from August 14 to 16, 2019. Although the data obtained in both August and October, 2019 (JST), were assessed in this study, time series data of rainfall intensity and cumulative rainfall were only available from August 14 to 16, 2019 (JST) (see **Figure 3.10**). The results showed that R_{ctb} was 1.32-fold greater than R_{tb} using the correction method, which tended to increase the R_{ctb} values obtained under strong windy conditions (see **Figure 3.11** (a)) and light rain. R_{tb} and R_{ctb} were 0.82- and 1.13-fold greater, respectively, than the rainfall intensity detected at the AMeDAS station (R_{AMe}). The R_{SPC} followed the rises and falls in R_{tb} and R_{ctb}. The results of (Rr (D < 1) and Rc (D<1)) mentioned in section 2.4 are indicated by the blue and green areas. Compared to Rr (D<1) and Rc (D<1), RSPC fell within the range of μ = -1 to 1. The green circles and triangles are Rr (D < 1) and Rc (D < 1) with the shape parameter μ = 0,

which is equivalent to the Marshall-Palmer distribution. The left axis shows the cumulative rainfall for each component (R_{tb}, R_{ctb}, R_{SPC}, Rr (D > 1), and Rc (D > 1)) from 00:00 on August 14 (JST). During light rainfall at 13:00 (JST) on August 15, accumulative R_{SPC} recorded the cumulative R_{tb} and R_{ctb}. However, during heavy rain after 14:00 (JST) on August 15, the cumulative R_{tb} and R_{ctb} recorded drastic increases, leading to a large difference between the cumulative $R_{tb/ctb}$ and R_{SPC}. **Figure 3.11** (a) shows the time series of the hourly horizontal wind speed R_{tb}, R_{ctb}, and R_{AMe}, which are total rainfall measured by the tipping bucket at the tower and the AMeDAS station. Wind speed and rainfall intensity increased as the typhoon approached; however, the wind speed at the AMeDAS station decreased earlier than that at the tower , as the AMeDAS station was located further south. The rainfall intensity reached its peak when the wind speed decreased. Furthermore, the volume and total number of hourly droplets in the range of 0.072 to 1.000 mm in diameter were measured by the disdrometer at the tower, and both showed an increasing trend (**Figure 3.11** (b)). The hourly total number and volume of rain droplets recorded by the disdrometer exhibited the same increasing trends (**Figure 3.11** (b)). The shape parameter μ varied from -2.53 to 0.33 during this period and decreased monotonically as the wind speed increased (**Figure 3.11** (c)). Although the rainfall decreased after 16:00 on August 15, μ continued to decrease during this period. Regarding the Ulbrich distribution, the number of small droplets less than 1 mm in diameter increased while that of large droplets decreased.

Figure 3.12 shows the time-lapse photographs of the sea surface conditions at the time points indicated by the arrows in **Figure 3.12** (a-d). In **Figure 3.12** (a), R_{tb} and R_{ctb} were 1 and 2 mmh^{-1}, with 1,978 droplets per hour and a volume of 122.1 mm^3h^{-1}, suggesting that the sea was calm. In **Figure 3.12** (b), whitecaps were visible at a wind speed of 18.2 ms^{-1} and the rainfall intensities (R_{tb} and R_{ctb}) were 8.5 and 13.4 mmh^{-1}, respectively. In **Figure 3.12** (c), the sea surface was covered with sea spray and streamlines were visible, such that droplets recorded by the disdrometer must have included sea spray. After the rainfall ended, some whitecaps remained (**Figure 3.12** (d)). From the time-lapse photographs, the disdrometer was not covered with waves, and the maximum significant height was 4.23 m during the observation periods. The data sets were

thus not directly influenced by waves.

Figure 3.10, 3.11, 3.12 demonstrate that rain and sea spray droplets less than 1 mm were detected by the disdrometer. To derive the proportions of small droplets against total rainfall, the relationships between R_{ctb} and R_{SPC} are drawn in **Figure 3.13** in conjunction with the three lines based on the DSD of **Eq**.(3.3). According to the data obtained from August to October, small droplets dominated the total rainfall during light rain. Nonetheless, the proportion was small during heavy rainfall. At wind speeds less than 5 ms^{-1}, the relationship followed the Marshall-Palmer distribution (red line), although R_{SPC} increased when R_{ctb} remained constant and the wind speed increased. Thus, the proportion of small droplets to total rainfall increased, reflecting the increasing amounts of sea spray as the horizontal wind speed increased. We hypothesized that the proportion of small droplets to total rainfall varies depending on the properties of sea spray. In the context of rain DSDs, this characteristic is important to estimate the real rainfall intensity, as the μ varies depending on the amount of sea spray generated (**Figure 3.13**).

To investigate the proportion, the DSDs of sea spray need to be discussed. **Figure 3.14** shows the DSDs of rain and sea spray derived by the disdrometer during two periods - August and October, 2019 - without rainfall monitored by the rain gauge. Even when the rain gauge revealed no rainfall, it was possible that rainfall may have been less than 0.5 mmh^{-1}, due to the minimum resolution of the rain gauge. Usually, the DSD of rain is given in units of $m^{-3}cm^{-1}$ and that of sea spray in units of $m^{-2}s^{-1}cm^{-1}$. The DSDs of rainfall below the resolution of the rain gauge and sea spray were averaged at the various wind speeds (from 1 to 20 ms^{-1}) at 1-ms^{-1} intervals, in which the standard deviations were derived (**Figure 3.14** (a)). The DSDs of rain below the resolution of the rain gauge are shown in **Figure 3.14** (a). The three DSD lines were derived using **Eq**.(3.3) for a rainfall of 0.5 mmh^{-1} and μ values of -1, 0, and 1. All DSDs were within the ranges of the lines, suggesting that the DSDs were those of rainfall; however, it is difficult to define causality of why the number of droplets increased with horizontal wind speed. In contrast, if the droplets were considered as sea spray, the DSDs would be similar to those previously reported for sea spray (3), (57), (5) (**Figure 3.14** (b)). Our findings were higher than those obtained at low wind

speeds (up to 15 ms^{-1}), and presumably the DSDs from **Figure 3.14** (a), (b) are those of either rain or sea spray. Notably, the direct measurement of sea spray DSDs offers valuable data sets (**Figure 3.14**), as a direct approach has been rare in this field of study.

Figure3.15 is the drop size distribution, which is the same as **Figure**3.15 but with fitting curves. This drop size distribution was approximated by potential functions

$$\frac{dF}{dD} = aD^b, \tag{3.5}$$

The number of droplets increased with wind speed. Therefore, the parameters a and b can be approximated as a function of wind speed. Then, considering each parameter as a function of wind speed, the drop size distribution **Eq**.(3.5) fits the following explanation.

$$\frac{dF}{dD} = 10^{cU^d} D^{eU+f},$$

The scatter diagrams of each parameter and horizontal wind speeds are shown in **Fig**3.16. The values of c, d, e, and f in the approximated curves are listed in **Table 3.1**. Finally, a new drop size distribution as a function of wind speed was

Table 3.1: Parameters in drop size distribution: c, d, e, and f

c	d	e	f
1.85	0.28	-0.024	-0.91

obtained. **Fig**.3.17 shows the observed drop size distributions with approximated curves.

3.9 Summary

Understanding the sources and properties of small rain and large sea spray droplets, which coexist in the diameter class of less than 1 mm, enables far more precise measurement of open-ocean rainfall; in this study, droplets with a diameter of 0.072 to 1.000 mm were observed. We performed rain and sea spray

observations at a marine tower using a disdrometer, rain gauge, anemometer, and time-lapse camera. The shape parameter μ of the Ulbrich distribution (as estimated by the disdrometer) decreased even after rainfall decreased, indicating an increase in the number of droplets less than 1 mm in diameter. Time-lapse images of the sea surface throughout the rain event showed large amounts of sea spray presenting as streamlines over the sea surface; this led us to conclude that the disdrometer detects both rain and sea spray. The findings from our direct measurements may have important implications in the study of air-sea fluxes, as only limited observational data are available at present.

Additionally, the relationship between the number of small droplets with diameters less than 1 mm and the total rainfall intensity was investigated. As the wind grew stronger, the proportion of small droplets to total rainfall increased. This is because more sea spray was generated as the wind speed increased. In addition, DSDs were detected by the disdrometer during periods of rainfall less than 0.5 mmh^{-1}. Based on the results of previous studies, these DSDs could possibly be both rain and sea spray, though the higher DSDs corresponded to the increased wind speed. Our final analysis revealed the proportion of sea spray to total rainfall, suggesting the contribution of sea spray to the rainfall measurement. When the hourly wind speed varied from 16 to 20 ms^{-1}, the average sea spray proportions were 82.7%, 19.1%, and 5.3% of the total rainfalls of 2.1, 8.9, and 32.1 mmh^{-1}, respectively. The variations reflect differences due to the properties of sea spray.

This study investigated the effects of sea spray on open-ocean rainfall measurements through the calculation of DSDs and rainfall intensities based on direct observations. The study also explored the significance of spume droplet DSDs in estimating the air-sea fluxes of sensible and latent heat. In the context of rain DSDs, we proposed that the amount of sea spray generated could be another influential factor on possible variations of μ, in addition to the rainfall types and seasonality that were noted previously. Finally, the ratio of sea spray to the total rainfall was calculated to determine the contribution of sea spray, enabling us to improve the accuracy of rainfall estimates over the open-ocean. From this study, it is confirmed that rainfall over the open ocean was certainly affected by sea spray under strong wind conditions. The DSD of rain was also affected by sea

spray, as the parameter μ decreased monotonically with wind speed, even when rainfall intensity was constant. Considering that rain and sea spray co-exist in the open ocean, rainfall and sea spray DSDs should be addressed separately when calculating real rainfall intensities over the open ocean.

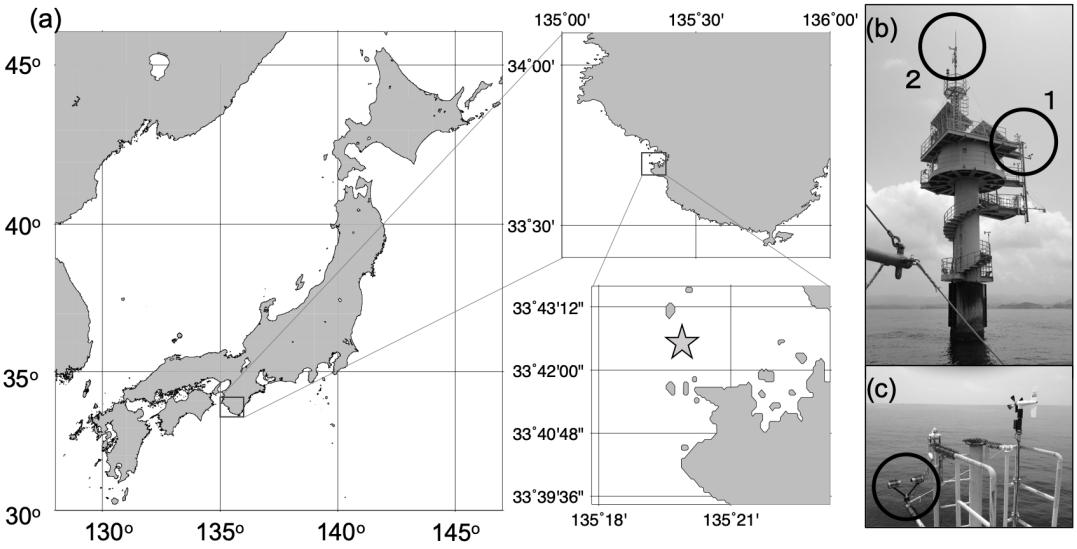

Figure 3.1: Location of the observation site, the observational tower and disdrometer. - (a) Map showing the location of the observation tower (marked with a star). The observation tower is located 1.8 km offshore from the mouth of the Tanabe Bay, Wakayama Prefecture. (b) Whole view of the Tanabe Island storm surge observation tower. Circle 1 shows the location of the disdrometer. Circle 2 shows the location of the propeller-type anemometer. (c) Installation of the disdrometer. The circle shows the disdrometer.

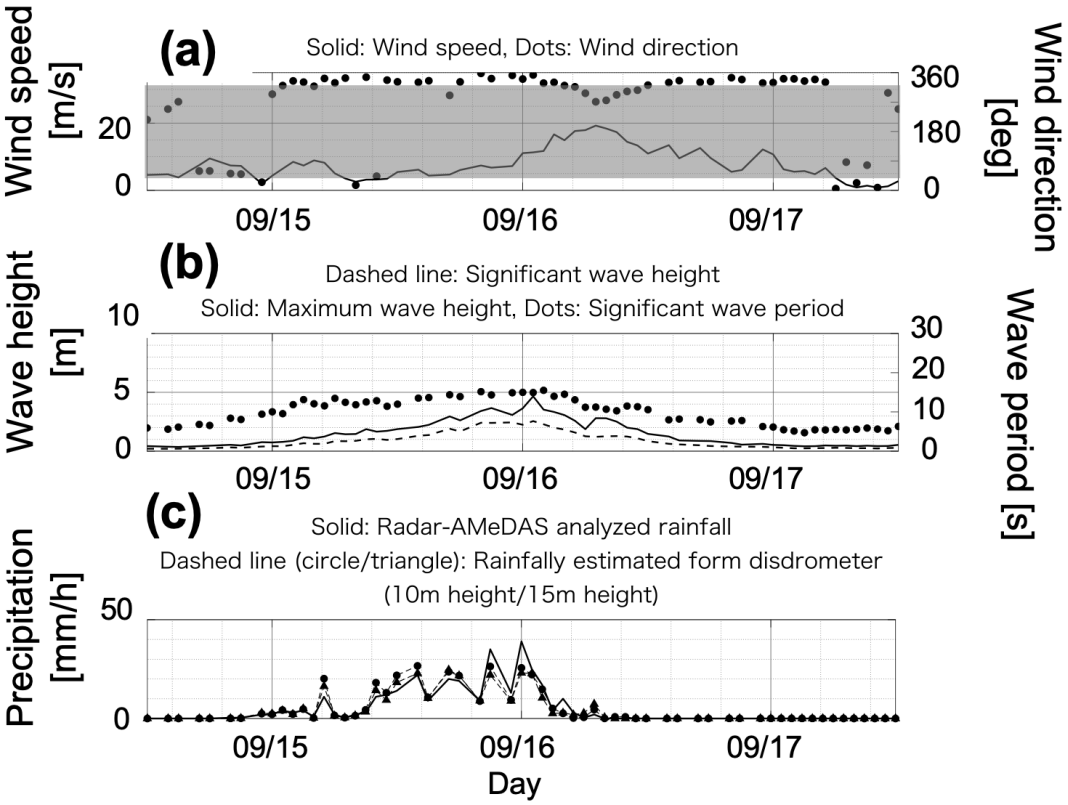

Figure 3.2: Time series of wind speed and direction, significant wave height, maximum wave height, significant period, rainfall intensity from analytical rainfall, and rainfall intensity from disdrometers at heights of 10 and 15 m at 12:00 on September 14, 2013, and 12:00 on September 17, 2013, during the passage of Typhoon No. 18 in 2014. - (a) The solid line indicates wind speed [ms^{-1}] and the dots indicate wind direction [$^{\circ}$]. The hatch indicates the wind direction of 45∼315 $^{\circ}$. (b) The solid line indicates the maximum wave height [m], the dashed line indicates the significant wave height [m], and the circle indicates the significant period [s]. (c) The solid line shows the analytical rainfall and the round and triangular lines show the rainfall intensity [mmh^{-1}] obtained from the disdrometer at 10 and 15 m height, respectively.

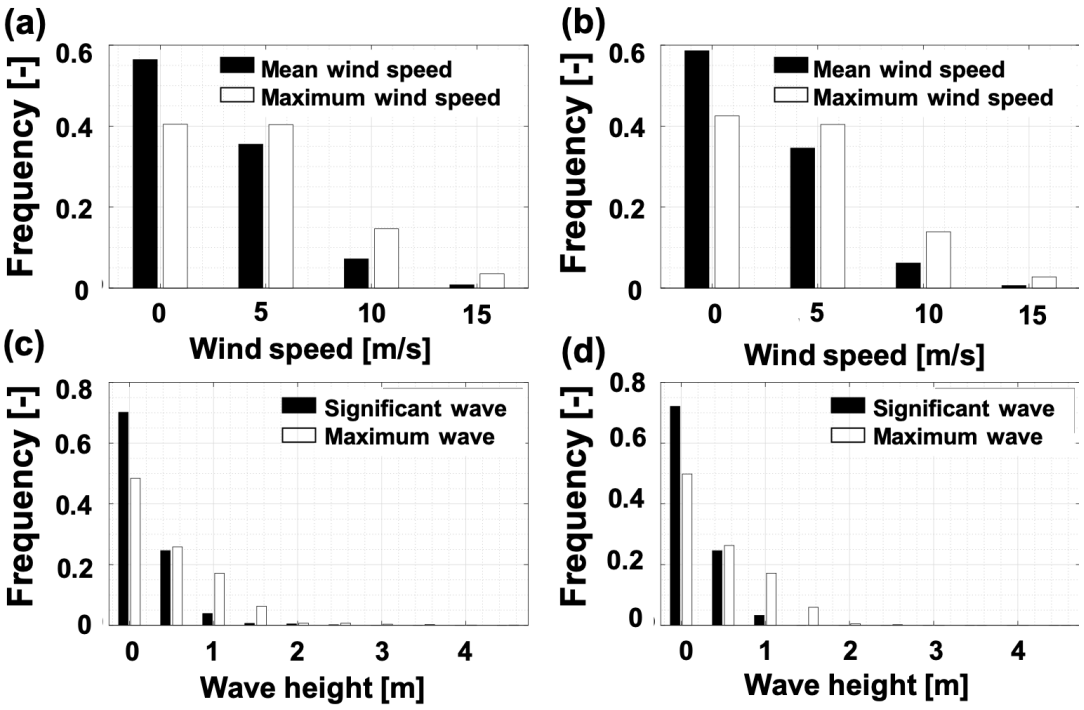

Figure 3.3: Relative frequency of wind speed and wave height. - (a) Histogram of the maximum and average wind speed, (b) histogram of the maximum and average wind speed observed in the absence of rainfall, (c) histogram of the maximum and significant wave height, and (d) histogram of the maximum and significant wave height observed in the absence of rainfall.

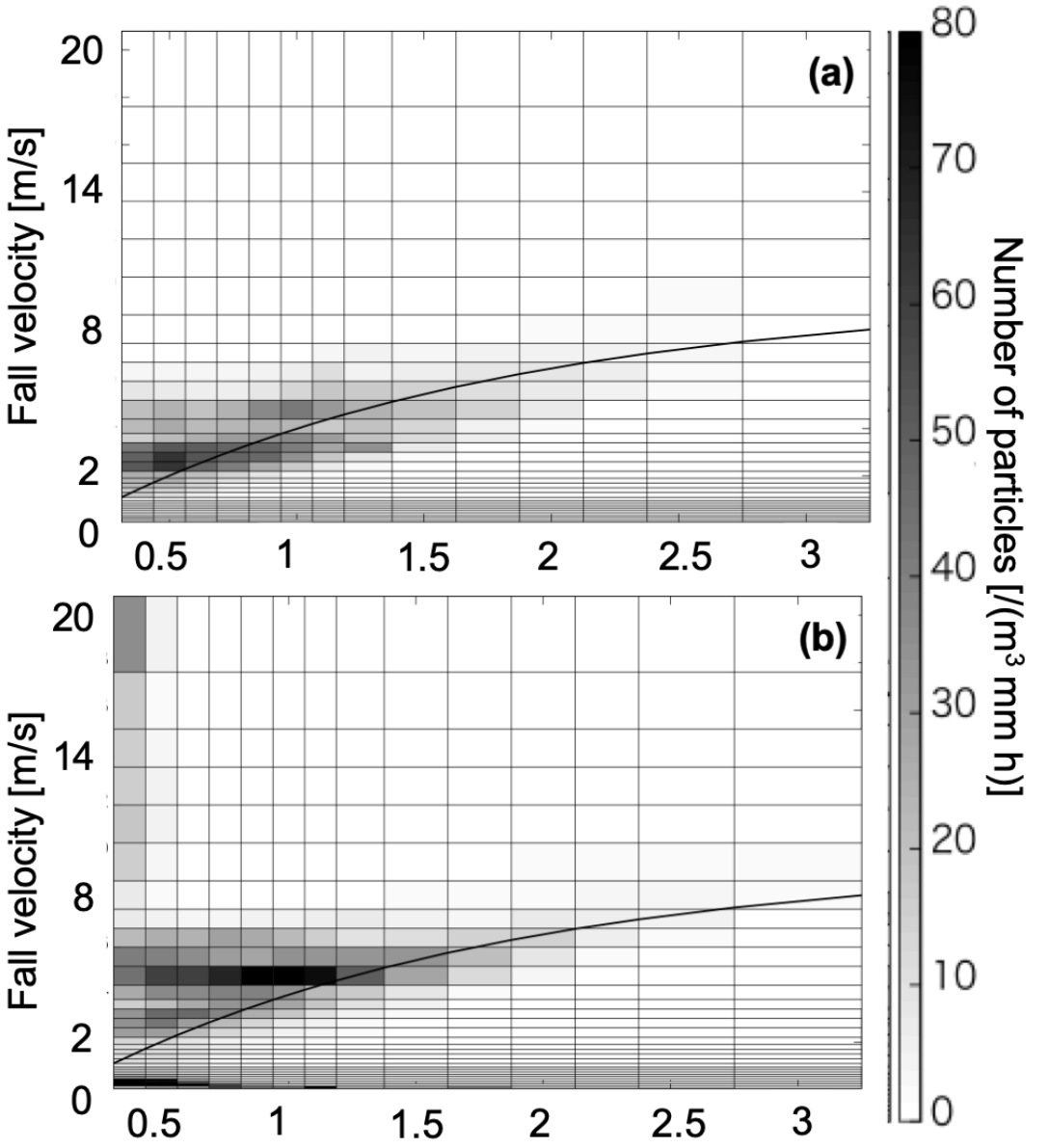

Figure 3.4: Number of particles averaged over 1 h for each drop size and fall velocity. - The data are the results of observations from a 10 m high disdrometer. (a) Observation result when the wind speed is 5∼10 ms^{-1} and the rainfall intensity estimated from the disdrometer is 3∼6 mmh^{-1}. (b) Observed result when the wind speed is 10∼15 ms^{-1} and the rainfall intensity is 3∼6 mmh^{-1}. The gray scale indicates the number of particles.

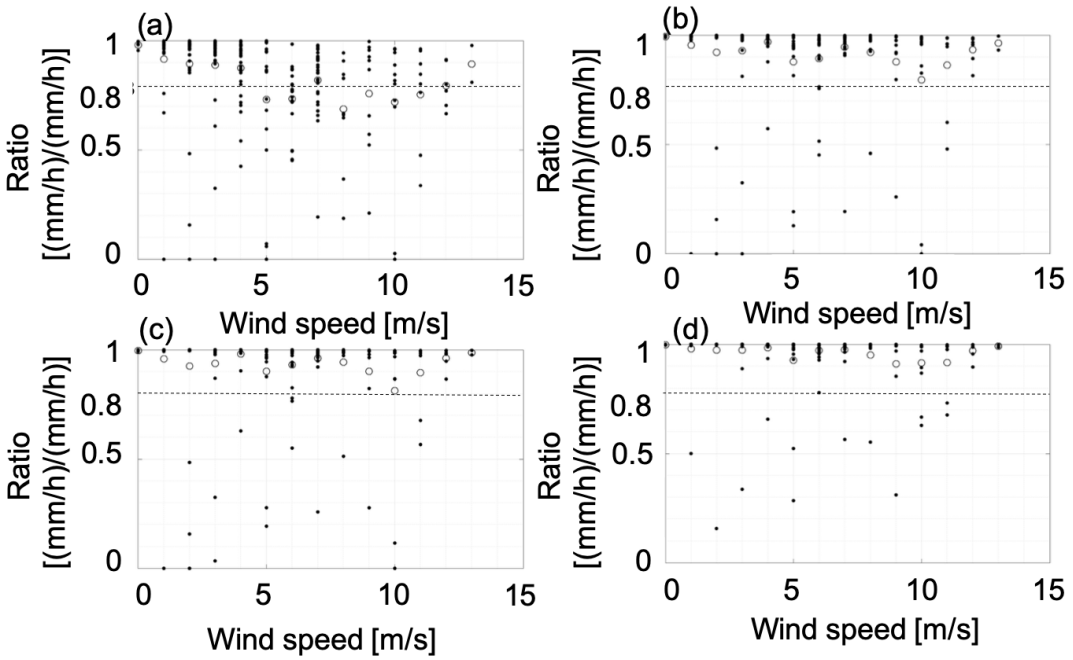

Figure 3.5: Relationship between the wind speed and the percentage of rainfall intensity calculated from the particles in accordance with the relationship between the particle size and the terminal fall velocity to the rainfall intensity calculated from the total volume of particles detected by the two installed disdrometers. - (a) Percentage of particles with a terminal velocity of ±20 % of the total volume. (b), (c), and (d) show the percentage of particles with a terminal velocity of ±40 %, ±60 %, and ±80 %, respectively. The white circles indicate the mean values, and the dashed line indicates 80 %.

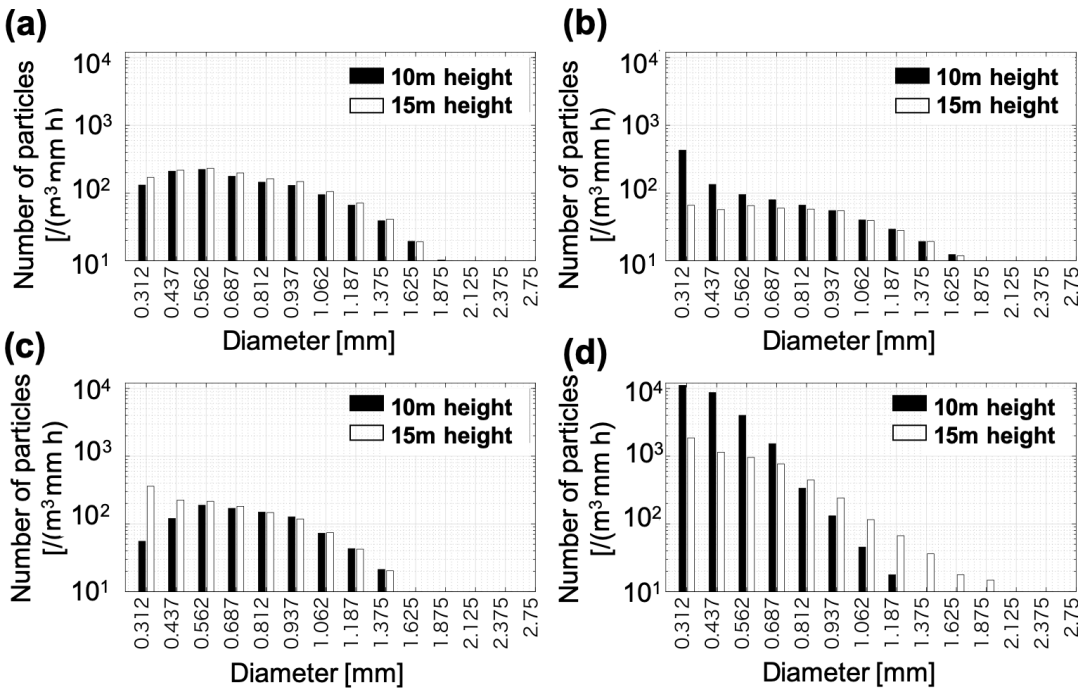

Figure 3.6: Hourly averaged drop size distributions detected at 10 and 15 m heights. - (a)∼(d) are the results when the wind speed was 0∼5, 5∼10, 10∼15, and 15∼20 ms^{-1}.

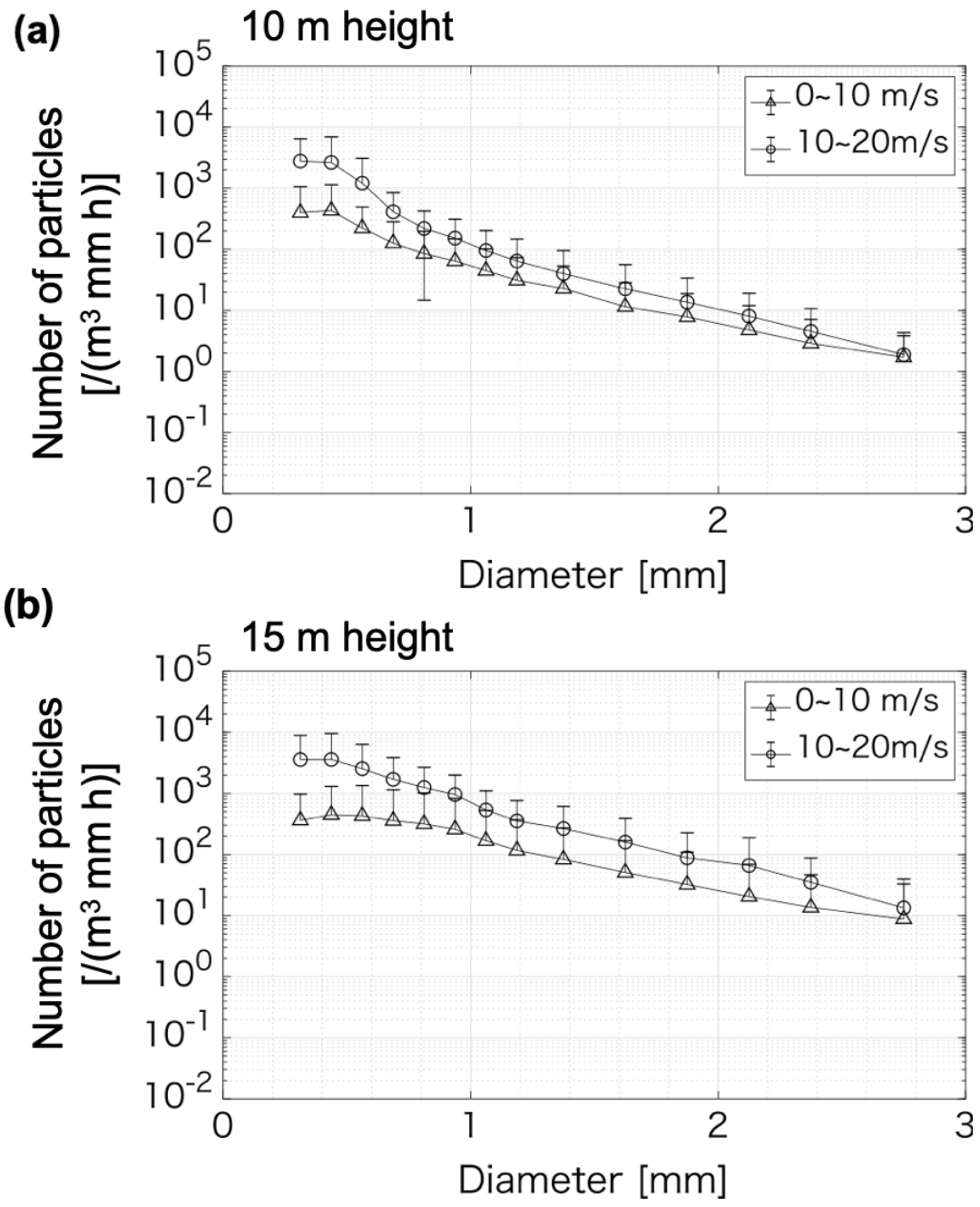

Figure 3.7: Drop size distributions at wind speeds of 0∼10 ms^{-1} **and 10∼20** ms^{-1} **obtained from observations.** - (a) and (b) are the drop size distributions obtained from the observations at 10 and 15 m height, respectively. The length of the bars represents standard deviation. The slope of the drop size distribution is used as a threshold to classify the data.

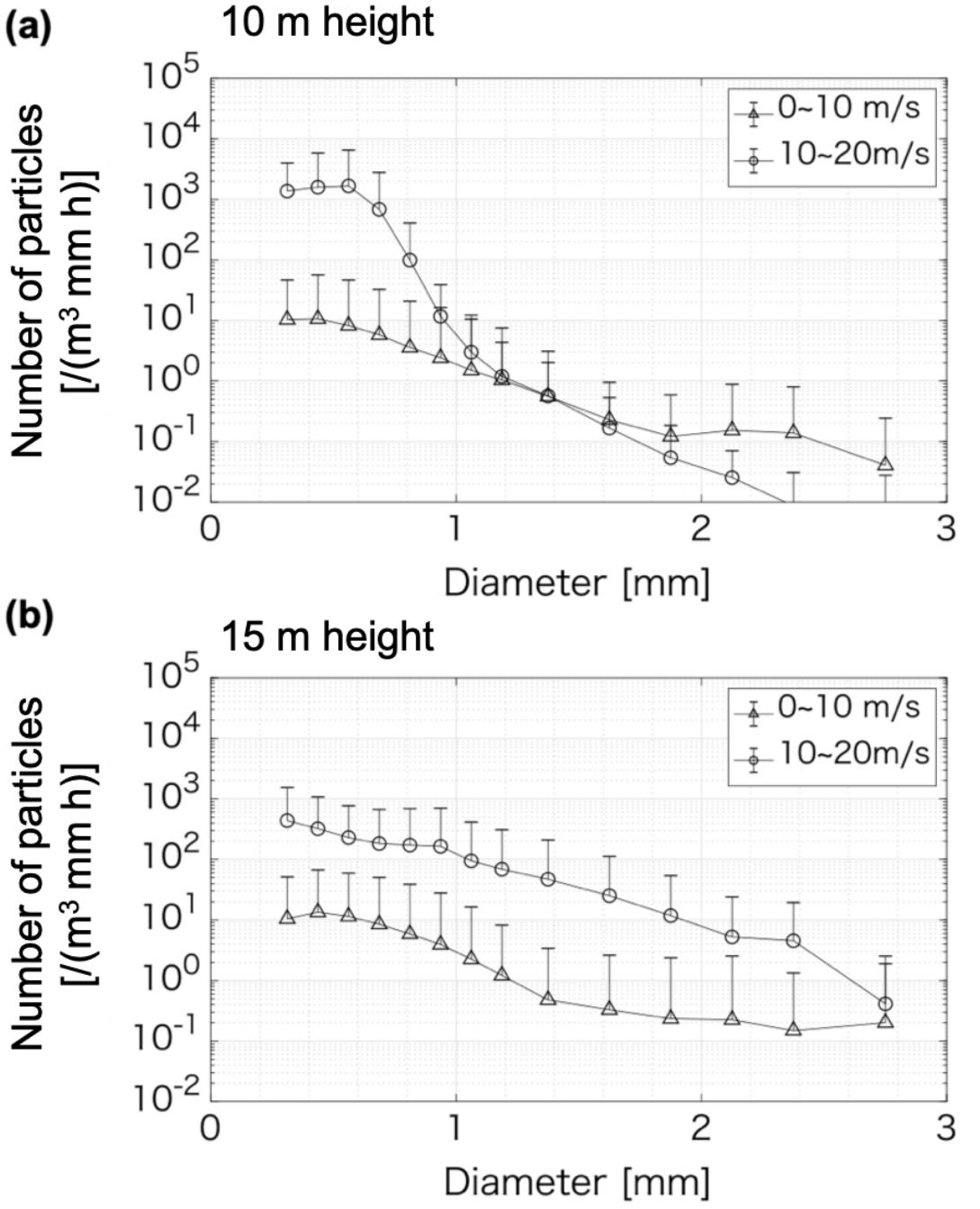

Figure 3.8: Drop size distributions obtained from observations at wind speeds of 0∼10 ms^{-1} and 10∼20 ms^{-1}. - (a) and (b) are the same as **Figure 3.7**.

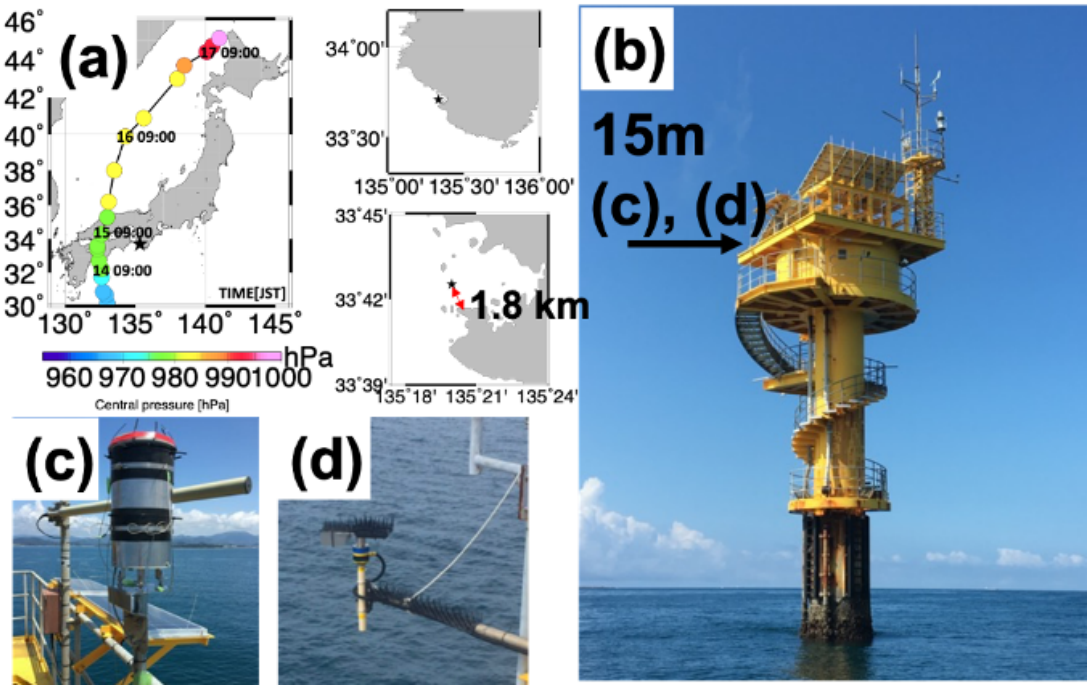

Figure 3.9: Map of the study area. - (a) Observation site is indicated by a black star. Colored circles indicate the central pressure and track of Typhoon Krosa over time (JST). (b) Observational tower; the arrow indicates the height of the observation deck (15 m) and the positions of the instruments, including (c) the tipping bucket and (d) snow particle counter (SPC).

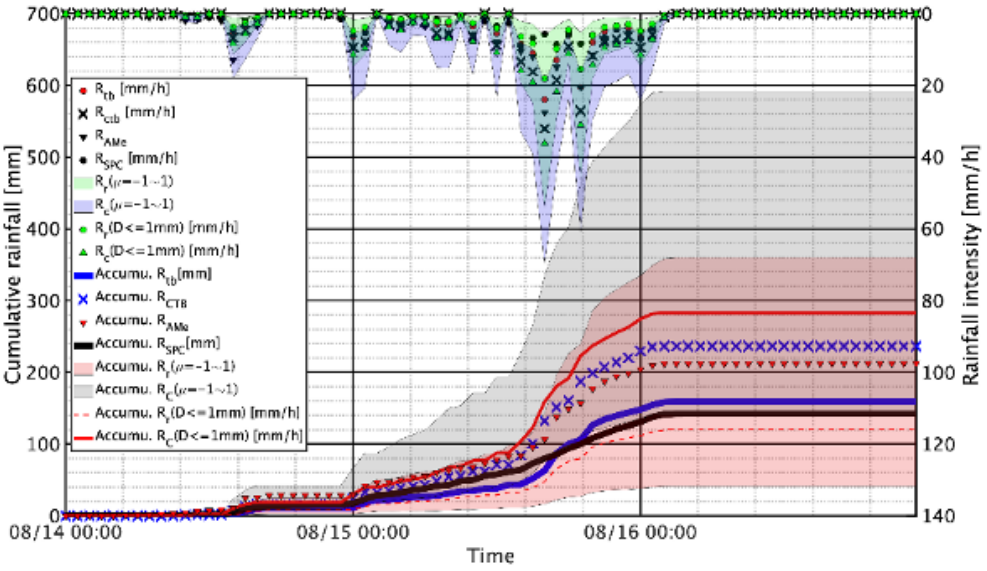

Figure 3.10: Time series of rainfall intensity and cumulative rainfall from August 14 to 16, 2019 (JST). - The rainfall intensity (right axis) of R_{tb} and R_{ctb} is shown in the red circles and black crosses, respectively. Rainfall intensity detected at the automated meteorological data acquisition system (AMeDAS) station (R_{AMe}) is indicated in black triangles, and the intensity calculated from the SPC data (R_{SPC}) is in black circles. The areas where the estimated results (($Rr(D<1)$ and $Rc(D<1)$) are described in Section 2.4 are highlighted in blue and green, respectively; they depend on the shape parameter (μ) values ranging from -1 to 1. The green circles and triangles represent $(D<1)$ $Rr(D<1)$ and $Rc(D<1)$ $(D<1)$ with $\mu = 0$. The left vertical axis shows the cumulative rainfall for each component (R_{tb}, R_{ctb}, R_{SPC},$(D<1)$, $Rr(D<1)$, and $Rc(D<1)$ $(D<1)$) from 00:00 August 14 (JST). Cumulative rainfall of R_{tb} and R_{ctb} are shown with the blue solid line and blue crosses, respectively, and that of R_{SPC} is in the black line. Cumulative rainfall of $Rr(D<1)$ $(D<1)$ and $Rc(D<1)$ $(D<1)$ with μ = 0 are expressed in red solid and dashed lines, respectively. The red area indicates the difference between the shape parameter μ = -1 and $\mu = 1$ where AMeDAS data points are plotted as red triangles.

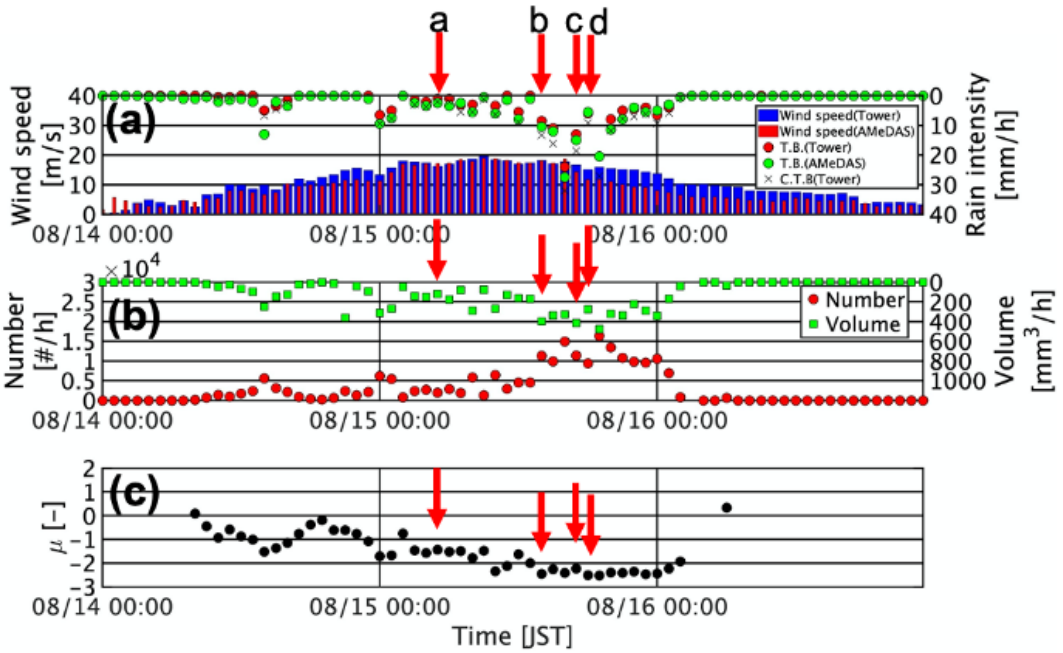

Figure 3.11: Time series of hourly wind speed and rainfall intensity (R_{tb}, R_{ctb}, and R_{AMe}), as well as the total number and volume of droplets and drop size distribution (DSD) shape parameter μ. - (a) Wind speeds at the tower and automated meteorological data acquisition system (AMeDAS) station are expressed with blue and red bars, respectively. R_{tb} and R_{ctb} are shown in green dots and black crosses, respectively, and R_{AMe} is in red dots. (b) Red circles indicate the total number of droplets detected by the SPC. Green squares indicate the total volume of particles. (c) DSD shape parameter μ is shown. Arrows in (a–d) indicate the time points photographed in **Figure 3.12**.

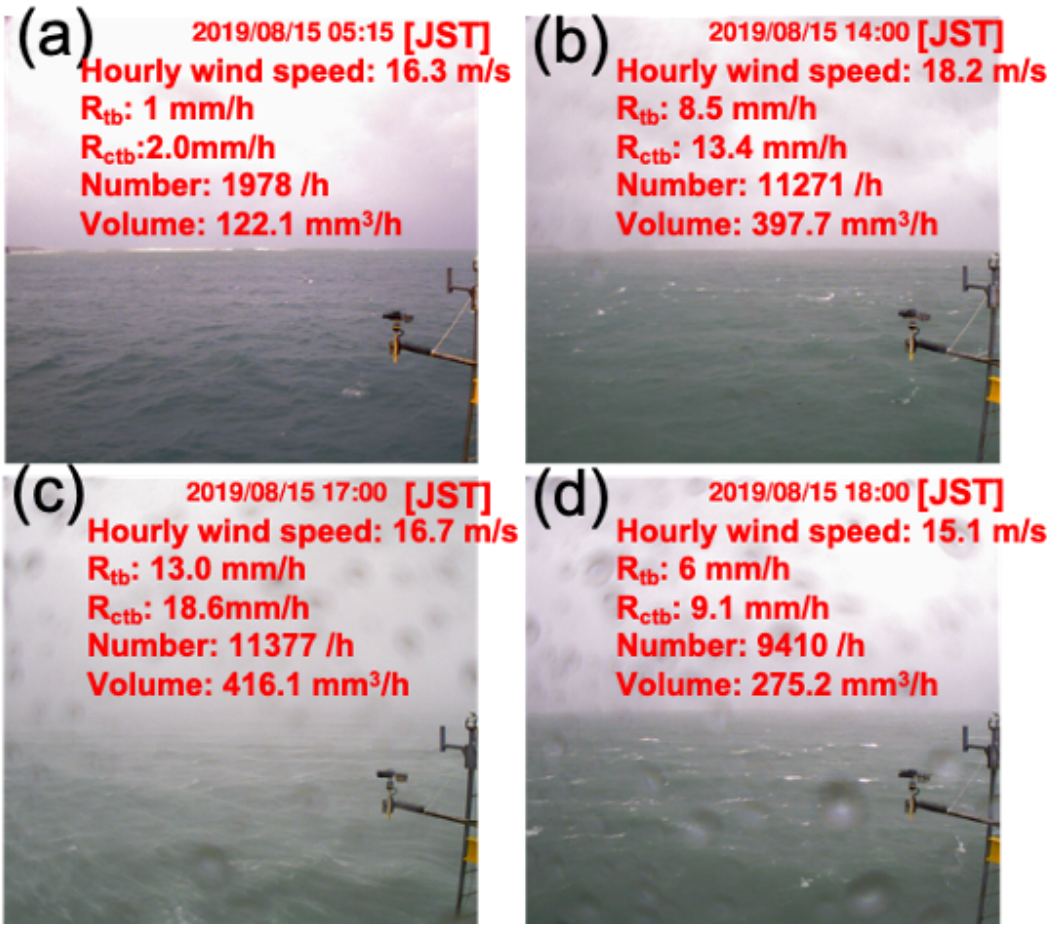

Figure 3.12: a-d Photographs of sea surface conditions. - (a)-(d) are equivalent to the time points indicated by the arrows in **Figure 3.11** a-d.

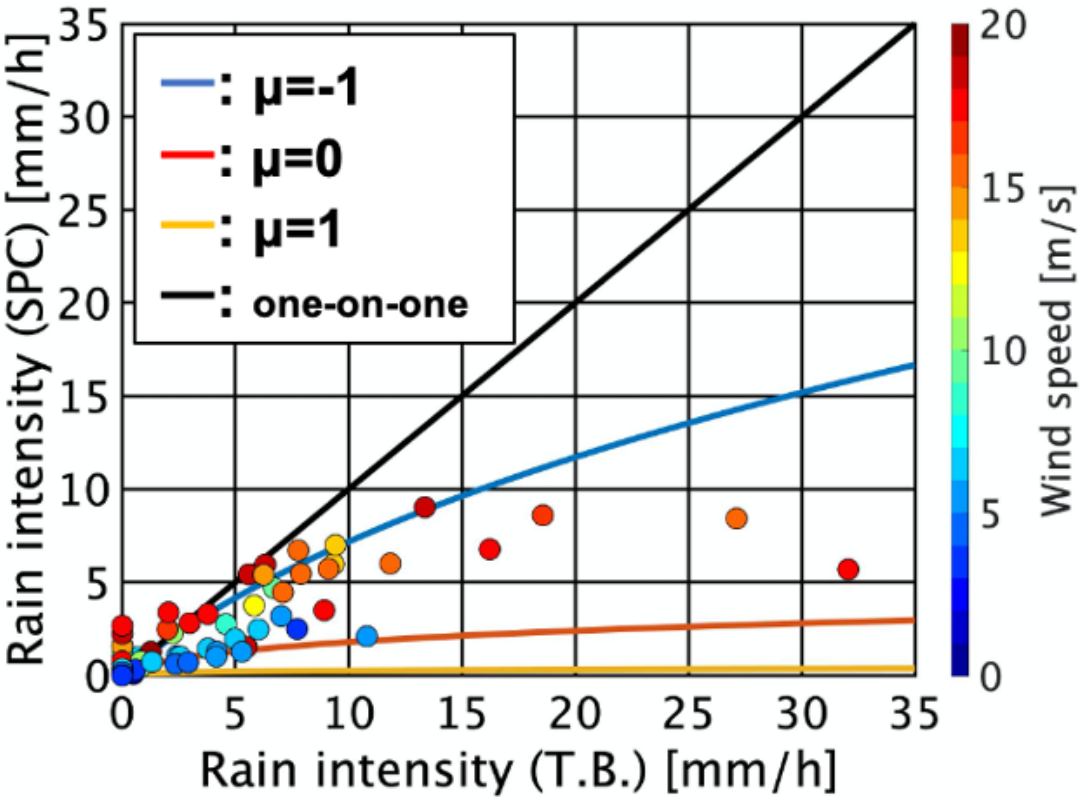

Figure 3.13: Relationship between rainfall intensity (R_{ctb}) and the intensity derived from SPC data (R_{SPC}). - Hourly wind speed is indicated in bar colors. Lines indicate the relationship between the rainfall intensity of drops with diameters less than 1 mm and the total rainfall intensity based on Ulbrich distributions for different values of μ, where light blue = -1, red = 0, and orange = 1. The black line indicates a one-on-one line.

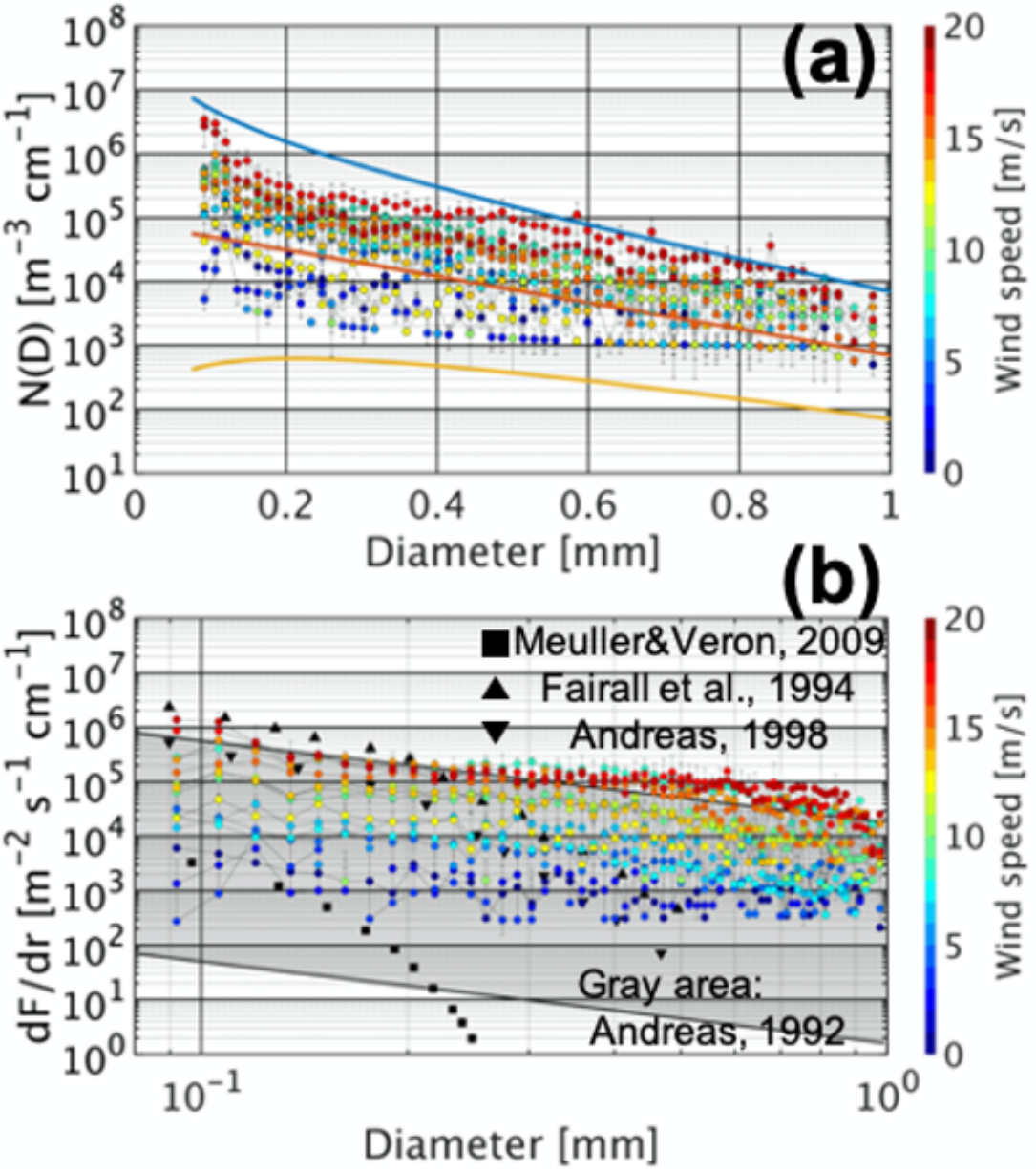

Figure 3.14: Drop size distributions (DSDs) that may include droplets derived from both rainfall and sea spray. - Each DSD is averaged for each hourly wind speed. The black bars show standard deviation (σ. Bar colors indicate hourly wind speed. (a) Ulbrich distribution for different values of μ, where light blue = -1, red = 0, and orange = 1. (b) DSDs of sea spray at hourly wind speeds ranging from 1 to 20 ms^{-1} in intervals of 1 ms^{-1}. The DSDs calculated in previous studies are also shown.

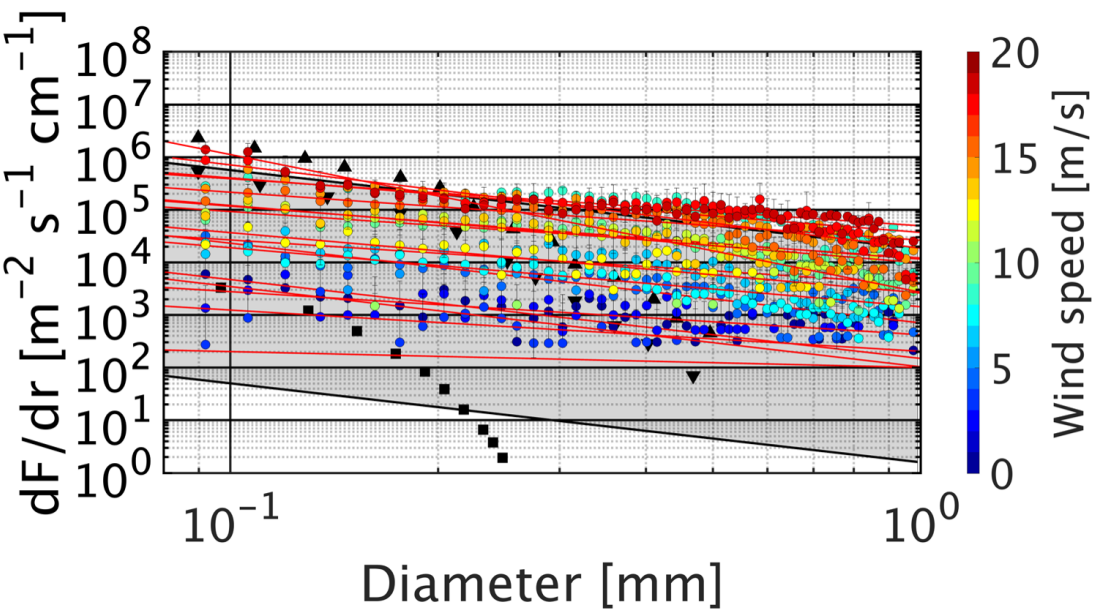

Figure 3.15: Drop size distribution of sea spray with fitting curves.
- Same as **Fig**.3.14(**b**) but with fitting curves with red lines.

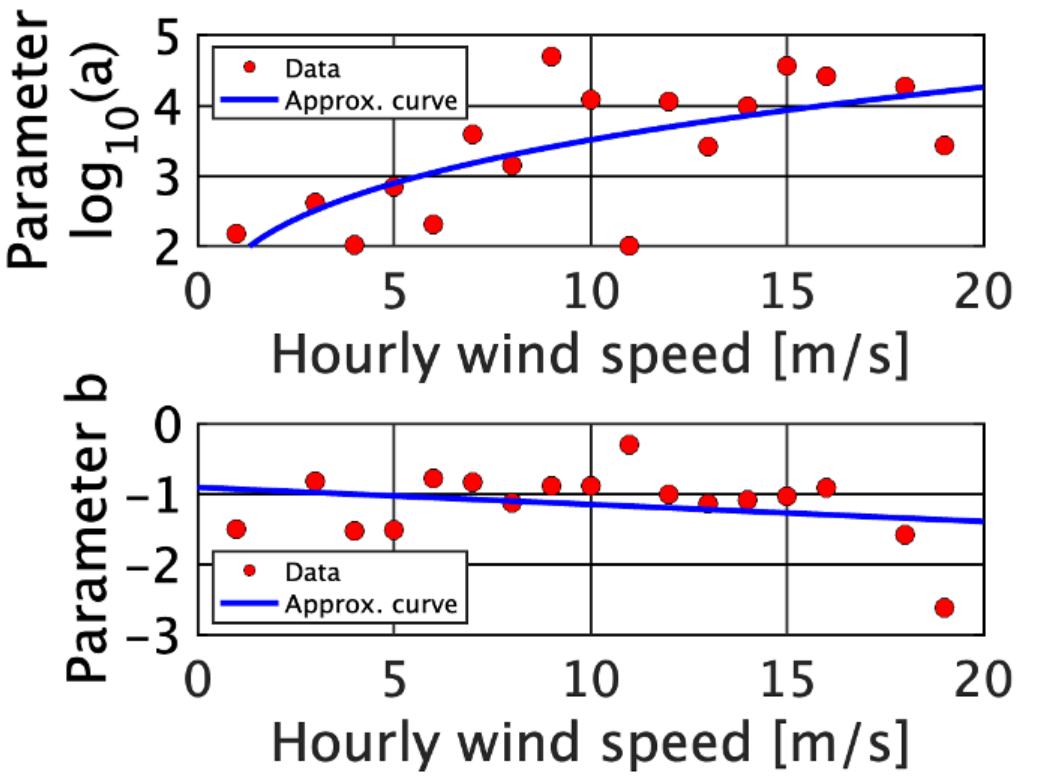

Figure 3.16: Scatter diagram of each parameter and hourly wind speeds. - Blue lines are fitting curves.

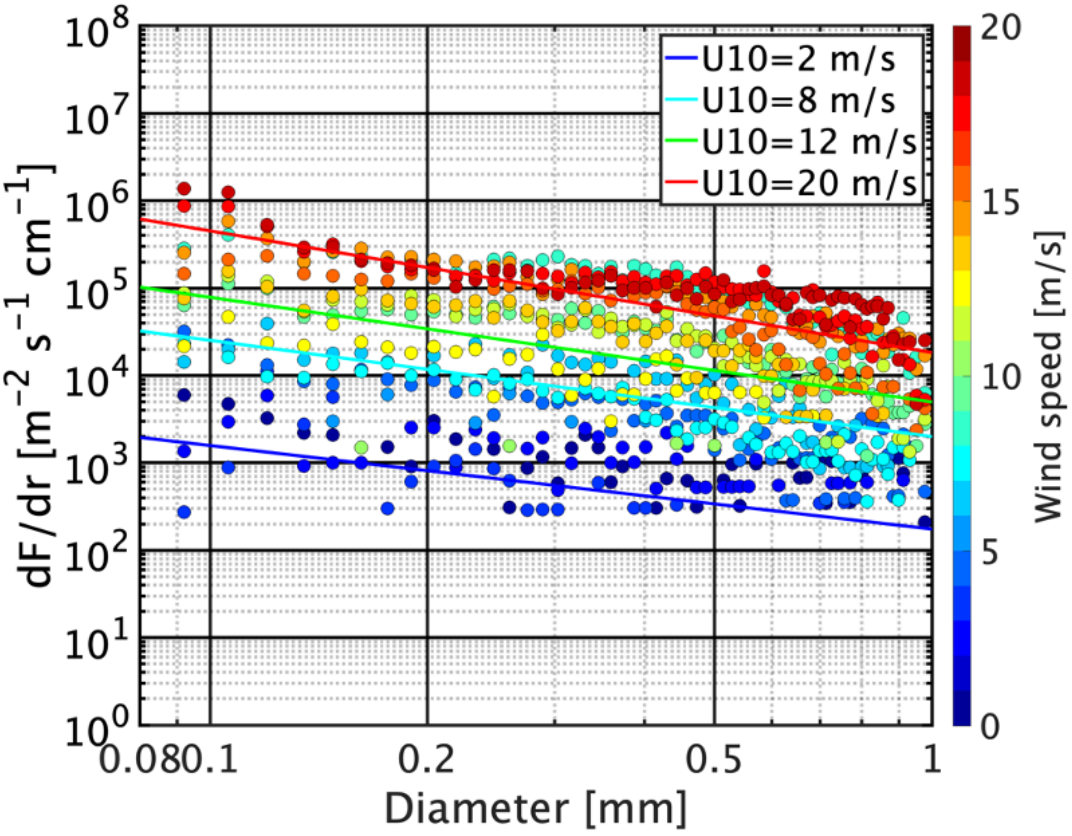

Figure 3.17: Drop size distribution of sea spray with fitting curves.
- Color of dot and fitting curves shows horizontal wind speed.

4

Estimation method of radar gain and sea clutter

4.1 introduction

Drop size distribution of sea spray is generally observed at a single point using buoy, optical disdrometer, or other instruments. In this study the disdrometer observations were conducted. To obtain the vertical distribution of concentration and dynamic structure of sea spray under winds and rain conditions, ship radar observation was conducted. This chapter introduces the detail of observation and a method to estimate radar gain which is the parameters of radar instruments in order to convert the received power, which is the result of radar observation, into the normalized backscattering radar cross section. The radar used in this study was a relatively inexpensive ship radar, which was rotated in the vertical direction to observe a height of about 2.5 km from the sea surface. This method is an innovative method proposed by Fujiyoshi et al. (2018)(31). However, since the radar was designed to detect surrounding ships and wave height, the algorithm to estimate the concentration of sea spray need to be proposed. Furthermore, because data size from radar observation is too huge to store, the radar image which has gradation from 0 to 255 is stored. Because of that, the color image should be converted into physical quantity. Therefore, in this chapter, the conversion

method from radar image into normalized radar backscattering cross section is proposed.

In addition, the height of sea clutter from the sea surface, which is a problem in radar observations, is taken into account in the radar width to lower the observable range as much as possible. Near-surface observations include reflections from the ground and sea surface. The received power from sources except the observation target is called clutter, for example, ground clutter and sea clutter. XRAIN (X-MP radar), a radar network system provided by the Ministry of Land, Infrastructure, Transport and Tourism (MLIT), is designed to observe rainfall and snowfall. The X-MP radar has a spatial resolution of 250 m and a temporal resolution of 1 minute. In this radar network, it is known that ground clutter from mountainous areas and sea clutter can be observed in winter because the radar elevation angle is small.

4.2 Ship radar observation

In this study, a ship radar was installed in the coastal area of Tanabe Bay, Wakayama Prefecture, to observe rainfall and sea spray during the summer in 2018. The location, typhoon path, typhoon center pressure, and installation status of the ship radar are shown in **Figure** 4.1. The observation location was about 2.7 km from Tanabe Bay, Shirahama, Wakayama Prefecture, in the ocean direction, and 2.6 km above the sea surface. The observation have been conducted from 2 August to 20 October, 2018 when three typhoons (CIMARON, JEBI, TRAMI) have been passed from the site. **Figure** 4.1 (a-1, 2, 3) shows the typhoon path, central pressure, the Tanabe-Nakashima storm surge observation tower (hereafter referred to as the tower) at the Disaster Prevention Research Institute (DPRI), Kyoto University, and the location of the radar. **Figure** 4.1 (a-1) shows the typhoon path and central pressure. **Figure** 4.1 (a-2) shows an enlarged image of the area enclosed by the red frame. **Figure** 4.1 (a-2) shows the Kii Peninsula, and **Figure** 4.1 (a-3) is an enlargement of the red frame in the same figure. In **Figure** 4.1 (a-3), the star indicates the observation tower

and the circle indicates the location of the radar. The radar is launched in the direction of the observation tower. **Figure 4.1** (b) shows the installation of the ship radar. The RHI observation was performed by rotating the radar in the vertical direction. The ship radar used in this study is conventionally used for ships. In this study, the radar was used to observe rainfall and sea spray over a horizontal distance of 2.7 km and a vertical distance of 2.5 km.

4.2.1 Data

4.2.1.1 Meteorological data

The rainfall data from the Nanki-Shirahama AMeDAS (Automated meteorological data acquisition system), which is located about 4 km away from the observation site, and the rainfall data from the X-MP radar are used for comparison. The wind speed and direction data were obtained from the 10-minute mean values at the AMeDAS site and from the 10-minute mean values of the propeller-type anemometer installed in the observation tower. For significant wave height, the 10-minute mean value of the ultrasonic wave height meter at the observation tower was used. The maximum horizontal wind speed at 23 m height was 39.5 ms^{-1} and maximum wave height is 11.2 m within this observation periods.

4.2.1.2 Ship radar data

The radar used in this observation is generally mounted on a top of ship to detect surrounding other ships. Radar wave length is 3 cm, frequency is 9410 MHz, and transmitted power is 25kW. Horizontal beam width is 1.2 degree, vertical width is 22 degree. Due to the usage, this radar just observe color image which has gradation from 0 to 255. This should be converted into normalized radar cross section which is kind of radar reflectivity.

4.2.1.3 Observation results

Figure 4.2 shows an example of the results obtained from the ship radar observations during the passage of Typhoon No. 20 from 11:00:01 to 23 seconds on August 23, 2018. The hourly mean wind speed at the same time was 11.2

ms^{-1} with rainfall intensity of 0.5 mmh^{-1}. The wind direction was the same as the radar injection direction. The position of the radar is at the lower left of the image, the horizontal distance is 2.7 km and the vertical distance is 2.5 km. The strong echo from the sea surface is a sea clutter. These confirm that rainfall falls diagonally due to wind. The radial lines in images (a), (e) and (f) are noise because another radar with horizontal rotation is settled at the same observational site to detect wave height.

Figure 4.3 shows what radar detect in this observation series. Radar detect rain, sea spray, sea foam and sea surface in this observation. Each scattering phenomenon are shown in the figure, respectively. Scattering by rain and sea spray is represented by Rayleigh and Mie theory, respectively. The Rayleigh scattering can be described by Mie theory (detailed explanation is in Appendix). The foam is also represented by Mie theory, assuming that foam is recognized as air particle with thin water shell(44). Scattering by sea surface is represented by surface scattering called as Bragg scattering. Bragg scattering occurs when scatterer is much larger than wavelength you use. In this observation, scattered waves by sea surface and foam are excluded by estimate of the height which sea clutter reaches.

Figure 4.4 shows time series of observed variable: rainfall intensity, wind speed and direction, and wave height from 06:00 (JST) to 18:00 on 4th September, 2018. Typhoon 21 (JEBI) passed the site during this period. Rainfall intensity, wind speed and wave height increased with typhoon approach and the maximum wind speed 39.5 ms^{-1} was obtained. This event caused the recored maximum wind speed at the AMeDAS station from 2006 to 2020. The other events, typhoon TRAMI and CIMARON, caused the second and third record maximum wind speed in the same AMeDAS station.

4.3 Methodology of estimate for radar backscattering cross section

Radar image has gradation from 0 to 255, although the purpose of this observation is to estimate concentration of sea spray. To achieve the main purpose,

radar image should be converted into radar backscattering cross section which is an indicator of reflection. In next chapter, the estimation method of concentration of sea spray is proposed.

In this section, the conversion method from radar image into normalized radar backscattering cross section is proposed.
The method consists of following 5 steps.

1. Collect radar images for time periods when the wind direction and radar observation coincide.

2. Exclude noise due to interactions between two radars and apply spatial average (arithmetic).

3. Estimate electric power from color gradients in the gray scale images by a reference.

4. Apply the bias correction to represent distance between radar and target grid cells.

5. Calibrate the radar electric power (ship radar) using meteorological radar.

The first step is to ensure that there is no difference between the direction in which rain and sea spray move and the behavior that appears in the image. Here, it is hypothesized that horizontal wind and horizontal advection of rain and sea spray match together. Radar is not able to detect the movement which does not follow the direction of radar emission.

The second step is to reduce the noise. As mentioned before, there are noises in the radar image because two ship radars are installed in this observation. The methodology to mitigate the noise in the image is shown in next section.

4.3.1 Noise reduction

The method to remove noise (shown in **Figure 4.2**) is introduced in this chapter. In another figure to show the data, received power is converted into reflectivity shown in **Figure 4.5** (Conversion method is in Chapter 5). The origin of x-y coordinate shows ship radar. The strong signal at 1.8 km of x-coordinate is from the tower. At 0 m height, strong signals horizontally distributed are sea clutters. Under a calm sea, rainfall intensity was 0 mmh^{-1} (**Figure 4.5** a). There was no signal except sea clutter. In **Figure 4.5** b-c, although rainfall was

0 mmh^{-1} by X-MP, signals existed at the altitude less than 1 km. In **Figure 4.5** d rainfall intensity was 13.0 mmh^{-1}. Strong signals were observed in all area. In summary, it is confirmed that ship radar observed rainfall and also sea spray.

The raw value ranges from 0 to 255; the minimum value shows black and the maximum value shows white. **Figure 4.6** (a-1) shows raw data and **Figure 4.6** (a-2) shows histogram of the gradation from 0 to 255 in each grid in the red rectangular. **Figure 4.6** (b-1) shows the same raw data as **Figure 4.6** but different rectangular. **Figure 4.6** (b-2) shows histogram inside of red rectangular in **Figure 4.6** (b-1). The value at both ends are relatively decreased, because the surface area contains strong reflection from sea surface and the signal from the tower. However, there still exists 255 due to the radial noise. Focusing on the data around the noise, the raw data and the maximum data are shown in **Figure 4.7**. The (a-1) shows raw data and (a-2) show histogram of that. The right column shows data above (b-1) 255, (b-2) 230, and (b-3) 200. The radial noise has more than approximately 200 value. To eliminate noise grid, interpolation is applied for raw data. The methodology is that the value of the grid with data above the threshold is replaced by the arithmetic mean of the surrounding 9 grids. The example result is shown in **Figure 4.8**. The **Figure 4.8** (a-1, 2) show raw data, **Figure 4.8** (b-1, 2) shows the data above the threshold of 200 and the right column shows the interpolated data. From (b-1), the data above the threshold is distributed near radar site and exist in a discrete state as noise, and the number of pixels is 32224 (3%) against the total of 1408000. From **Figure 4.8** (c-1), the strong signals are eliminated using the threshold of 200. Comparing the histogram of (a-2) and (c-2), the shape below 200 is similar to each other. The final figure in this section is shown in **Figure 4.9**, which is the relationship the ratio of eliminated data against the total area with various threshold from 190 to 255. The rate decreases to less than 2.5 % when threshold is 200. From these analysis, the threshold is determined as 200.

4.3.2 Estimate electric power and bias correction to represent distance

In this section, the third and fourth method are introduced. Radar image has 0 to 255 gradations. The gradation can be converted into electric power by a reference. That is defined as following equation.

$$P_r(x, y) = -100 + 0.352 \times Image(x, y),$$

Here, $P_r(x, y)$ shows electric power [dBm] in grid of x-th row and y-th column and $Image(x, y)$ shows gradation (0 255) in x-th row and y-th column. The value, -100 is the minimum limitation of detection. This equation is applied in this observation data.

Considering the radar attenuation, the equation needs to be modified. The mechanism of attenuation is based on the concept of electric flux which is the measure of the electric field through a given surface. Since electro-magnetic wave propagates radially, the flux decreases as the distance between the radar and objective increases. The concept of modification for this attenuation is electric power should be the same at each distance. That is why the electric power should be considered the distance. The equation to modify the difference due to the distance is shown in below.

$$P_r(x, y) = -100 + 0.352 \times Image(x, y) + 40 \times log_{10}(r(x, y)),$$

Here, $r(x, y)$ shows distance between radar and the grid on x-th row and y-th column. The black-and-white radar image is converted into received power [dBm] by this equation to reduce the attenuation effect based on the distance.

4.4 Quantification method of radar observed data

The last step is to estimate normalized radar backscattering cross section introduced in this section. Radar observation is based on the scattering theory of electromagnetic waves. When an electromagnetic wave irradiates an object, the free electrons in the object vibrate to produce a new electromagnetic wave.

This phenomenon is called scattering, and the object that emits the electromagnetic wave is called a scattering medium. The characteristics of the radar, the scatterer, and the power received by the radar are expressed by the Friis(30) transfer formula, which is generally called the radar equation and uses the following equation(41).

$$P_r = \frac{P_t G_t^2 \lambda^2}{(4\pi)^3 R^4} \sigma, \tag{4.1}$$

where, P_r is received power [W], P_t is emitted power [W], G_t radar gain[-], λ is wave length [m], R is distance between radar and scattering medium [m], σ is radar backscattering coefficient [m^2] (hereafter, RCS). The radar backscattering cross section depends on the material and shape of the scattering medium and is an important parameter in radar observations. **Eq**.(4.1) is a radar equation for mono-static radar whose transmitted antenna is the same as received antenna.

The radar gain represents the directivity of the radar and is the ratio of the power density of electromagnetic waves radiated in one direction against the power density when radiated uniformly in all directions with the same power. The radar gain is required for quantitative evaluate of received power. The radar gain of the ship radar is estimated using the observations of the X-MP radar, whose gain is known. The X-MP radar captures the same observation target as ship radar.

Here, when the received power of an antenna in an electric field with a certain power density P_1[Wm^{-2}] is P_2 [W], the effective area is P_2/P_1 [m^2]. In other words, it represents the range of power that the antenna can receive. From **Eq.** (4.1), $P_t G_t / 4\pi R^2$ represents the power per unit area [Wm^{-2}] at the distance R from the radar to the scattering medium. Multiplying it by radar backscattering cross section, which represents the power radiated per effective area relative to the incident power, gives the power radiated by the scatterer [W]. Furthermore, to obtain the power density at the distance R, divided by $4\pi R^2$ and multiplied by $\lambda^2 G_t / 4\pi$, which is the effective area of the radar, to obtain the power received by the radar P_r. RCS is a value that depends on the radar irradiated area. Therefore, normalized radar backscattering cross section is used to standardize it. Normalized radar backscattering cross section is expressed by the following

equation(41).

$$\sigma_0 = \left\langle \frac{\sigma_j}{\delta A_j}, \right\rangle \tag{4.2}$$

where, δA_j is area of j-th scattering medium. The parentheses in the equation represent the ensemble average, which is the average of all point scattering medium contained in the unit volume. Thus, in the process of radar observation, Normalized radar backscattering cross section is the only parameter that depends on the scatterers, and by estimating the Normalized radar backscattering cross section of an object, radar can expand the observability. To estimate the normalized radar backscattering cross section from the observation results, the following equation is used from **Eq.** (4.1) (4.2).

$$\sigma_0 = \left(\frac{(4\pi)^3 R^4}{G_t^2 \lambda^2} \frac{P_t}{P_r} \right) / A. \tag{4.3}$$

where, A is total irradiated area from radar at the distance of R. In order to estimate the gain of the ship radar, the gain was estimated by comparing it with the normalized radar backscattering cross section for rainfall estimated from the observations of the X-MP radar, which has a known radar gain. The rainfall intensity obtained from the X-MP radar is the arithmetic mean of the data of the area of ship radar observation. In this study, ship radar data is compared with X-MP radar data in Katsuragi station. Parameters of Katsuragi station have been already set(84). To compare the X-MP radar with ship radar, the data detecting the area, altitude of 1 km to 2.5 km and horizontal distances of 1.55 to 1.7 and 1.9 to 2.05 km. The distance from the Katsuragi station to the site is 73 km. Assuming that the radar gain is 9.46 dB, radar cross section of ship radar matches that of X-MP radar in **Figure 4.10**. The colorbar shows 10-minutes averaged wind speed at the tower. Horizontal bar shows maximum and minimum value in the target area. In this analysis, all duration (approximately 3 months) data was used. Following equation shows the difference depending on the radar gain.

$$NRCS_{diff} = (NRCS_{XRAIN} - NRCS_{Ship})^2. \tag{4.4}$$

The results are in **Figure 4.11**. The minimum value is 1.93×10^4 when radar gain is set as 8.1 [dB]. Using the estimated radar gain, normalized cross section

from radar observation is obtained by **Eq**.(4.3). **Figure 4.12** shows spacial distribution of normalized backscattering radar cross section. This method forced us to evaluate physical quantities of black-and-white color images.

4.5 Estimation method of height sea clutter reaches

Since meteorological radar targets rainfall, they should be conducted as close to the ground as possible because the purpose is to know accurate rainfall intensity and rainfall amount to mitigate disasters. However, radar can be reflected by ground: sea surface and land. To reduce the reflection from the both, the elevation angle is set at high gazing angle, although the radar observes the area above the clouds. Therefore, radars managed by MLIT perform quality control for each observation point to determine the observation elevation angle. The altitude of clouds differs between summer and winter, so it is necessary to set the elevation angle for each season. Because some sites are located at more than 1 km above the sea level, in winter season the gazing angle should be negative. In addition, the radar has horizontal and vertical beam widths and is fan-shaped, so the farther the distance from the radar is, the longer the fan is, and the larger the representative observation area becomes. When the ground or sea surface enters the volume of the beam, the reflectivity becomes strong, and it becomes ground clutter or sea clutter. In the case of ground clutter, it can be removed from the observation results by using the Moving target indicator (MTI) method. However, for example the C-band MP radar installed at Mt. Otobe-dake in Hokkaido requires a negative elevation angle, but since rainfall in some areas is subtracted by MTI, the target area is compensated by a high elevation angle value(91). In this way, the effects of ground clutter are removed by examining each region. In the case of sea clutter, it is identified by comparing weak and strong winds on the axis of wind speed and is sometimes equivalent to rainfall intensity is around 1 mmh^{-1}. It is difficult to identify the location of the sea clutters, although they interfere with rainfall observations. If it is determined, it is replaced by the value of high elevation angle as in the case of ground clutter.

That is because radar observations at low elevation angles are usually compensated by observations at high elevation angles, instead of using data from that area. In common sense in radar observation, low angle data is removed from its analysis. However since the target is sea spray in this study, the height sea clutter reaches should be known. The concept of this radar observation is shown in **Figure 4.13**. The high altitude area contains only raindrops. At lower altitude contains rain and sea spray and the number of sea spray becomes bigger and bigger. And reflectivity from sea surface becomes biger. In this section, estimate of the height at which the effect of sea clutter is proposed and data above that height is used in this study.

Firstly, radar beam has power density within the shape of beam. The power density distribution of the radar beam width has been measured as a known parameter in the case of radars intended for rainfall observation such as X-band MP radar. However, since the radar used in this study is a marine radar and only captures the presence or absence of ships, there is little information needed for quantification, as mentioned. One of them is the power density distribution of the radar beam width. The power density distribution is assumed to be normally distributed, referring to the power density distribution described in the paper. The density distribution within the beam width is shown in **Figure 4.14**. This shape represents the main lobe of radar beam and is described by following Gaussian equation:

$$f(x) = \frac{1}{\sqrt{2\pi}} \exp\left(-\frac{x^2}{2}\right).$$

The **Figure 4.15** shows a schematic diagram of radar beam and sea surface. Because the distance from radar and the target is far enough approximately 1.8 km compared with radar height which is approximately 2 m, the radar height can be considered as zero. Another setting of calculation is that the wave surface is up and down with wave height observed at the tower horizontally as shown in **Figure 4.15**. The elevation angle of the radar is set to 0 degrees, and the cumulative value of the power density irradiated to the sea in the fan beam, P_0, is 0.5, because the half of power density is radiated to the sea surface. Assuming that, the integration range is from $-\infty$ to 0, and the cumulative value is 0.5. Next, we calculate the area of the sea included in the fan beam at a certain elevation

angle Θ, and integrate the power density irradiated to that area to obtain the cumulative value of the power density irradiated to the sea surface P_Θ. The sea clutter P_{rs} from the sea surface at a certain elevation angle is expressed by the following equation.

$$P_{rs} = P_{r0} \times \frac{P_\theta}{P_0} \tag{4.5}$$

Since the minimum received power of the ship radar is -100, the height at which P_{rs}=-100 is the maximum height at which the sea clutter can reach. For the sake of simplicity, we do not consider Bragg scattering and mirror point scattering, which represent the scattering of sea surface waves. Using **Eq**.(4.5), the received power from sea surface can be described as follows:

$$P_r(\theta) = 10\log_{10}\left(\int_{\theta_{low}}^{\theta_{high}} f(\theta)d\theta \times P_{rmax}\right) \tag{4.6}$$

Here, $P_r(\theta)$ is the received power of sea clutter at the angle of θ, $\theta_{low/high}$ is angle at which radar is radiated for sea surface, P_{rmax} is maximum value of received power. This value is from observation result at 0 m height. **Figure 4.16** shows an example of calculation **Eq**.(4.6). In this case, P_{rmax} is 3.16×10^{-7} (-65 dBm). Sea clutter reaches 10 m height. From this methodology, the height of sea clutter is estimated.

4.6 Horizontal wind speed profile and drag coefficient

In this section, vertical profiles of horizontal wind speeds are estimated by using radar images. Radar image clearly has the characteristics of horizontal advection of rain drops as shown in **Figure 4.2**. Hypothesizing that the advection of rain is the same as the wind speed, estimation of horizontal wind speed is achieved from the images. The shape apparently looks like logarithmic profile in this case. However, the profile of horizontal wind speed changes from moment to moment. We need to recognize that the logarithmic profile is averaged situations. After understanding it, the logarithmic profile is utilized in this section. The

profiles of horizontal wind speed is generally described as logarithmic profiles of neutral atmospheric stability as follows.

$$U(z) = \frac{u_*}{\kappa} \ln\left(\frac{z}{z_0}\right) \tag{4.7}$$

Here, $U(z)$ is horizontal wind speed at altitude of z, u_* is friction velocity, κ is karman constant, z_0 is roughness length. At least two horizontal wind speeds at different height z_1, z_2, friction velocity and roughness length can be estimated.

$$U(z_1) = \frac{u_*}{\kappa} \ln\left(\frac{z_1}{z_0}\right)$$
$$U(z_2) = \frac{u_*}{\kappa} \ln\left(\frac{z_2}{z_0}\right)$$

Then, solving for friction velocity,

$$u_* = \frac{\kappa(U(z_1) - U(z_2))}{\ln(z_1) - \ln(z_2)}$$

Also, the horizontal wind speed at 10 m height is

$$U(10) = \frac{u_*}{\kappa} \ln\left(\frac{10}{z_0}\right).$$

Using wind speed at 10 m height and friction velocity, the drag coefficient is

$$C_{d10} = \left(\frac{u_*}{U_{10}}\right)^2. \tag{4.8}$$

From **Eq.**(4.7) to **Eq.**(4.8), the drag coefficient can be estimated. To achieve this estimate, the horizontal wind speed profiles are required. In the next subsection detailed methodology is introduced.

4.6.1 Methodology for estimate of horizontal wind speed

The detailed of methodology is introduced in this subsection. The flow chart is shown in **Figure 4.17**. In Step1, time periods when dominant wind direction is south to north is extracted. This means that wind and radiated electro-magnetic wave propagate in the same direction. In Step 2, radar images are classified into each groups based on 10-minutes averaged horizontal wind speed observed

by wind anemometer at 23 m height of the observational tower. The groups are 20 to 25 ms^{-1}, 25 to 30 ms^{-1}, 30 to 35 ms^{-1}, and 35 to 40 ms^{-1}. After the classification, radar images are again investigated one by one to find possibility of estimating wind speed in Step 3. In Step 4, estimate of horizontal wind speed at each height on Hovmöller diagrams is conducted. One example of process is shown below. Checking the images carefully, as shown in **Figure 4.18**, the mass moves left to right. The time difference of these pictures is 2.6 seconds. To clearly see this mass, threshold of image value is set and convert value less than the treshold into 0 (blue in **Figure 4.19**). After remove these grids, Hovmöller diagrams are made, shown in **Figure 4.20**. Horizontal axis shows distance and vertical axis shows time. The horizontal distance is from 0.5 to 1.5 km. The sampling time is maximumly 21 seconds. **Figure 4.21** is one example of Hovmöller diagram at the height of 0.39 km. Red dots are decided as following equation, which indicates average distance from radar origin:

$$D = \frac{\sum_x^{x_{max}} r_x \times P_x}{\sum_x^{x_{max}} P_x}$$

And the red line is drawn based on least-squared method. This trend line shows wind speed. **Figure 4.22** shows results for all height. Results from 30 to 150 m heights (55 points) are used in following analysis. The low area less than 30 m height is excluded from this analysis because the area contains sea clutter. This is the methodology to estimate horizontal wind speed by Hovmöller diagrams in Step 4. In Step 5, data exceeds 100 ms^{-1} and blow 0 ms^{-1} are excluded. In Step 6, quality control is conducted using order statistics of respective heights. The thresholds of percentile are set as 0 to 100th percentile, 25 to 75 percentile and 35 to 65 percentile. In Step 6, averaged horizontal wind speed at each 10 m height is calculated. For example, an order statistics at 30 m height. Then, 1st to 24th percentile and 76th to 100th percentile data are excluded. This process is conducted for each 2.2 m height. Then, in Step 7, we calculate the average of the data within the height from 30 to 40m as the averaged value at 35 m height. In Step 8, we draw scatter diagram on semi-logarithmic graph. One example is shown in **Figure 4.23**. From this figure, wind speed profile below 60 m height follows logarithmic profile in Step9. Then, we have decided to use data below

up to 60 m height for Step 10. The friction velocity and roughness length are estimated by applying log-normal distribution for the data obtained in Step 9. Horizontal wind speed at 23 m height is estimated by the log-normal distribution and calculate the ratio against horizontal wind speed at 23-m obtained from the wind anemometer in Step 10. We set the threshold of ratio as 0.8 and 1.2 in Step 11. In Step 12, the ratio and the averaged horizontal wind speed used in Step 10 are multiplied together. In Step 13 and 14, again we apply the log-normal distribution for horizontal wind speeds of not only radar data but also wind anemometer data. In Step 14.a, both wind speeds at 15 m and 23 m heights are included. In Step 14.b, either wind speed at 15 m or 23 m height is included. In Step 14.c, averaged wind speed of 15 and 23 m height is included as wind speed at 19 m. Finally, 14 types of the friction velocity, wind speed at 10 m height, roughness length and drag coefficient are obtained in Step 15. This is the whole processes to estimate profiles of wind speeds from radar observation images.

4.6.2 Results of estimate of profiles of horizontal wind speeds

The results of the estimates are introduced in this subsection. We conducted the analysis explained in previous subsection for approximately 1200 images equivalent to 40 minutes data. The maximum averaged wind speed at every 10 minutes is 39.5 ms^{-1} at 23 m height. These 1200 images are classified into 4 groups which are from 20 to 40 each 5 ms^{-1}. In the 40 ms^{-1} group, 9 cases are obtained. The averaged wind speed is 34.6 ms^{-1} and standard deviation is 2.2 ms^{-1}.

Figure 4.24 shows the profiles of horizontal wind speeds from 20 to 40 ms^{-1}. Here, the thresholds are set to 25th to 75th after excluding the outliners. The other results are summarized in **Table 4.1**. And also these results have standard deviation due to the 12 types of estimate methods are applied. Thus, each standard deviations are shown in **Table 4.2**. The relationship between wind speed at 10 m height and drag coefficient is shown in **Figure 4.25**. Small dots shows 12 patterns: 3 patterns (Step 7 a, b, c) $\times$ 4 patterns (Step 14 a, b, c) in

Table 4.1: Results of the estimate of drag coefficient, friction velocity, roughness length and horizontal wind speed at 10 m height.

U_{23} [ms^{-1}]	C_D [-]	u_*	U_{10}	z_0
20∼25	8.2×10^{-6}	0.57	20.7	7.6×10^{-4}
25∼30	2.7×10^{-3}	1.20	23.5	6.0×10^{-3}
30∼35	4.0×10^{-3}	1.70	27.5	0×10^{-3}
35∼40	2.1×10^{-3}	1.50	34.6	5.7×10^{-3}

Table 4.2: Results of the estimate of standard deviation for each variables.

U_{23} [ms^{-1}]	C_D [-]	u_*	U_{10}	z_0
20∼25	1.42×10^{-6}	0.05	0.33	9.4×10^{-6}
25∼30	9.4×10^{-4}	0.19	1.47	6.5×10^{-3}
30∼35	1.6×10^{-3}	0.33	1.19	0×10^{-3}
35∼40	1.4×10^{-3}	0.45	2.19	1.2×10^{-3}

the flow chart. Bigger dots is mean value of 12 patterns and bar shows standard deviation.

4.7 Summary and conclusions

In this chapter, results of radar observation are introduced and conversion methods into normalized backscattering radar cross section and wind speeds are proposed. In 2018, three extreme typhoons are observed by ship radar. The typhoon JEBI caused the averaged wind speed of 39.5 ms^{-1} at 23 m height. This is the maximum wind speed in this observation duration.

The radar image is converted into backscattering radar cross section by proposed method. The methodology contains quality control and estimate of radar gain. After taking these processes, the normalized radar cross section, which is a physical quantity that represents the degree of scattering by materials is obtained. This method can be applied to radars that are generally used as weather radars.

For example, since meteorological radars installed in various parts of Japan have overlapping observation ranges, it is possible to estimate the parameters required for radar observations by comparing the observation results of both radars at the same observation point. This method can be applied not only to ground-based radar but also to satellite radar because it uses the radar equation based on electromagnetism.

Another problem in radar observation is sea clutter. In this chapter, we estimated the height at which the sea clutter reaches. In this study, the height of the sea clutter is estimated by considering the width of the radar beam and the wave height, enabling the analysis of data at low altitudes that would otherwise be removed. This method can be used not only for the observations in this study, but also for low-elevation observation data during approaching typhoons and in winter.

The last methodology proposed in this chapter is to estimate horizontal wind speeds at each height. This method enables to calculate the drag coefficient under typhoons. In this observation, drag coefficient with up to 40 ms^{-1} is estimated. This estimation method based on Hovmöller diagram has characteristics that wide range of wind speed is calculated even below 0 and above 100 ms^{-1} Furthermore, the threshold of wind direction is set as south from 135 to 225 degree. That means real wind speed and estimated wind speed is different from about 1.4 times.

The author set as three thresholds to exclude outliers. The method of rejecting outliers can be discriminated by hypothesis testing. The previous study suggested that the relationship between averaged wind speed and instantaneous wind speed estimated from observation results during typhoon events(93). Further analysis can be conducted by assuming the histogram of wind speed follows a distribution, for example Weibull distribution. Goda (1990)(92) excludes outliners with some distribution of wind speed: Weibull, log-normal distribution. Method for ex In the next chapter, the particle size distribution is estimated from the normalized backscattering cross section obtained in this chapter.

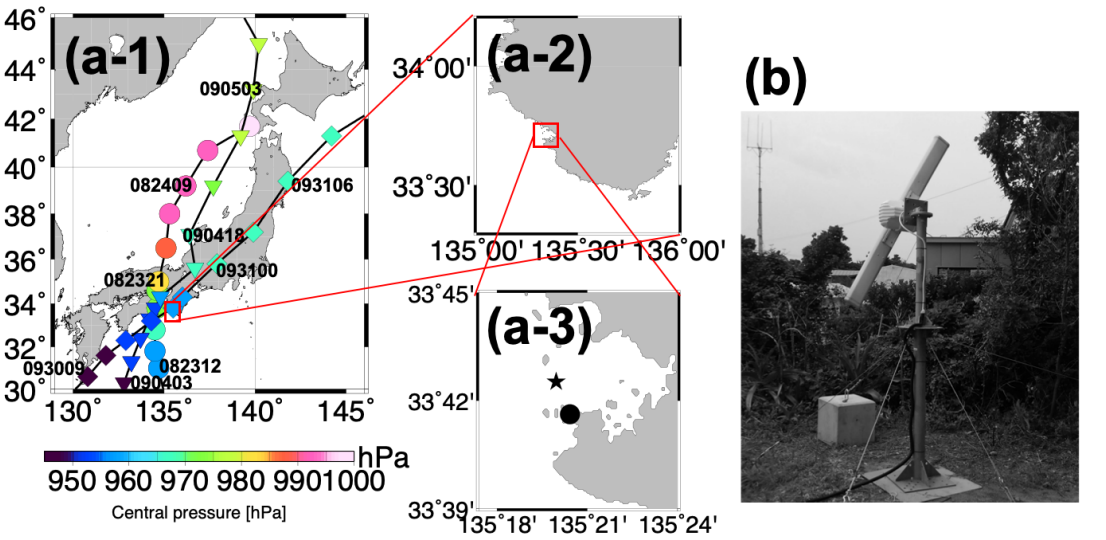

Figure 4.1: Overview of the observation with ship radar - (a-1, 2, 3) Typhoon path, central pressure, observation points and (b) installation of ship radar. The circles in (a-1) indicate the typhoon path and the color bar indicates the central pressure of the typhoon. Circles indicate Typhoon 20 (CIMARON), inverted triangles indicate Typhoon 21 (JEBI), and squares indicate Typhoon 24 (TRAMI). The date and time (JST; mmddhh) are shown in the figure. (a-2) is an enlarged image of the Kii Peninsula. The enlarged image in the red frame of the same figure is (a-3). The circle in (a-3) indicates the location of the radar and the star indicates the location of the observation tower.

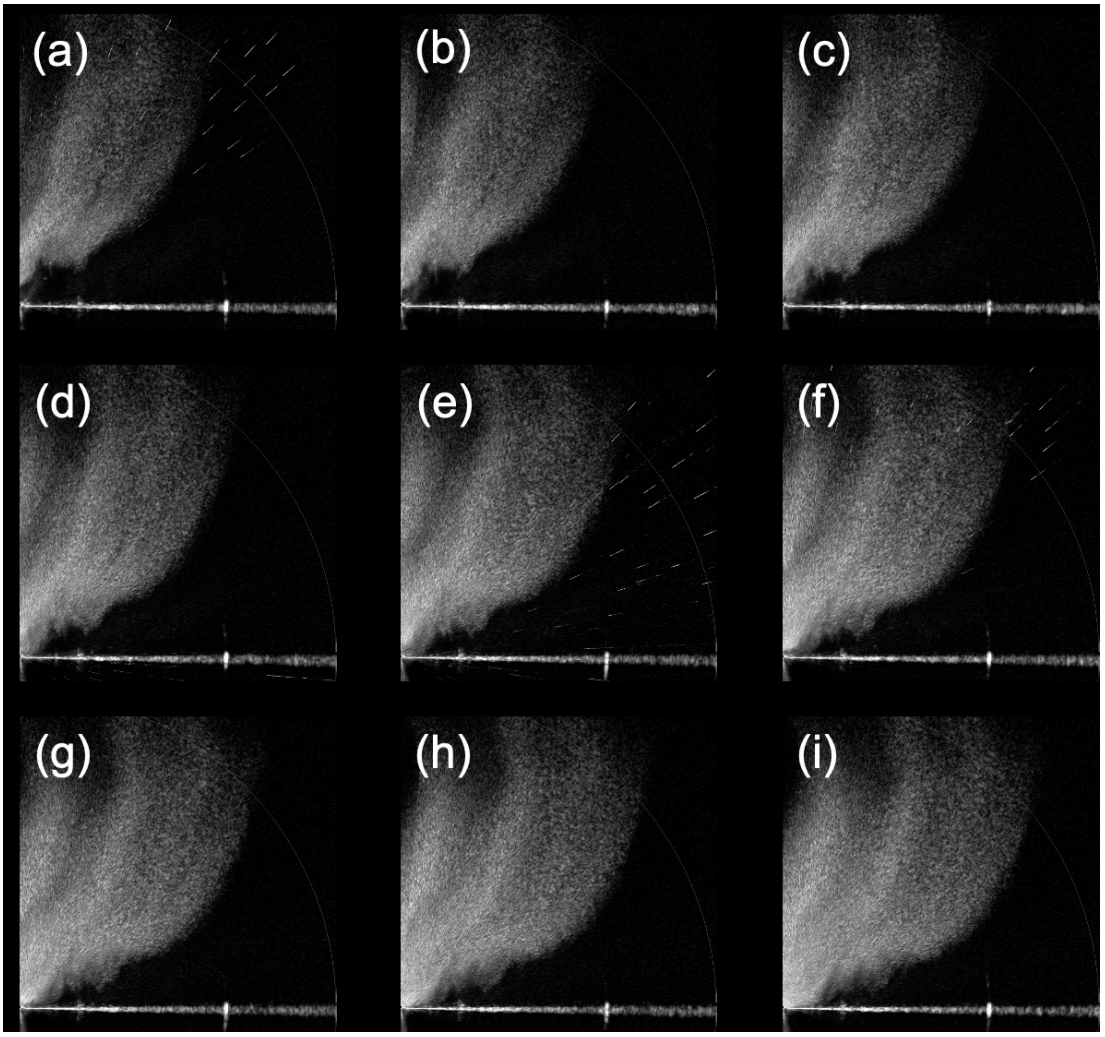

Figure 4.2: Radar images taken every 2.6 seconds - These data were obtained during the passage of Typhoon No. 20, with an hourly mean wind speed of 11.2 ms^{-1} and rainfall intensity of 0.5 mmh^{-1} at AMeDAS.

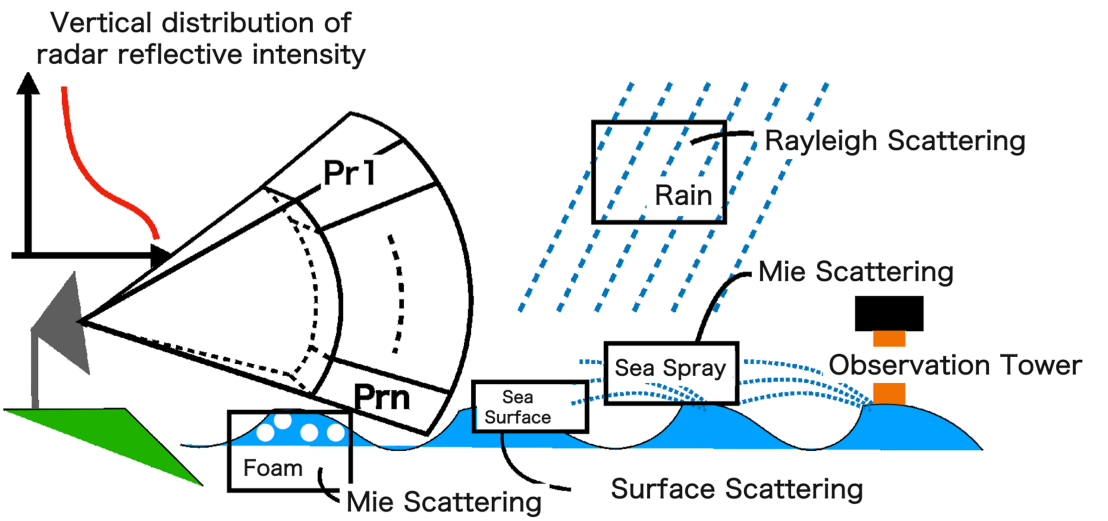

Figure 4.3: Ship radar observation and scatterers are rain, foam, sea surface and sea spray. - The factors that scatter electromagnetic waves and their respective scattering type are shown.

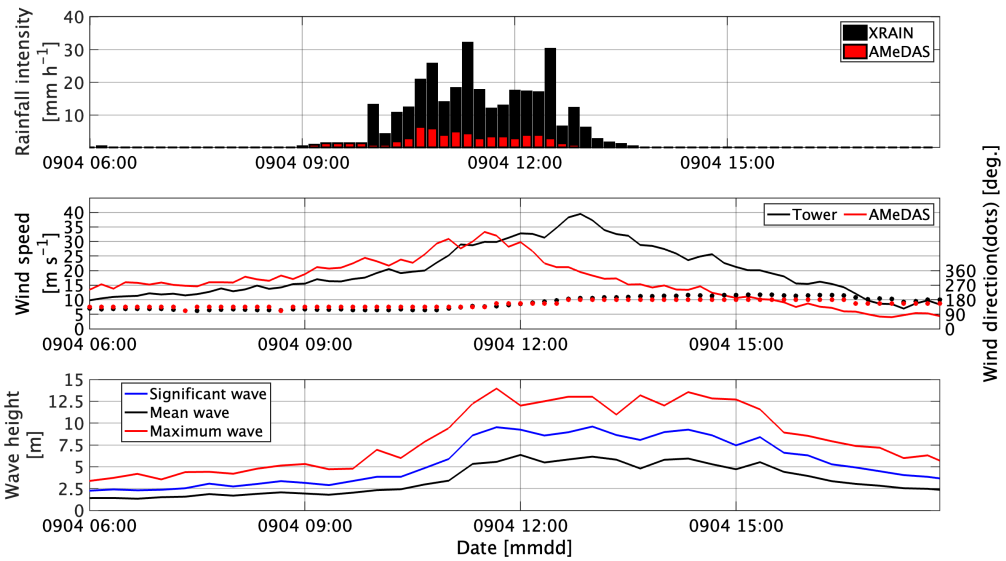

Figure 4.4: Time series of rainfall intensity, wind speed and direction, and wave height from 06:00 (JST) on 4th September 2018 to 18:00 on 4th September 2018. - (a) Hourly rainfall [mmh^{-1}] at each 10 minutes at the X-MP radar (Black) and AMeDAS sites (Red). (b) 10-minute mean wind speed and direction at the observation tower (Black) and AMeDAS sites (Red). Wind direction is defined clockwise with north direction at 0 $^{\circ}$. (c) 10-minute maximum wave height (Red), significant wave height (Blue) and mean wave height (Black) [m] at the observation tower.

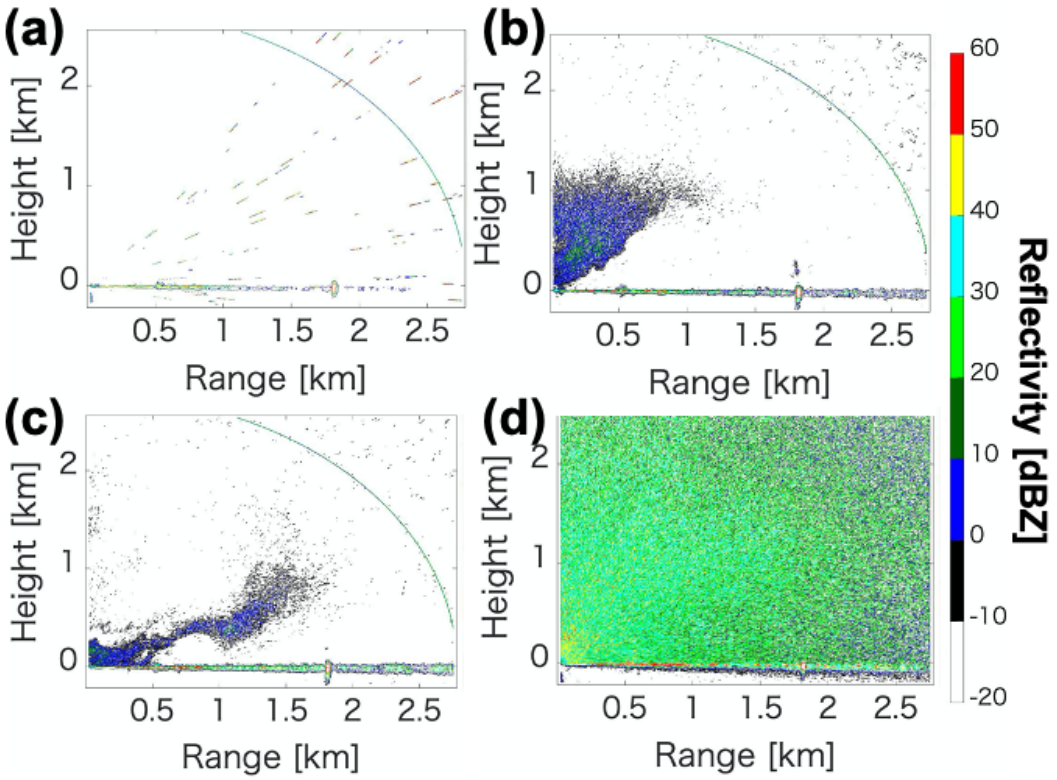

Figure 4.5: Snapshot of radar observation on August 23. - The contour represents the reflection intensity [dBZ]. The curve in the figure represents the distance of 2.7 km, and the radial lines from the center are noise caused by radar interference. (a) represents 0:00:00, (b) represents 8:30:00, (c) represents 10:40:00, and (d) represents 23:00:00. The origin of each figure is the position of the radar, and the strong reflection intensity in the range of about 1.8 km is the reflection from the observation tower. The rainfall (at AMeDAS), wind speed and wind direction (at the observation tower) are as follows. (a) 0 mm/10mins, 10.11 ms^{-1}, east, (b) 0 mm/10mins, 8.32 ms^{-1}, east-southeast, (c) 0 mm/10mins, 11.72 ms^{-1}, south, (d) 7 mm/10mins, 26.0 ms^{-1}, south.

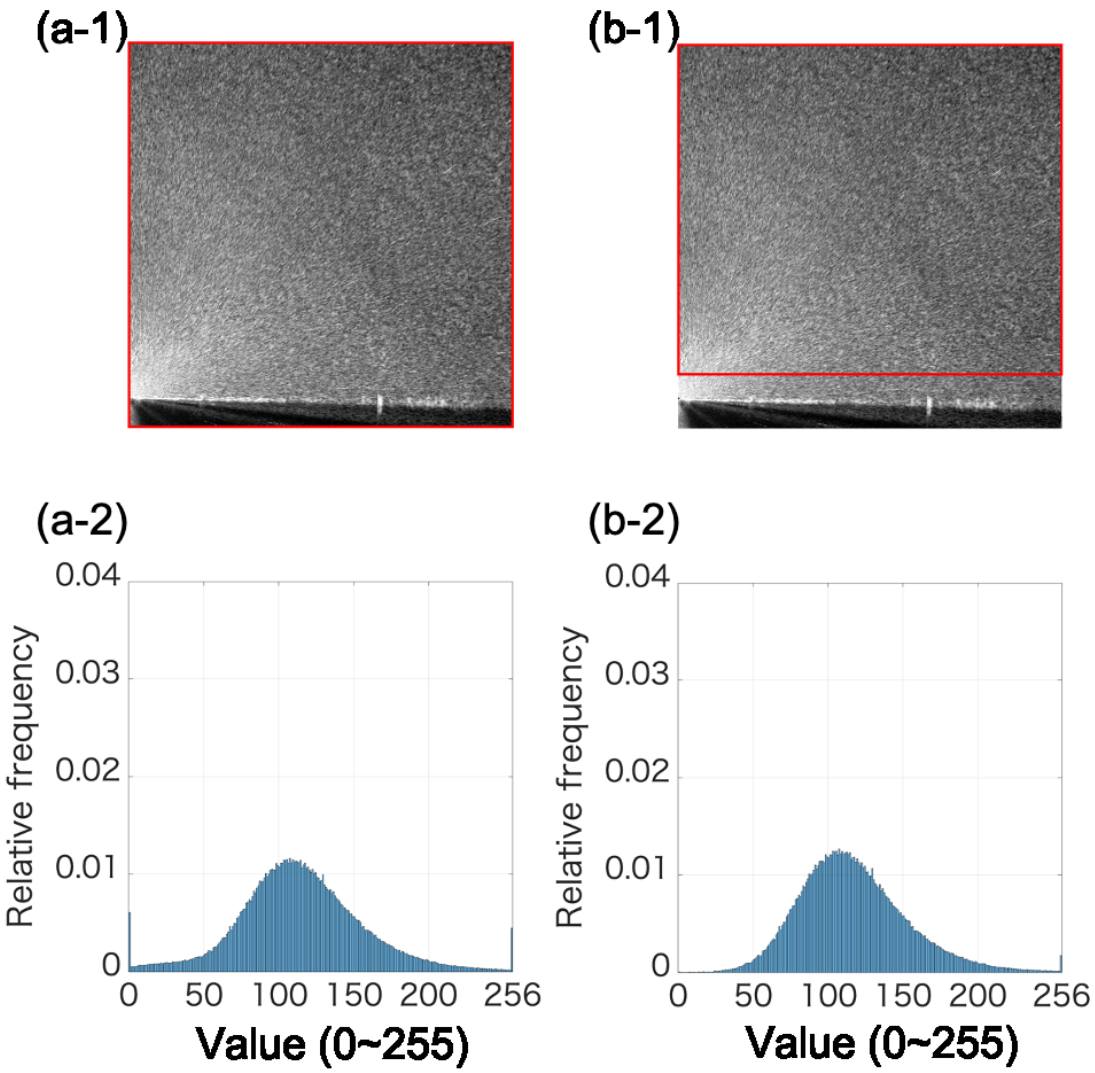

Figure 4.6: Raw observation data and histogram of gradation from 0 to 255 - (a) raw data and histogram for all area surrounded by red rectangular, (b) raw data without sea clutter zone.

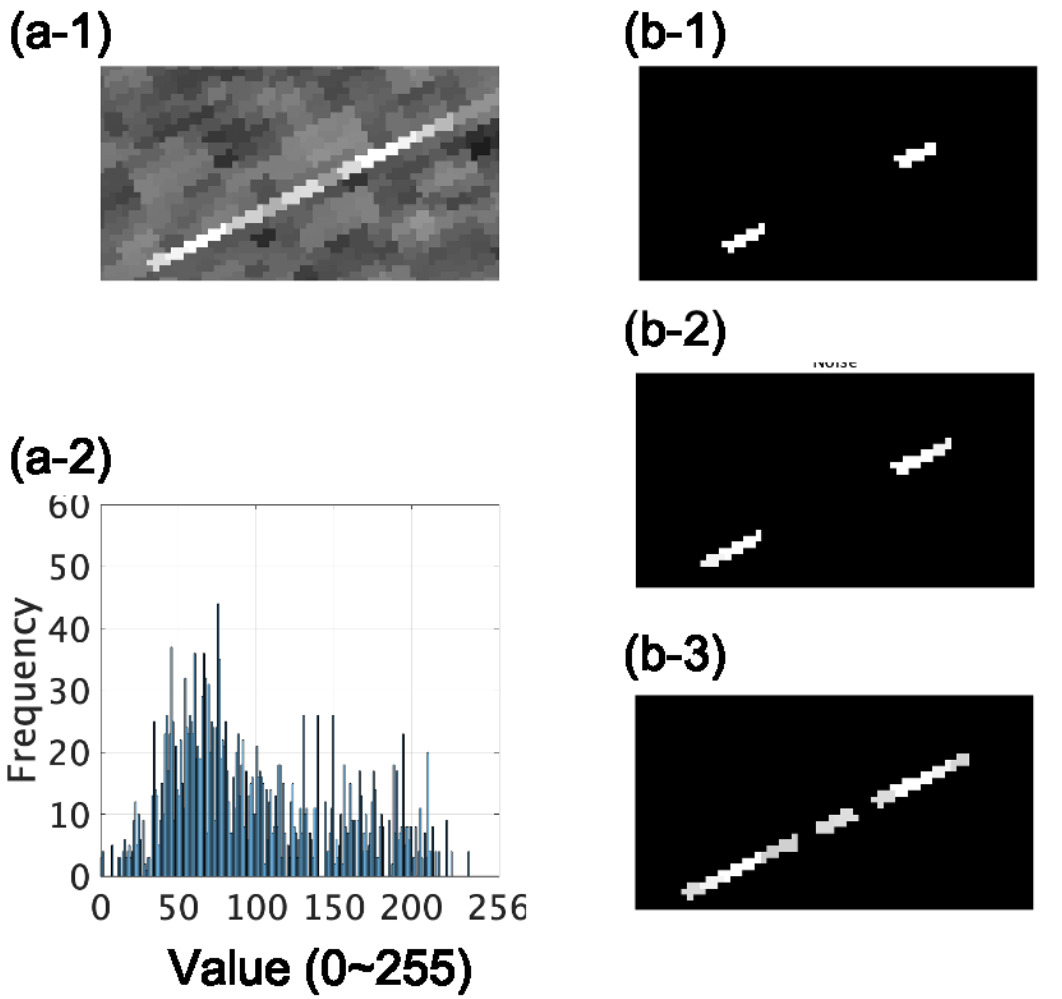

Figure 4.7: Raw data and histogram around radial noise. - (a-1) raw data around noise, (a-2) histogram of raw data shown in (a-1), (b) raw data with threshold of 255 (b-1), 230 (b-2), 200 (b-3).

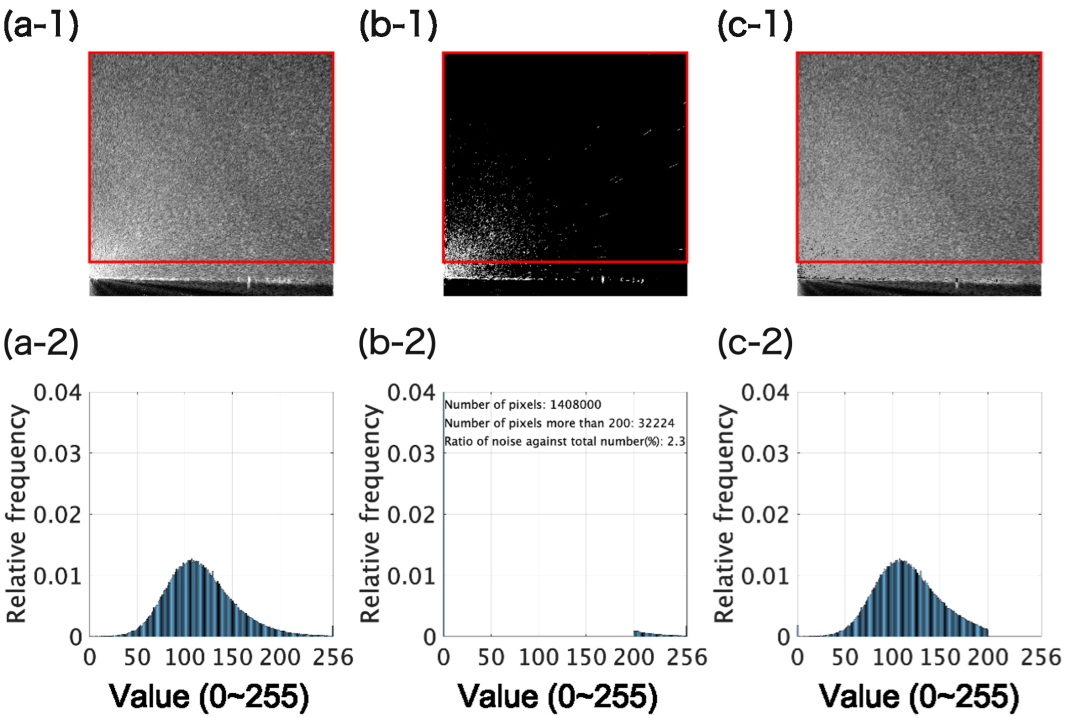

Figure 4.8: Raw data, modified data and histograms - Group (a) shows raw data, (b) shows data above the threshold of 200 and (c) shows interpolated data.

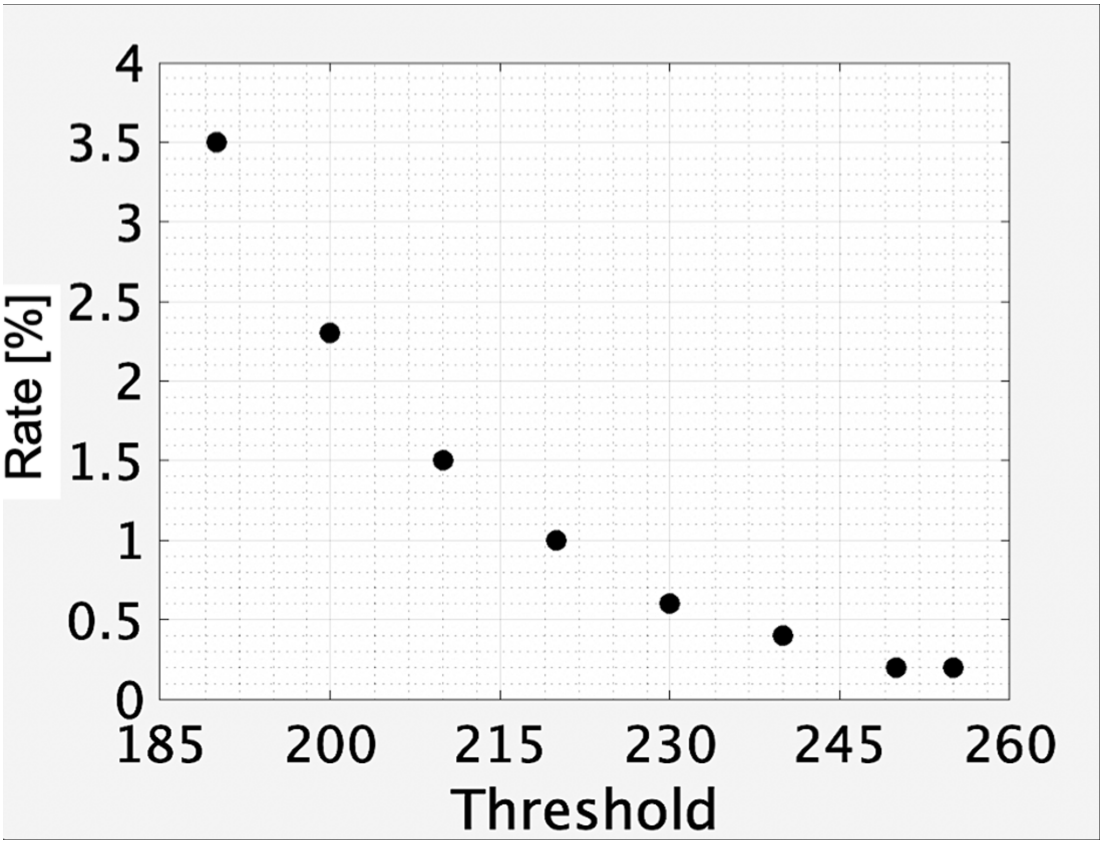

Figure 4.9: Relationship between threshold and rate. - Vertical axis indicates the rate of the number of pixels containing noise to the total number of pixels. Horizontal axis shows threshold.

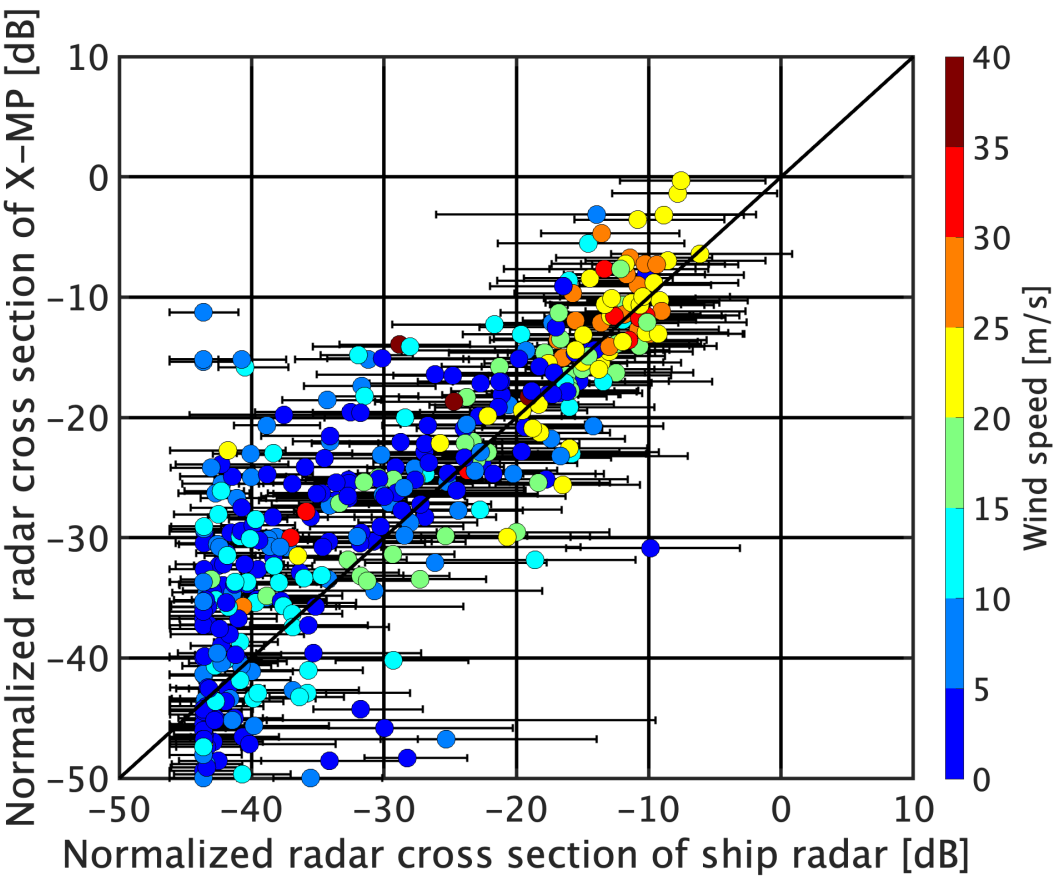

Figure 4.10: Comparison of the normalized radar cross section obtained from the X-MP radar with the normalized radar cross section of the ship radar obtained assuming a gain of 9.46 dB. - Bar represents the standard deviation and the color bar represents the rainfall intensity of the X-MP radar.

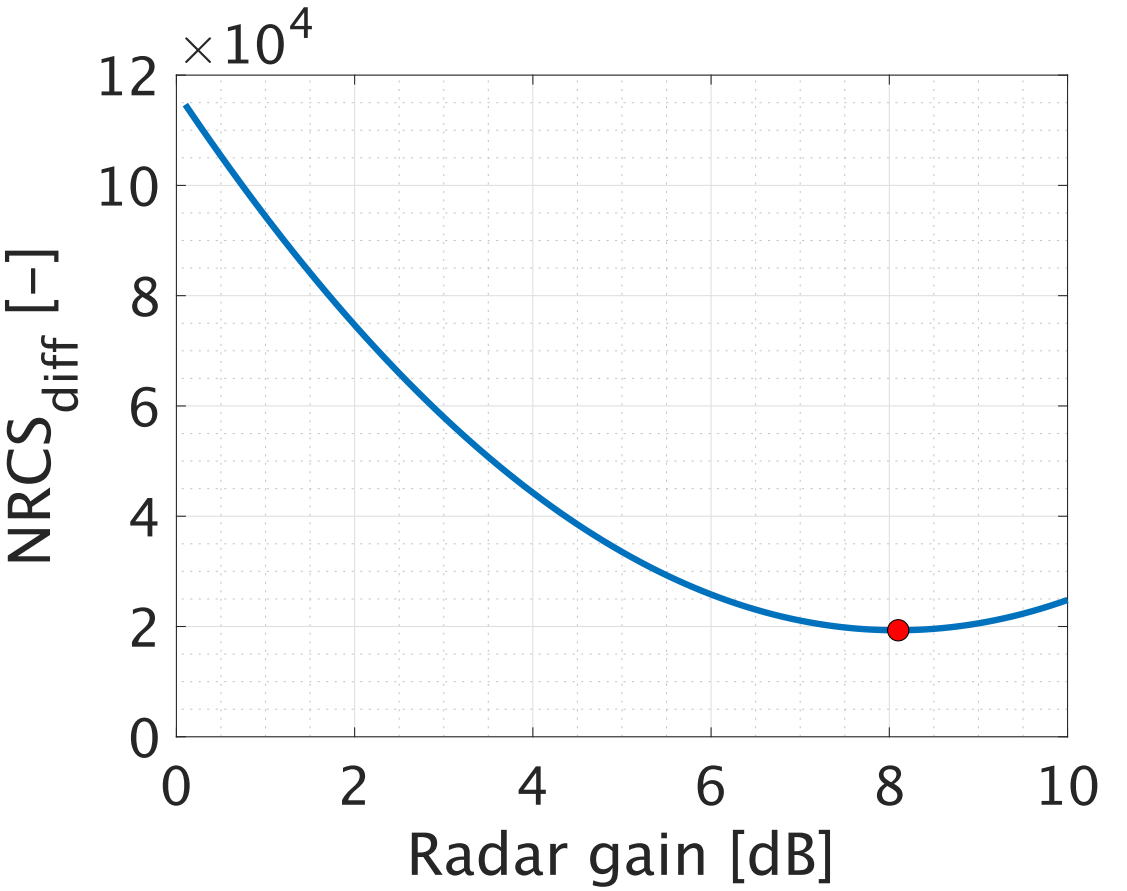

Figure 4.11: Relationship between radar gain and difference of normalized radar cross section. - The difference in vertical axis is calculated by **Eq**.(4.4).

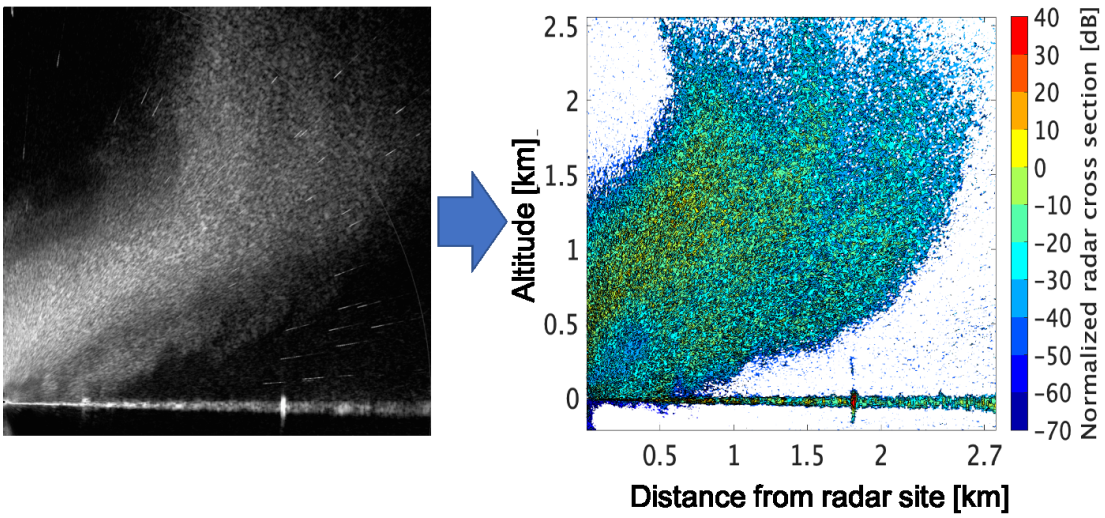

Figure 4.12: Conversion from raw data into normalized radar cross section. - Color shows normalized radar cross section [dB].

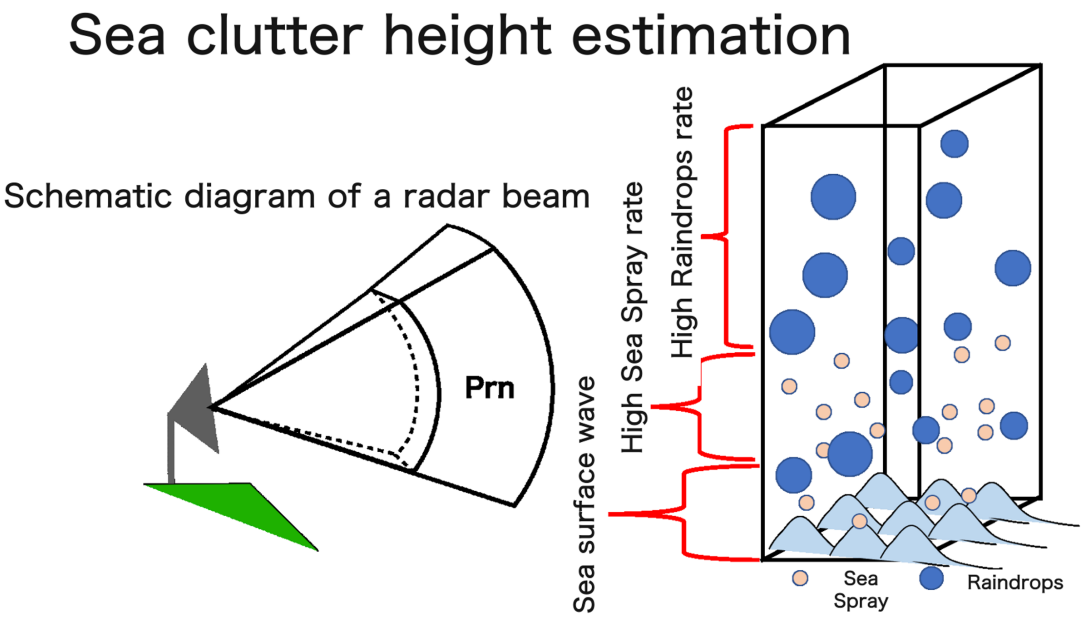

Figure 4.13: Conceptual diagram of the radar beam and the distribution of raindrops, droplets, sea surface, and foam in space. - Blue circle is rain drop, orange circle is sea spray.

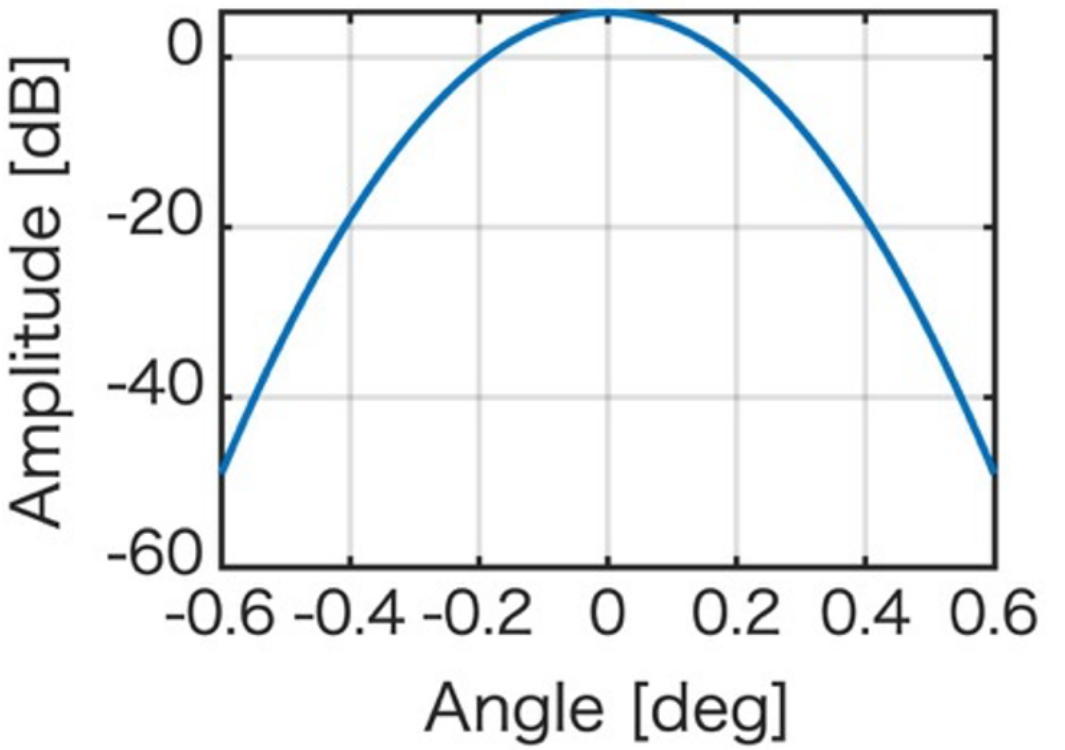

Figure 4.14: Distribution of electric density in radar beam - Only the main lobe of the power density distribution is shown.

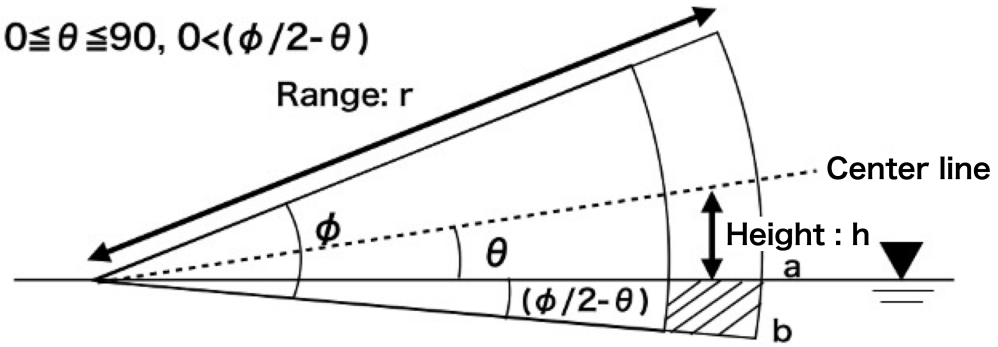

Figure 4.15: Schematic diagram of estimation method of the height sea clutter reaches. - The hatched area indicates beam width radiated for sea surface.

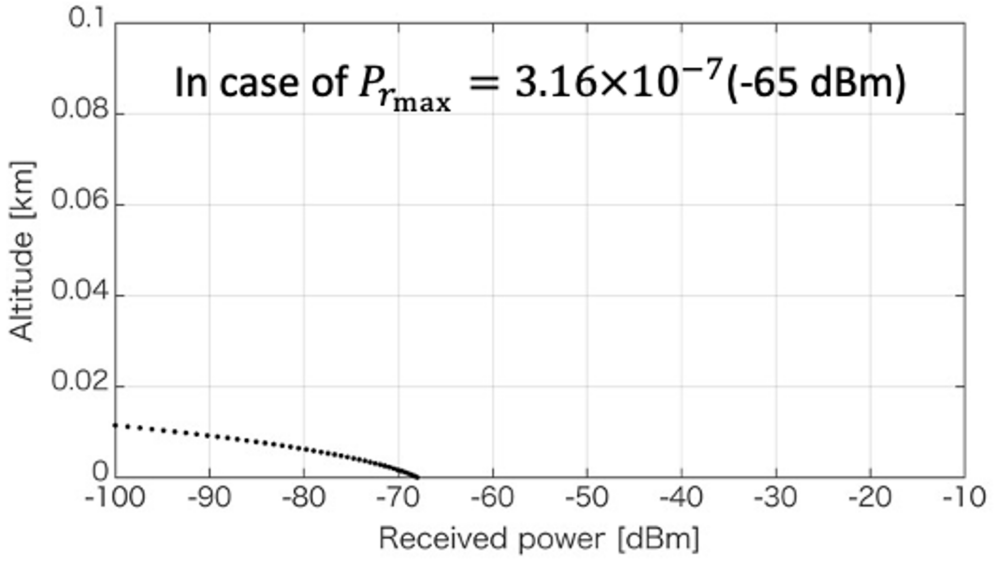

Figure 4.16: Vertical Distribution of Radar Received Power by Sea Clutter. - In this case P_{rmax} is 3.16×10^{-7} (-65 dBm).

4. ESTIMATION METHOD OF RADAR GAIN AND SEA CLUTTER

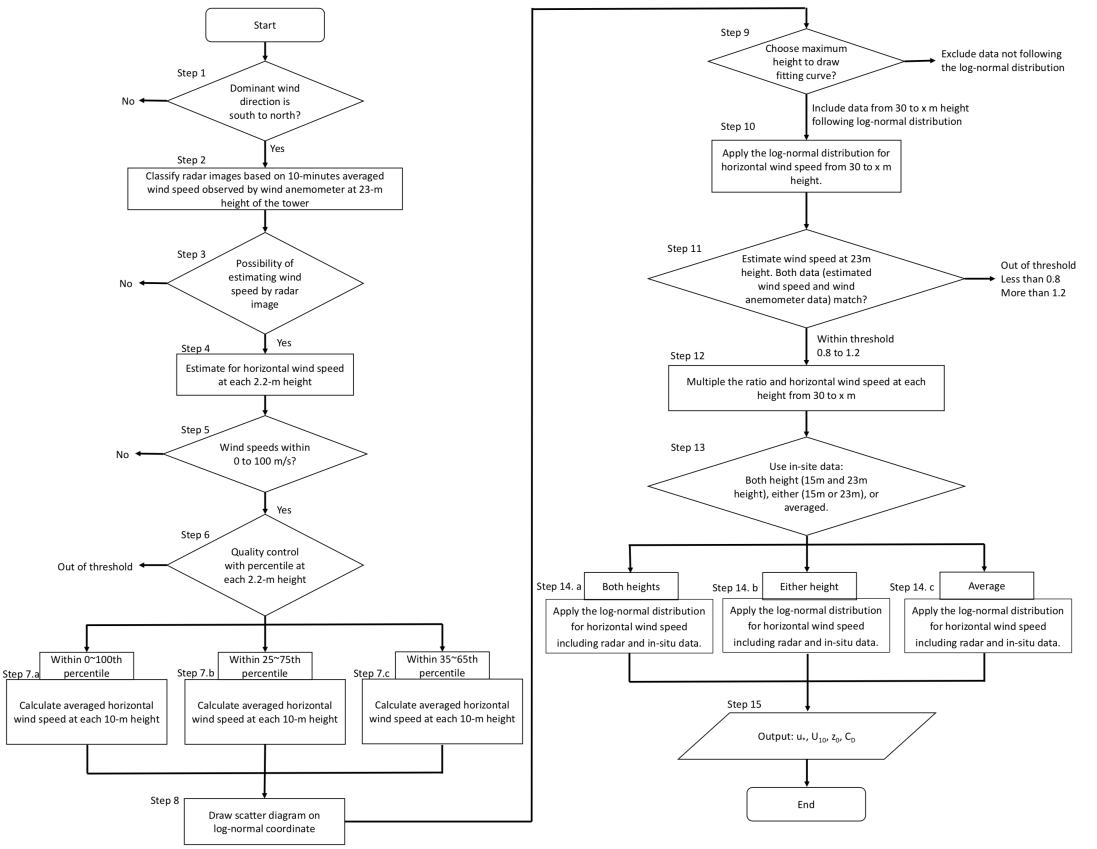

Figure 4.17: Flow chart for estimate profiles of horizontal wind speed. - Whole processes consist of 15 steps.

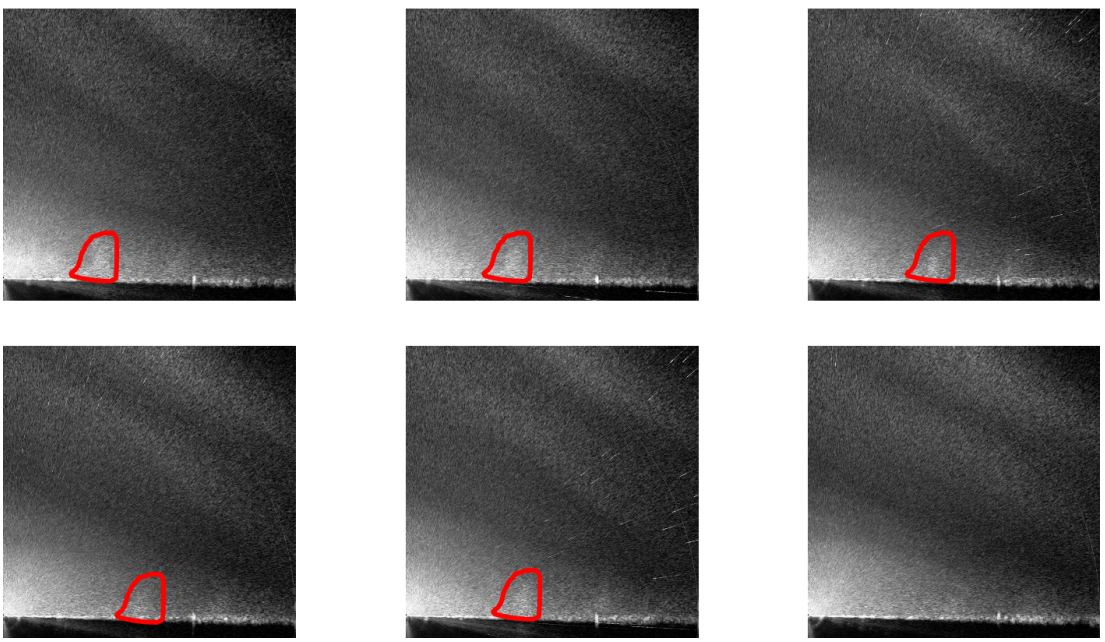

Figure 4.18: Raw images. - Red area moves left to right.

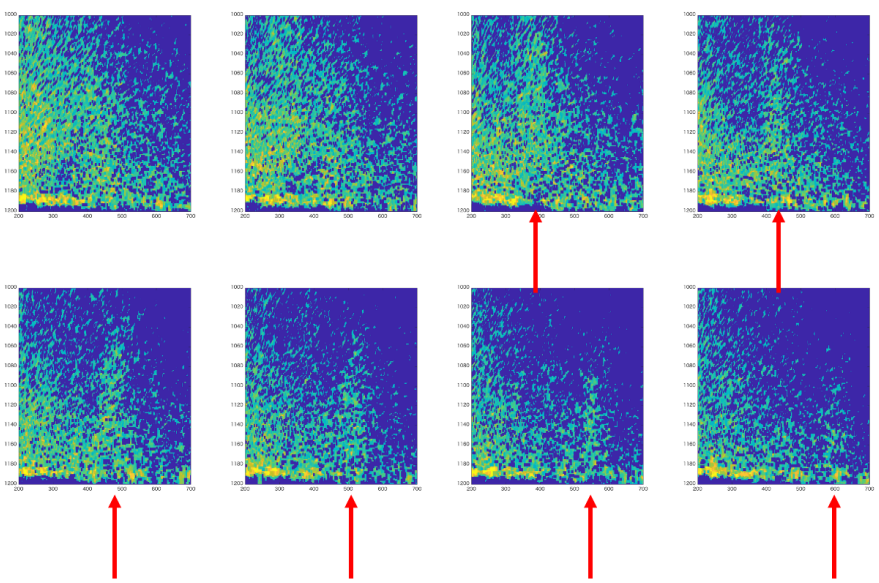

Figure 4.19: Raw images with threshold of value at 115. - Arrow shows the position of mass moving left to right.

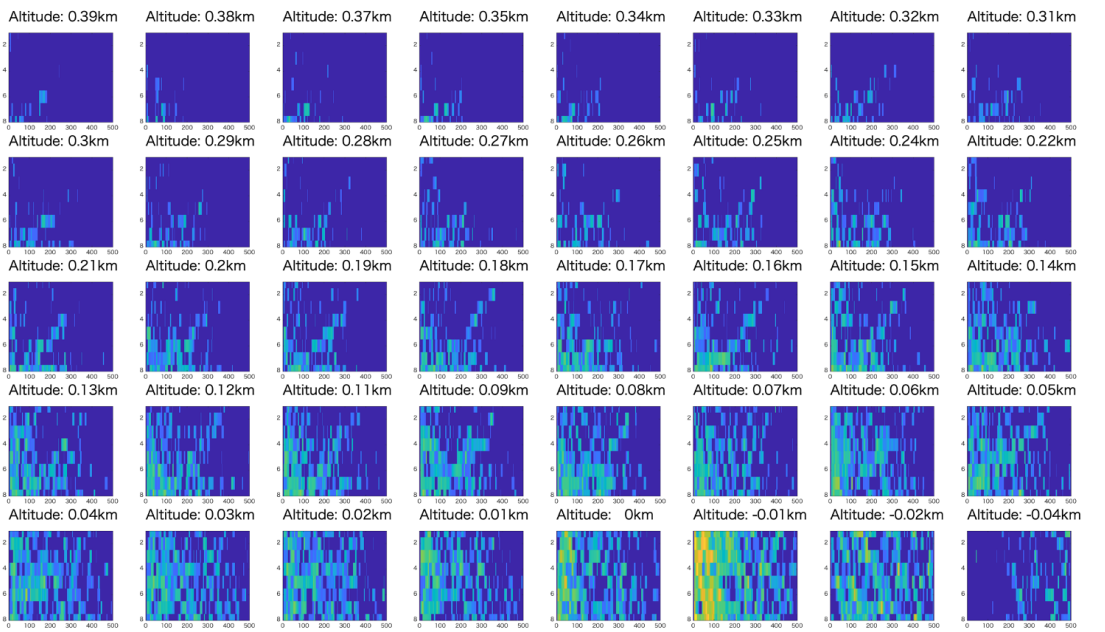

Figure 4.20: Hovmöller diagram at each height. - The height is from -0.04 (under the surface) to 0.39 km.

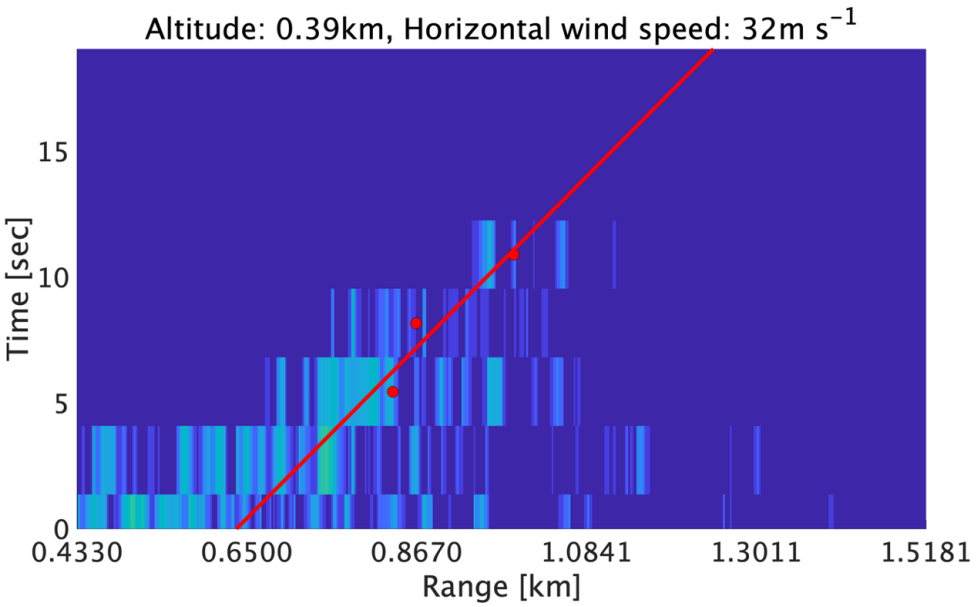

Figure 4.21: Example of Hovmöller diagram at the height of 0.39 km. - Red dots is averaged distance weighted by image value. Red line shows a result of least-squared method.

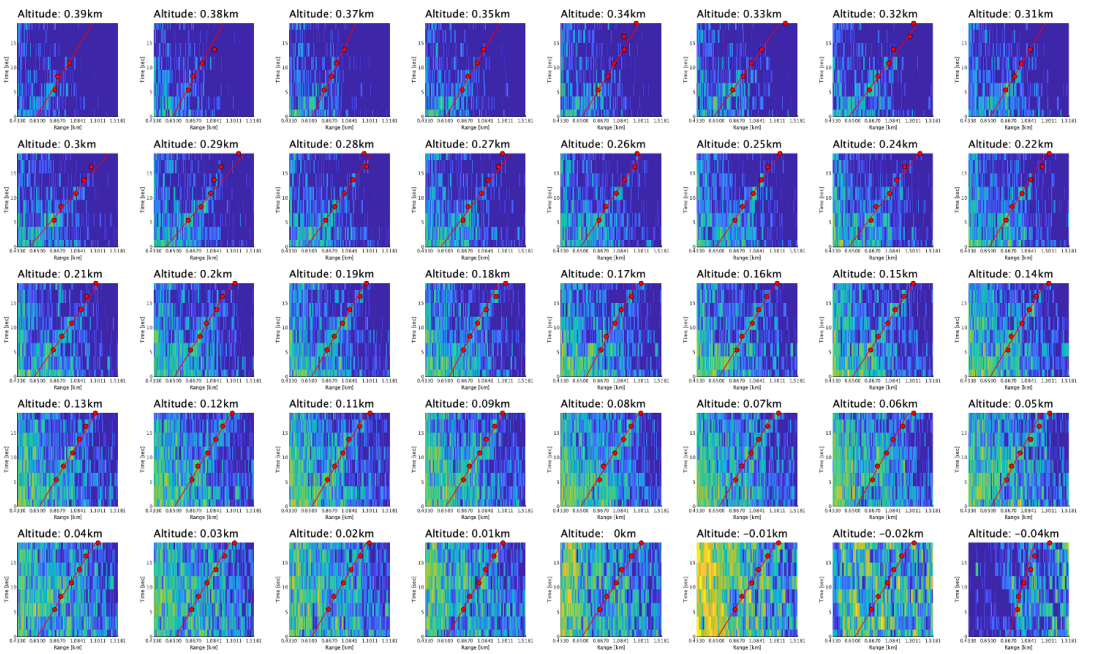

Figure 4.22: Hovmöller diagrams at each height with the line estimated by least-squared method. - Same as **Figure 4.20**, but with red dots which indicate averaged distance and red lines.

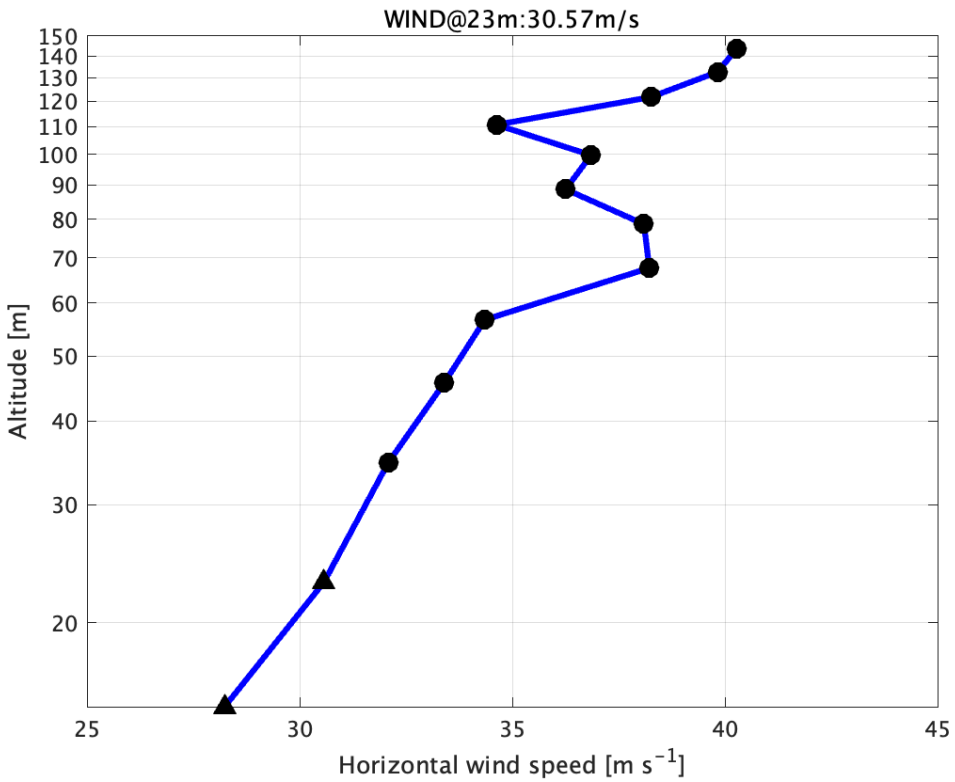

Figure 4.23: Relationship between wind speed and altitude in semi-logarithmic graph. - Circle shows averaged wind speed estimated from radar observation and triangle shows 10-minutes averaged wind speed estimated from wind anemometer.

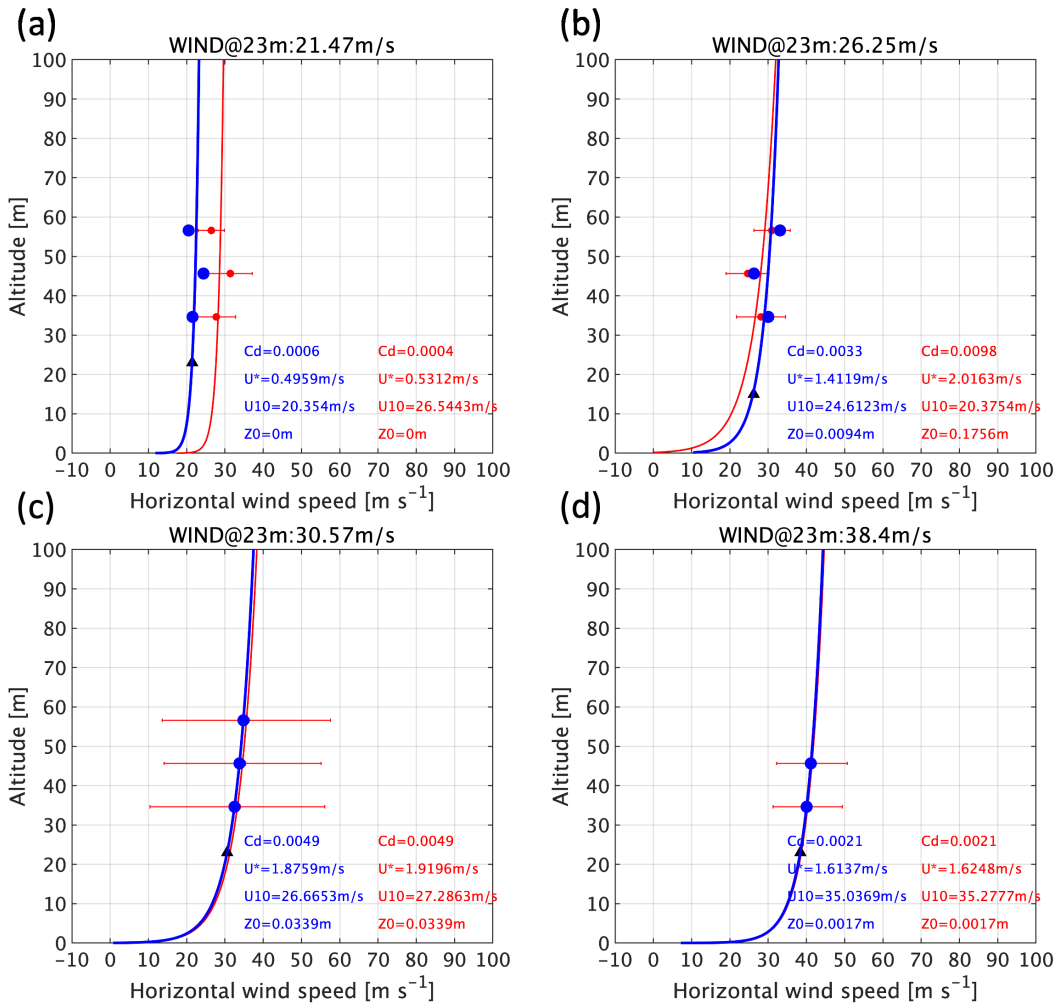

Figure 4.24: Profiles of horizontal wind speeds. - (a) 10-minute averaged wind speed at 23 m height is from 20 to 25 ms^{-1}, (b) 25 to 30 ms^{-1}, (c) 30 to 35 ms^{-1}, (d) 35 to 40 ms^{-1}. Red dot is estimated from Hovmöller diagram with standard deviation. Red line is a fitting curve for red dots. Black triangle shows 10-minute averaged wind speed at 23 m height. Blue dot is modified wind speed calculated from multiplying the ration in Step 12 and red dots. Blue line is a fitting curve for blue dots. Red/Blue color sentences are for red/blue fitting curves, respectively.

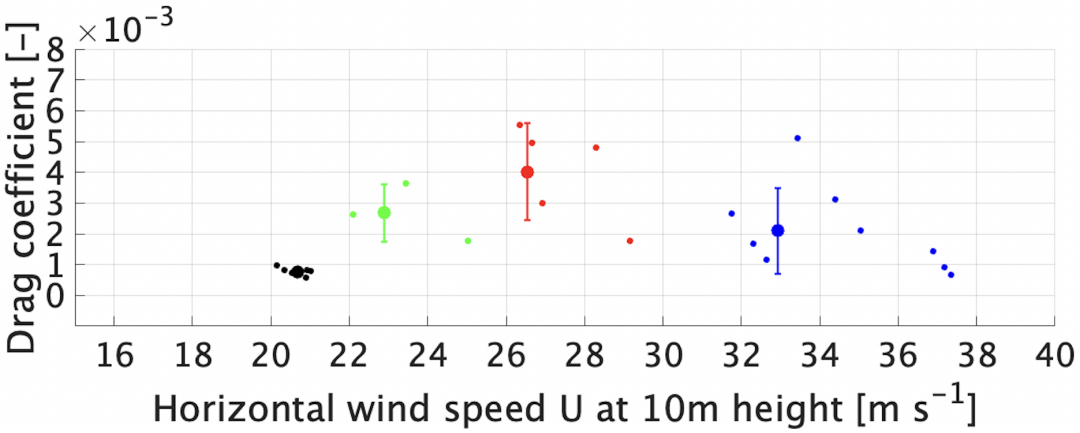

Figure 4.25: Relationship between horizontal wind speed at 10 m height and drag coefficient. - Small dots shows 12 patterns: 3 patterns (Step 7 a, b, c) × 4 patterns (Step 14 a, b, c) in the flow chart. Bigger dots is mean value of 12 patterns and bar shows standard deviation. Black dot is estimated from the group with wind speed at 20 to 25 ms^{-1}. Green dot is estimated from the group with wind speed at 25 to 30 ms^{-1}. Red dot is estimated from the group with wind speed at 30 to 35 ms^{-1}. Blue dot is estimated from the group with wind speed at 35 to 40 ms^{-1}.

5

Estimation method of concentration from normalized radar cross section

5.1 Introduction

As mentioned in the previous section, the principle of radar observation is based on the scattering theory of electromagnetic waves. The scattering of electromagnetic waves depends on the relative refractive index, relationship between particle size and wave length, and shape of the material. Electromagnetic waves are referred to by different names depending on their wavelength. The wavelength range generally referred to as radio waves such as several millimeters to 1 km, Infrared rays range from 1 μm to 10 μm, electromagnetic wave visible to the human eye ranges from 360 nm to 700 nm, ultraviolet rays range from 10 nm to 360 nm, and radiation ranges from 10 pm to 10 nm. An electromagnetic wave visible to the human eye is generally called light. The reason behind the sky changes color from blue to orange during sunset is because visible light is scattered by aerosols in the atmosphere. The blue color of the sky is important, when considering the scattering of electromagnetic waves. A very known and the most influential scientist of the 20th century Albert Einstein also considered this problem. As blue

light have a shorter wavelength than the other visible light. Therefore, it is more easily scattered by aerosols than red light. During the daytime, when the sun reaches to a higher altitude, the shorter, high energy blue wavelength of sunlight gets very well scattered by aerosols and reaches to our eyes. At dawn and dusk, when the sun's altitude is low, the blue light is scattered but reduced because it travels a relatively long distance before reaching to our eyes, and the remaining red light reaches to our eyes. Therefore, the sky is red at dawn and dusk, and blue during the day. This scattering known as Rayleigh scattering, named after Sir Lord Rayleigh of England. Rayleigh scattering occurs when the size of the particles is small compared to the wavelength. Clouds, on the other hand, are white in color. This is because the size of cloud water particles is larger than that of aerosols, and thus the scattering of visible light is different from Rayleigh scattering. The scattering of visible light on cloud water is called Mie scattering, named after Gustav Mie of Germany. Mie scattering occurs when the wavelength is equal to the particle size, and another scattering called geometric scattering occurs when the particle size is even larger than the wavelength.

Rayleigh scattering and Mie scattering represent scattering of electromagnetic waves by a single spherical particle. As mentioned above, the difference between Rayleigh scattering and Mie scattering is the size of the particle with respect to the wavelength, but both can be expressed using Mie scattering theory when expressed in a mathematic form. In this section, we introduce the mathematic expression of Mie scattering. Mie scattering contains some dominant parameters: particle diameter, wavelength, and relative refractivity. The diameter is from 0.001 to several mm, equivalent to sea spray and rain droplets. In our observations, X-band radar whose wavelength is 3 cm used. However, the Mie theory can be applied for small particles such as cloud water and aerosols. In this study, sea spray and rain were the targets of X-band radar observation. Therefore, the scattering of X-band radar by rain is represented by Rayleigh scattering. However, the size of sea spray ranges widely from 0.001 to 1 mm. This range is equivalent to cloud water. For the first analysis in this chapter, we investigated the change of scattering due to the particle size.

The governing parameter for scattering is relative refractivity which varies

due to salinity. A previous study suggested a theory of refractive indices of water containing salt, comparing the theory against experimental results (2). The proposed equation is based on the Lorents-Lorenz and Clausius-Mossotti equations, which indicate the dielectric constant or refractive indices of polarizable molecules. In 1986, the Danish physicist and mathematician Ludwing Lorentz derived the equation from the theory of elasticity. In 1878, the Dutch physicist Hundrik Lorentz formed their equation from the standpoint of electromagnetism in a vacuum and in matter. Lorentz chaired a committee to predict the impact of the *Afsluitdijk* at the request of the Dutch government. In this Chapter, relative refractivity for X-band radar is obtained from the .

For the next step, we must consider scatterings by several particles, because our targets are a tall cloud of drops. The concepts of single scattering and multiple scattering are considered. In the former scattering, an electro-magnetic wave is hit by a particle and returns to the observation site without further scattering by the other particles in the unit volume. Alternatively, the multiple scattering involves iterative scattering by particles in the unit volume. This is a type of Rayleigh or Mie scattering for unit volume and is generally called volume scattering. The threshold between them is qualitatively the relationship between the wavelength and distance of particles. Usually, rain observation can be treated as single scattering because the density of particles is enough low. For sea spray, Dombrobsky and Ballis (2010)(44) explained an algorithm for scattering by sea spray packed into a unit volume which is based on single scattering. Victor (2011, 2013) (65), (66) show the applicability of this algorithm for radar observations rotating horizontally and detecting the sea surface. Thus, in this study, volume scattering is treated as single scattering. The methodology to represent the radar cross section with an equation for number of drops in unit volume is applied for this study. Here the proposed method, using the algorithm and estimated normalized radar cross section enables us to estimate concentration of sea spray from radar observation. Finally, the mass concentration profile of sea spray is calculated and relationship between wind speed and mass concentration at certain height were investigated.

5.2 Mie scattering and Rayleigh scattering

In this section, scattering is investigated in terms of the refractive index, size parameters, and number of terms in **Eq**.(7.20). The Mie theory is derived in Appendix 7.1. First, the refractive index was investigated. **Figure 5.1** shows the refractive index of water against the wavelength based on a prior experiment. This is cited from the M.S. Thesis of D. Segelstein, "The Complex Refractive Index of Water", University of Missouri-Kansas City, (1981). The blue line shows the real number and orange line shows the imaginary number. The vertical red line is the wavelength at 3 cm, equivalent to the X-band radar. The refractive index of water against 3 cm is 8.07-1.82i. It should be noted that refractive indices vary with wavelength. For the salinity of water, the refractive indices are 9.82–5.06i. This value is for 3 % salinity water.

The next step was to consider the diameter of raindrops and sea spray. The analysis was performed assuming raindrops and sea spray, respectively. The size of raindrops is approximately 0.1 to several millimeters. Conversely, drop ranges from 0.001 mm to 1 mm. The wavelength of the radar observation was 3 cm because it was an X-band radar. The relative refractive index, which is important when considering the scattering of electromagnetic waves, was 6+i (personal communication with Victor Raizer). First, we considered the variation of the backscattering cross section in the presence of a single spherical particle. The backscattering cross section is defined as the backscattering efficiency factor multiplied by the area. The relationship between backscattering cross section and diameter is shown in **Figure 5.2**. The figure shows that the backscattering radar cross section increased monotonically with particle size up to approximately 5 mm in diameter. However, it did not increase monotonically from 5 to 10 mm in diameter. As the particle size increased, the value oscillated and the amplitude gradually decayed. This is a difference between Rayleigh scattering and Mie scattering. When considering rainfall and droplets, Rayleigh scattering should be applied. Note that Rayleigh scattering is an approximate solution of Mie scattering, as derived in Appendix 7.1, and is based on the Mie scattering principle.

The next investigation was the difference in Mie and Rayleigh scattering. For the Mie scattering theory, the number of waves scattered by particle was

calculated following the function of the size parameter:

$$N_{max} = floor(x + 4.05x^{1/3} + 2) + 1. \tag{5.1}$$

Here, N_{max} shows the number of terms. This number is related to how many waves are composed in calculation. The scattering wave consists of composed waves. **Figure 5.3** shows the relationship between the size parameter and the number of terms. For the range of diameters of rain and sea spray, number of terms varies from 4 to 8. To investigate Rayleigh scattering, the number of terms was set as 3. To define Rayleigh scattering, in the aspect of phenomenology, the wavelength is almost the same as the radius, that is, the size parameter is less than 1. When the size parameter is less than 1, the number of terms is less than 8. This was the same case for rain and sea spray. The calculation result is shown in **Figure 5.4**, when the number of terms was set based on **Eq**.(5.1). These figures show phase function of scattering wave, and the angle shows propagating angle of scattering wave. (a-1) shows propagating angle and ratio of scattering wave by single particle. (a-2) shows the same as (a-1) but the coordinate system is cartesian coordinate. The particle diameters of 0.1, 0.01, 1, and 5 mm are in (a), (b), (c), and (d), respectively. The relative refractivity was set as 8.07-1.82i. For (a), (b), and (c), the scattering direction and radiance were relatively similar. However, for (d), a small difference was noted: forward scattering was bigger than backscattering. In **Figure 5.5**, the number of terms is set to 3. The characteristics are the same as those in **Figure 5.4** between cases (a) $\sim$ (d). Comparing these results with **Figure 5.3**, **Figure 5.3** (a), (b), (c) and **Figure 5.4** (a), (b), (c) are same as each other. However, comparing **Figure 5.3** (d) with **Figure 5.4** (d), forward scattering of **Figure 5.3** (d) was stronger than that of **Figure 5.4** (d). From this analysis, the Mie theory can be applied for rain and sea spray.

5.3 Single scattering for volume scattering

In this section, we describe a method to represent scattering by multiple particles using the backscattering cross section derived in the previous section.

5. ESTIMATION METHOD OF CONCENTRATION FROM NORMALIZED RADAR CROSS SECTION

When considering scattering by multiple particles, if we can assume that the distance between the particles is sufficiently large compared to the wavelength of the electromagnetic wave, the scattering by the group of particles can be treated as a single scattering. Conversely, if the distance between the particles is small, multiple scattering must be considered.

The distance between each particle was calculated based on previous drop size distributions of rain and sea spray assuming the following two conditions. To investigate that, the first assumption is that all particles are distributed uniformly and the structure is a hexagonal close-packed structure. The second assumption is that particles are spherical, based on these assumptions, we calculated the radius with the densest situation in the unit volume. For the densest situation, the total volume of all particles was 74 % of the unit volume V. The total number of particles in the unit volume was defined as N; therefore, we obtained the following relationship:

$$0.74V = \frac{4}{3}\pi R^3 \times N, \tag{5.2}$$

Then, solving **Eq.**(5.2) for R,

$$R = \left(\frac{0.74 \times 10^9}{N \times \frac{4}{3}\pi}\right)^{\frac{1}{3}}, \tag{5.3}$$

This shows the distance between the centers of particles. For rain, the total number of particles is

$$N = \int_{D_{min}}^{D_{max}} N_0 \exp\left(-\lambda D\right) dD.$$

For example, when rainfall intensity is 5 mmh^{-1}, assuming that D_{min} and D_{max} are 0.1 and 5, and $\lambda = 4.1 \times 5^{-0.21}$, $N_0 = 8 \times 10^3$, then the total number is 2.04×10^3. In addition, using **Eq.**(5.3), the distance between centers is 44.2 mm. The representative diameter of rain D_{ave} for rainfall intensity 5 mmh^{-1} can be calculated using the following equation:

$$D_{ave} = \frac{\int_{0.1}^{5} D \times N_0 \exp\left(-\lambda D\right) dD}{\int_{0.1}^{5} N_0 \exp\left(-\lambda D\right) dD} = 0.44. \tag{5.4}$$

Figure 5.6 shows relationship between rainfall intensity and averaged distance calculated by **Eq.**(5.4). The distance decreases with increase of rainfall intensity. The distance drastically decreases up to 20 mmh^{-1}, and reaches about 34 mm. Even the rainfall intensity is 100 mmh^{-1}, the distance is more than 30 mm equivalent to the wavelength of X-band radar.

Figure 5.7 shows the same as **Figure 5.6** but with drop size distribution defined as **Eq.**(3.3). The parameter μ varies from 0 to 10. When parameter is smaller, the number of smaller drops relatively increase. Thus, the blue color is equivalent to $\mu = 0$. When rainfall intensity is less than 20 mmh^{-1}, the distance between each particle widely spread from 40 to 120 mm. However, the distance becomes approximately 30 to 40 mm for all μ, as rainfall intensity becomes 100 mmh^{-1}. From this investigation, the single scattering algorithm can be applied for rain drops packed into unit volume.

5.4 Normalized radar cross section of backscattering

In this section, a normalized radar cross section of backscattering was obtained from an algorithm based on the Mie theory. As shown in the previous section, our observation targets, sea spray and rain, can be expressed in terms of single scattering. Here, we applied the method proposed by Dombrobsky and Ballians (2010) (44) to derive the normalized radar cross section, accounting for the drop size distribution. This method has been applied to the observations of the sea surface by horizontal radar using Victor (2012, 2013) (65) and (66). In this study, we estimated the parameters contained in the drop size distribution by comparing the normalized radar cross section obtained by the same algorithm including drop size distribution with that obtained in Chapter 4. This proposed algorithm makes it possible to estimate the drop size distribution from radar observations. The backscattering efficiency Q_b [-] derived based on the Mie

scattering principle is as follows.

$$Q_b = \frac{1}{x^2}\left|\sum_{n=1}^{\infty}(2n+1)(-1)^n(a_n - b_n)\right|^2,$$

Here, a_n and b_n are scattering coefficients, and are described as follows.

$$a_n = \frac{m^2 j_n(mx)[xj_n(x)]' - j_n(x)[mxj_n(mx)]'}{m^2 j_n(mx)[xh_n^{(1)}(x)]' - h_n^{(1)}(x)[mxj_n(mx)]'},$$
$$b_n = \frac{j_n(mx)[xj_n(x)]' - j_n(x)[mxj_n(mx)]'}{j_n(mx)[xh_n^{(1)}(x)]' - h_n^{(1)}(x)[mxj_n(mx)]'}.$$

j_n is the Bessel function, h_n is the Hankel function, m is the relative refractivity, and x is the size parameter. The relationship between backscattering efficiency and RCS is

$$\sigma_b = Q_b \pi \left(\frac{D}{2}\right)^2,$$

Here, D is the diameter of the sphere. These equations are a general scattering theory for a single spherical particle. To describe the volume scattering, which we consider here as scattering from many particles with several diameters following a drop size distribution in a unit volume, the following equations were used(65)(66)

$$\begin{aligned}
\sigma_b &= 0.75\frac{C}{a_{30}}\int_0^{\infty} Q_b a^2 N(D)dD, \\
C &= \frac{4\pi}{3}N_0\int_0^{\infty} D^3 F(D)dD, \\
a_{30} &= \frac{\int_0^{\infty} D^3 N(D)dD}{\int_0^{\infty} N(D)dD}, \\
N(D) &= \frac{A^{B+1}}{\Gamma(B+1)D^B \exp(-AD)}.
\end{aligned} \tag{5.5}$$

Here, N_0 is the number of particles in the unit volume [cm^{-3}]. The first equation means integration of scattering by all particles in unit volume. The second equation means total volume of particles and the last is average volume weighted by number of drops in each size. This enables us to represent radar observation results obtained in Chapter 4. In a previous study, the particle size distribution $N(D)$ was assumed to be gamma-distributed, and the radar cross section by Mie

scattering was derived considering the volume scattering when multiple particles exist in a unit volume. In this study, we assumed that this $N(D)$ is the drop size distribution where raindrops and sea spray are mixed and estimated the drop size distribution by determining the parameter that fits the normalized cross section obtained from the observation. In **Figure 5.8**, the normalized radar cross section of a single particle and volume scattering are shows. **Figure 5.8** (a) has the single peak, this monotonic increase is the characteristics of Rayleigh scattering. In **Figure 5.8** (b), several cases are presented with different parameters. Interestingly, all cases have single peak and the characteristics of Rayleigh scattering. When two parameters are set, the number of particles in unit volume is determined. In this Chapter, the two parameters are estimated with two different conditions. One is the normalized radar cross section obtained in Chapter 4 and another is the conservation of the profile shape.

Figure 5.9 shows flow chart for estimate number of drops and mass density for each height from normalized radar cross section obtained in Chapter 4. The whole processes consist of 13 steps. The obtained data in Chapter 4 is used and calculate spatial average from the region near the observational tower because meteorological datasets are used in this analysis. The averaged data is obtained with the horizontal 300 m width (from 1550 to 1700 m to from 1900 m to 2050 m) and vertical each 2.2-m height in Step 2. From Step 3 to Step 8, estimate of two parameters in the fourth of **Eq**.(5.5). The parameter A and B varies from 1 to 400 and from 1 to 5, respectively. We calculate all cases and, the minimum value of the subtract between normalized radar cross section and it was estimated with **Eq**.(5.5) and that it obtained in Chapter 4. In Step 6, parameter A and B for each height are selected and multiple choice are allowed. In Step 7, with these parameters A and B, mass density for each height is calculated. These processes are iteratively calculated with height from 0 to 2700 m. After iterative calculation, the continuity of vertical distribution of mass density is used to exclude the parameter set. Finally single set of parameter for each height has been decided in Step 8. In Step 10, whole data is classified into two groups. One is, when it was rainy and another is with no-rainfall time. In Step 11.a, mass density profiles are drawn and mass density at 30-m height is extracted. These profiles are mass density of sea spray because there are no rainfall. These profiles and

mass densities are classified into each horizontal wind speed. In Step 11.b, mass density profiles are dawn. Since the mass density of rain should be considered in this Step, we subtract mass density at 100 as rain at each height from 30 to 100 m. Then, mass density profiles of sea spray are drawn. Finally, we obtained mass density profiles and mass density at 30-m height. In Step 13.a and b, we apply the exponential curve following equation for mass concentration profiles from 30 to 100 m height. We exclude below 30 m height which contains sea clutter.

$$c(z) = c_0 \exp(-\alpha z) \tag{5.6}$$

All steps are conducted and drop size distribution and mass concentration of sea spray are estimated. Furthermore, relationship between wind speed and profiles and mass density are investigated.

5.5 Results

In the first step, no-rainfall data used by the X-MP radar at Katsuragi station. Furthermore, the analysis with rainfall estimated by the X-MP radar is shown later. The normalized radar cross section from the ship observations was obtained and spatial averaged result is shown in **Figure 5.10** (left panel). This figure shows that the distribution is almost constant at a height from 100 to 1000 m. From the results, we can assume that these characteristics of rainfall is uniformly distributed in Step 12. At the surface, the maximum value increased with wind speed at 23 m height. **Figure 5.10** (right panel) shows the estimated results. The estimate completely represent the profile of normalized radar cross section. **Figure 5.11** shows mass density profiles when it is no-rainfall. The color bar shows the 10-minutes averaged wind speed at the tower. The lower area approximately up to 30-m heigh contained sea clutter. Thus, the results of comparing the normalized cross section of the sea clutter calculated in the previous chapter are shown in **Figure 5.12** (a). For the maximum wind speed when it is no-rainfall, the maximum wave height was 10 m. Therefore, assuming the lowest height is 10 m, the maximum height reached by sea clutter is 20 m, as shown by black crosses in **Figure 5.12** (a). Additionally, the averaged diameter

D_{ave} was calculated using the estimated drop size distribution. The diameter is described as

$$D_{ave} = \frac{\int_{d_{min}}^{d_{max}} D \times N(D) dD}{\int_{d_{min}}^{d_{max}} N(D) dD}.$$

Here, d_{min} and d_{max} are 0.001 to 5 mm, respectively. $N(D)$ is the drop size distribution defined in **Eq**.(5.5). The results are shown in **Figure 5.12** (b). The vertical axis shows the normalized cross section at the height from 20 to 40 m. The diameter became smaller as the height increased. This is because drops from rain are a constant diameter while the drops from sea spray become smaller with height. A diameter of 0.04∼0.08 cm was distributed at heights from 20 to 40 m.

Figure 5.13 shows mass density profiles of sea spray at wind speeds from 20 to 30 ms^{-1} when it is no-rainfall. The red dots show the profile of maximum wind speed was 27.4 ms^{-1} without rainfall. The blue dots show the profile when wind speed was from 15 to 20 m^{-1}. The red and blue lines are fitting curves with **Eq**.(5.6). The equation is applied for these profiles, however fitting range is different, it is because the boundary layer height of mass density is different. The boundary layer height increases with wind speed increases. In the case of the maximum wind speed, the equation is applied for the range of height from 30 to 80 m. If the wind speed is from 15 to 20 ms^{-1}, the range of height from 20 to 60 m is applied. Fitting curves enable us to obtain mass density of sea spray on the sea surface, although It is difficult to observe the sea surface area since sea clutter contaminates into radar observation.

Figure 5.14 shows mass density profiles of sea spray at wind speeds from 25 to 40 ms^{-1} during rainfall. Color shows 10-minutes averaged wind speed at the observational tower and dots are calculated results. Other lines are fitting curves based on **Eq**.(5.6). The methodologies are the same but we extract mass density of rain at 100-m height from the each height because the profiles above 100m are uniformly distributed. The mass densities at height from 20 to 100 m increase with wind speeds. We applied **Eq**.(5.6) for all cases. The range of height for fitting curve is from 30 to 100 m. The strongest wind speed is 38.2 ms^{-1} and the second strongest is 37.3 ms^{-1}.

Figure 5.15 shows relationship between 10-minutes averaged wind speed

and mass density at 20-m height extracted from profiles in **Figure 5.13, 5.14**. Blue dots are mass density at 20-m height. The dashed line shows fitting curve. The mass density increases exponentially with wind speed.

5.6 Summary and conclusions

In this chapter, the drop size distributions of sea spray were estimated from the normalized radar cross section. The normalized backscattering radar cross section indicated that strong radiance from the scatterer radiated in a backward direction. This physical quantity is significantly important for radar observation. If this quantity is calculated for a target medium, radar observation can be applied.

In this study, the target scatterers were rain and sea spray. The first analysis in this chapter revealed whether single scattering and multiple scattering was suitable for these targets. Assuming their previous drop size distributions, the average distance of particles was calculated. Then, the distance was almost the same as the wavelength of the X-band radar used in this study. Thus, we applied the single scattering theorem for both rain and sea spray.

The second analysis was estimate of concentration and mass density of sea spray. The applied algorithm was proposed by Dombrobsky and Billian (2010)(44). This methodology is based on the Mie theory for each particle with various diameters, integrating all radius and multiple drop size distributions. In this study, assuming the drop size distribution having two parameters, a normalized backscattering radar cross section was calculated by the algorithm. Since this result should match the observation result in Chapter 4, when the ship radar detected rain and sea spray, the two parameters in the drop size distribution had another condition, it is "the vertical profile of mass density is continuous". The drop size distribution was estimated in both cases without rainfall and with rainfall. The maximum wind speed at each 10 minute at 23 m height is 38.2 ms^{-1}. In the same event, typhoon JEBI, the record maximum wind speed was observed at Nanki-Shirahama AMeDAS station from 2006 to 2020. From this investigation, profiles of mass density and drop size distribution are finally obtained

under severe wind conditions by radar observation. And these are represented by exponential curve which is the same as equation for suspended sediment in river channels. Thus, we can apply the equation for numerical simulations and the observation results are useful for validation of numerical simulations. These information can lead to further understanding the multi-interactions between the air and sea, and improvement of numerical simulations.

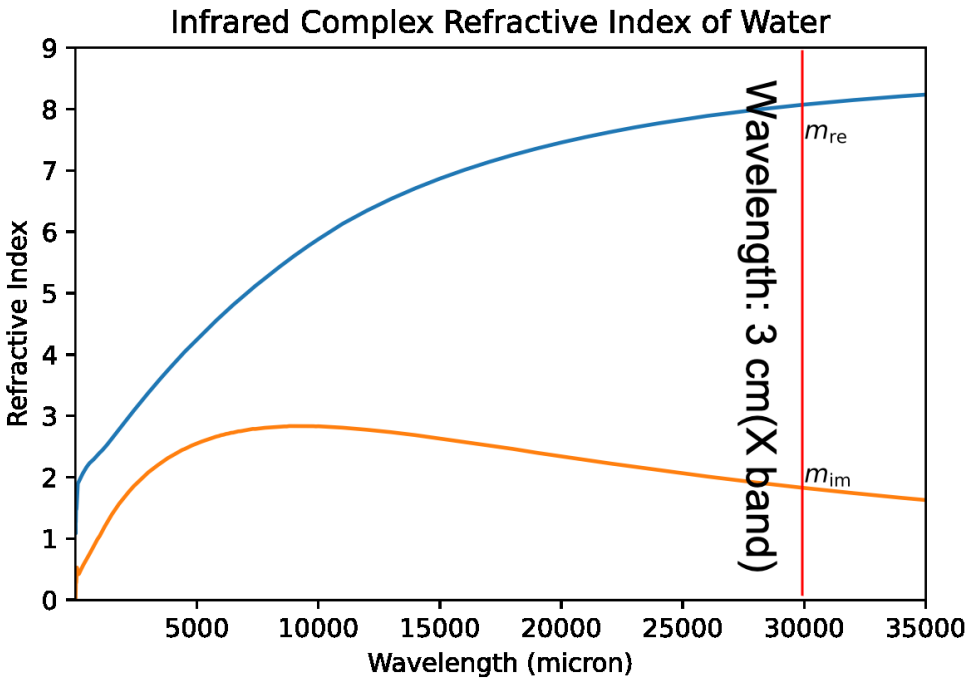

Figure 5.1: Complex refractive index of water - The vertical red line shows that the wavelength is equal to 3 cm (X-band radar).

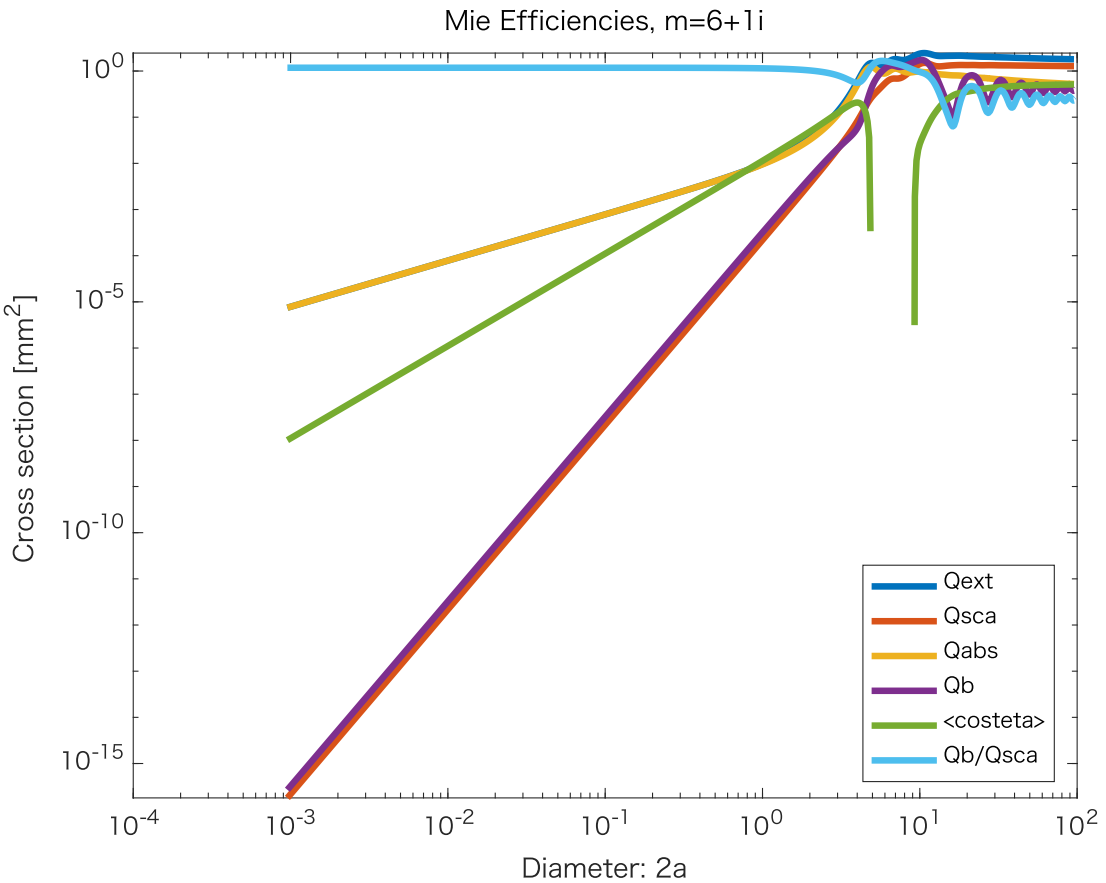

Figure 5.2: Relationship between particle size and the radar cross section. - The relative permittivity is shown for the case of 6+i, which is equivalent to salt water. This indicates the extinction, scattering, absorption, and backscattering cross sections.

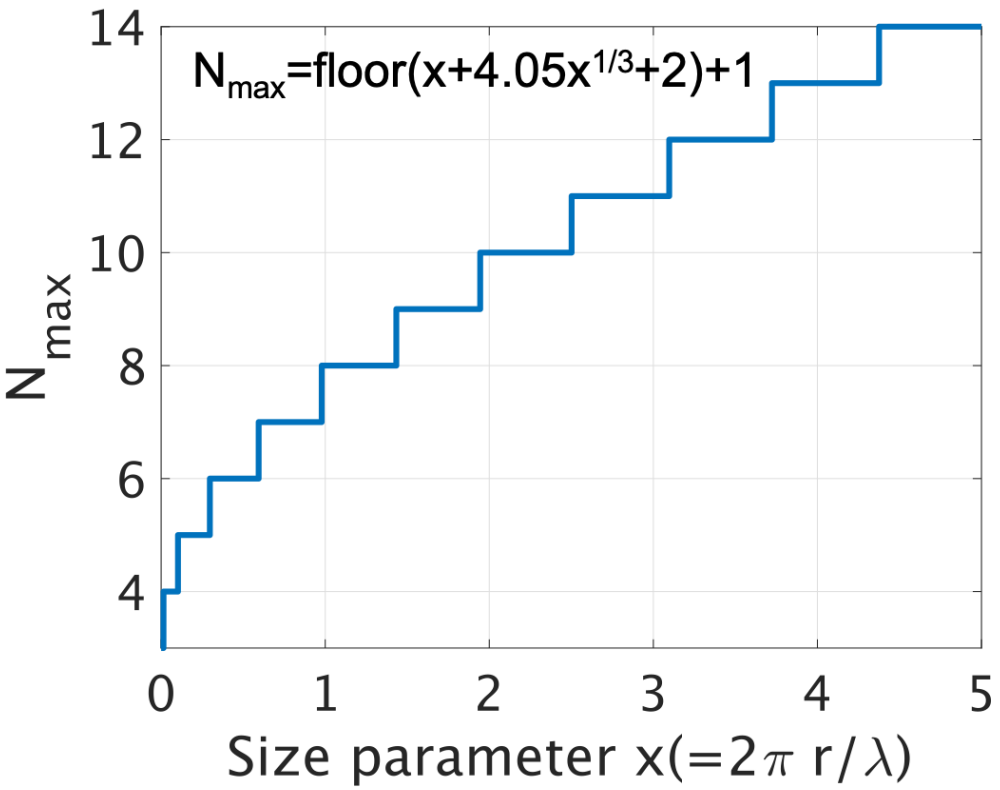

Figure 5.3: Size parameter and number of terms in the Mie theory.

- The number of terms is based on the equation in this figure.

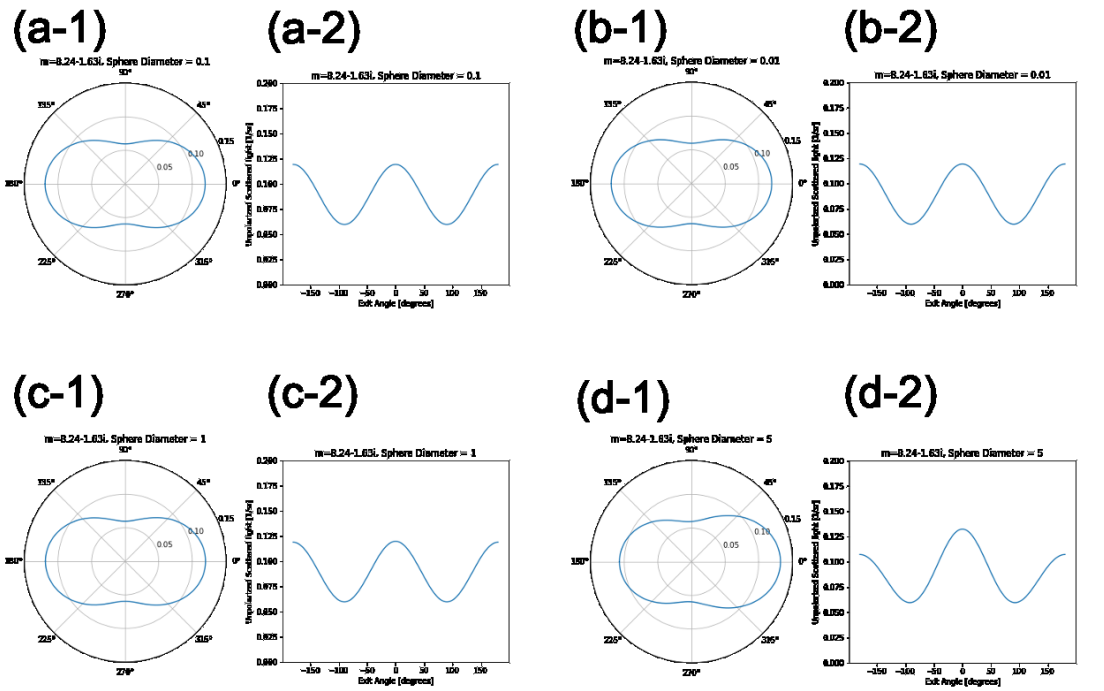

Figure 5.4: Scattering direction and radiance in several cases based on the Mie theory - (a) Diameter: 0.01 mm, Relative refractivity: 8.07–1.82 i. (b) Diameter: 0.1 mm, Relative refractivity: 8.07–1.82 i. (c) Diameter: 1 mm, Relative refractivity: 8.07–1.82 i. (d) Diameter: 5 mm, Relative refractivity: 8.07–1.82 i.

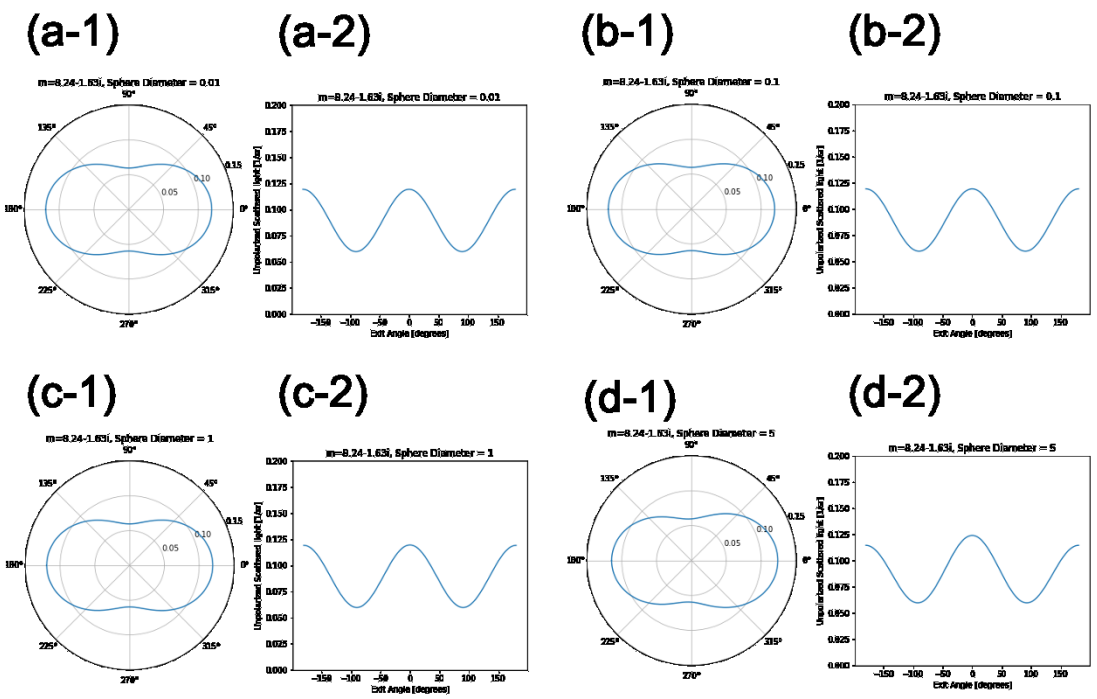

Figure 5.5: Same as Figure 5.4, but with the Rayleigh theory (number of terms is 3). - (a) Diameter: 0.01 mm, Relative refractivity: 8.07–1.82 i. (b) Diameter: 0.1 mm, Relative refractivity: 8.07–1.82 i. (c) Diameter: 1 mm, Relative refractivity: 8.07–1.82 i. (d) Diameter: 5 mm, Relative refractivity: 8.07–1.82 i.

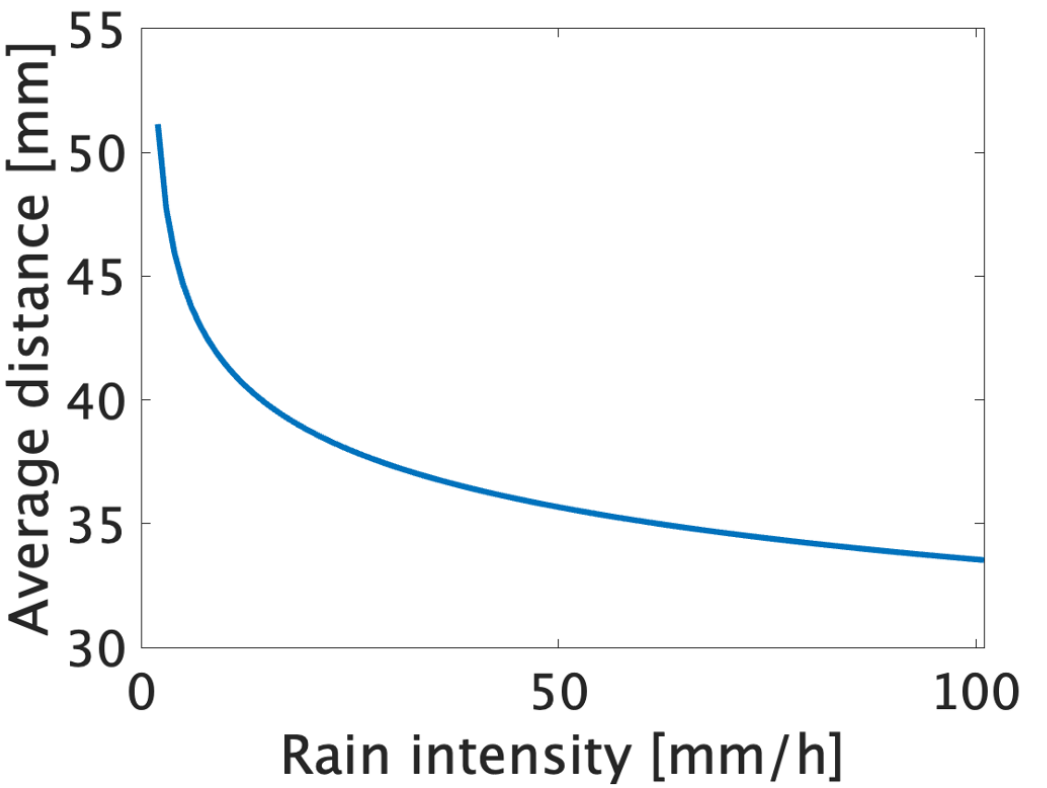

Figure 5.6: Relationship between rainfall intensity and average particle distance. - It is assumed that the drop size distribution is Marshall and Palmer equation.

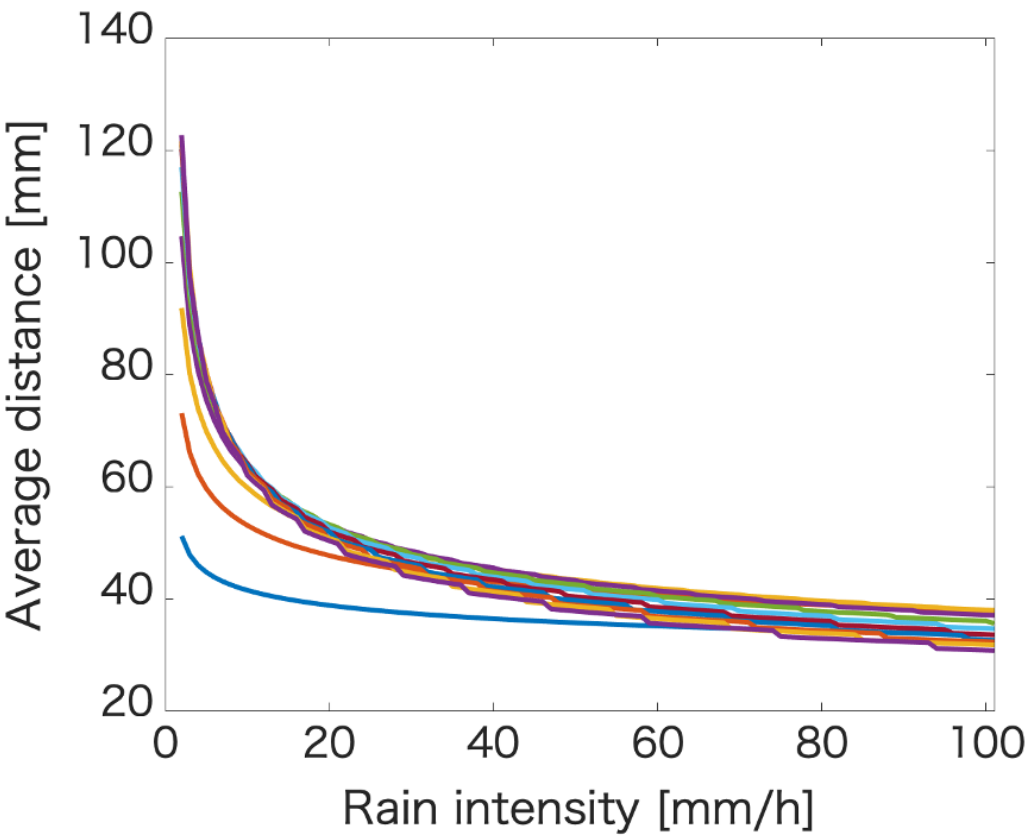

Figure 5.7: - Same as **Figure 5.6**, but assuming the Ulbrich equation.

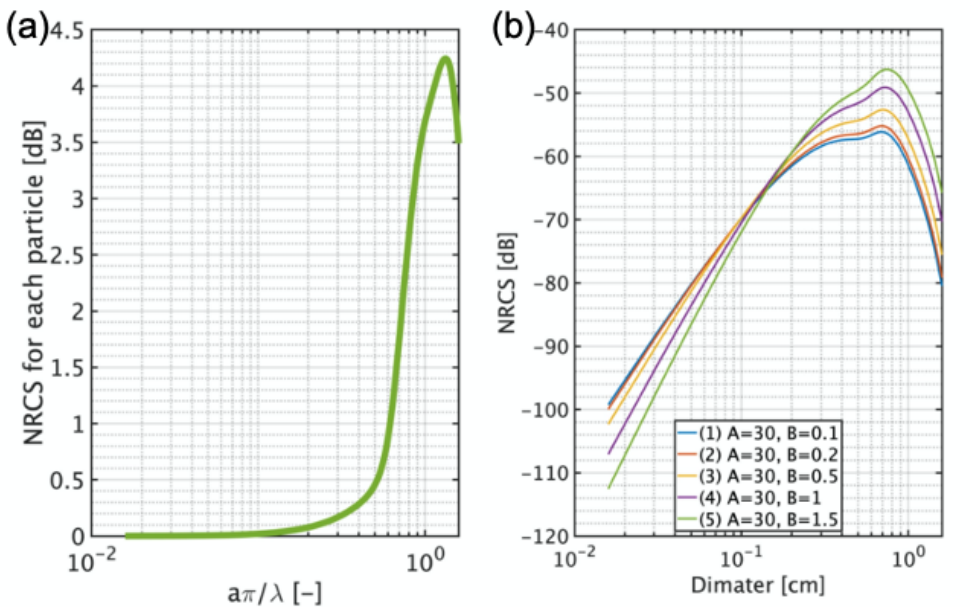

Figure 5.8: Distribution diagram of NRCS for each particle size. - (a) NRCS for a single particle. (b) Distribution of NRCS for a particle size distribution, assuming an arbitrary particle size distribution. The legend shows the two parameters of the particle size distribution.

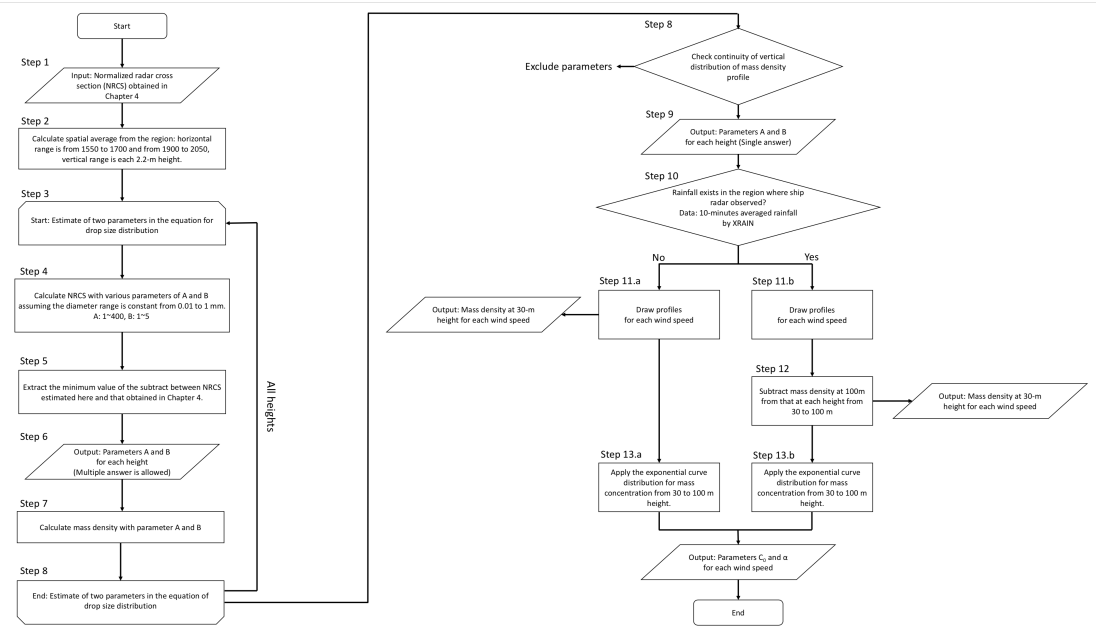

Figure 5.9: Flow chart for estimate profiles of number of particle and mass density. - Whole processes consist of 13 steps.

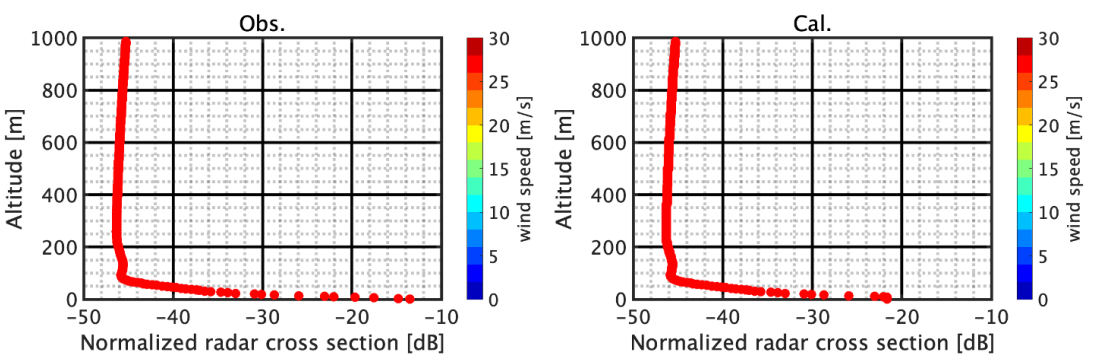

Figure 5.10: One example of a calculation to estimate the parameters in drop size distribution. - Left panel shows one result in Chapter 4. Right panel shows the calculation result.

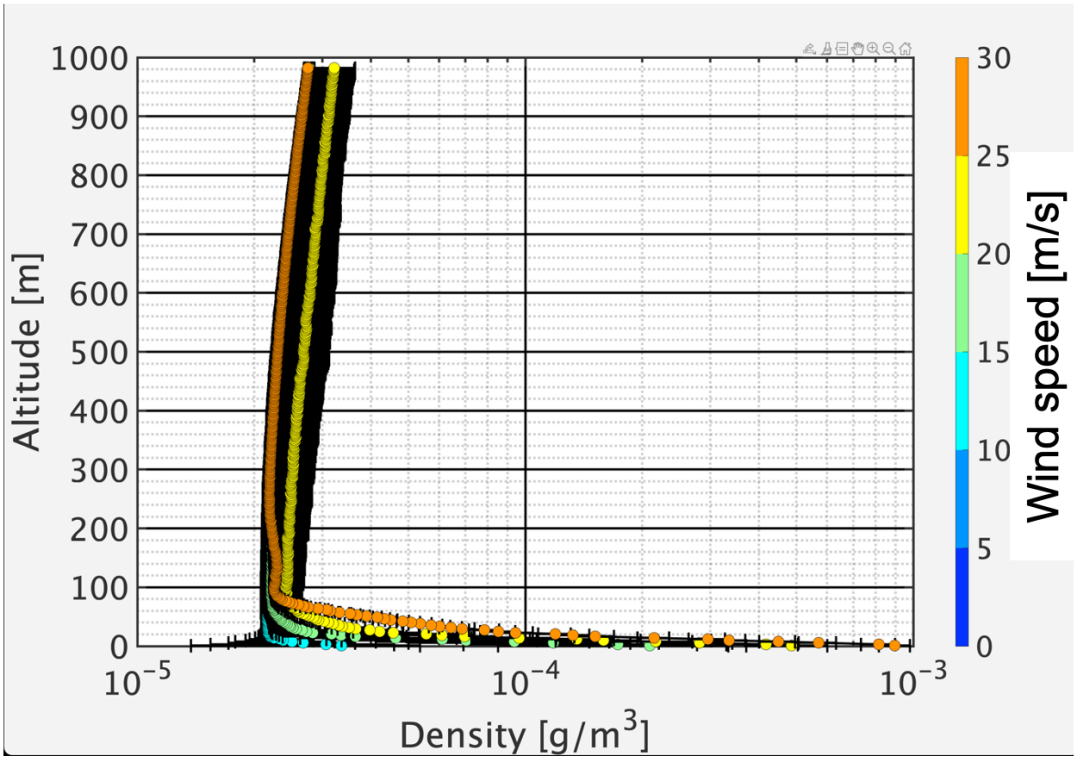

Figure 5.11: Vertical profile of density for each wind speed. -

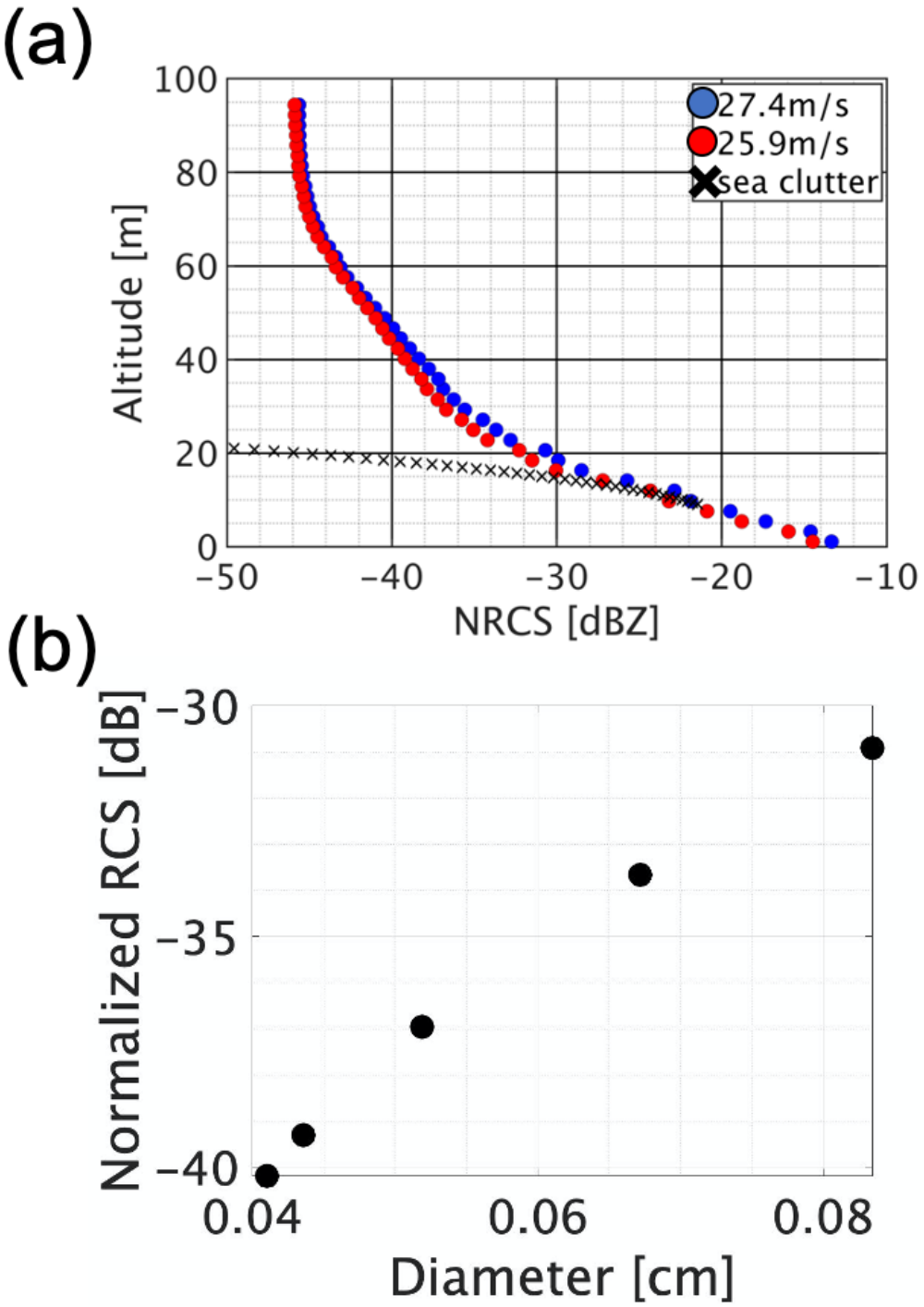

Figure 5.12: Profiles when wind speed is 27.4 and 25.9 ms^{-1} without rainfall and averaged diameter. - (a) Vertical profiles of NRCS obtained from ship radar observations at wind speeds of 25 and 27 ms−1 are shown with circles, and NRCS of sea clutter is shown with crosses. (b) Representative particle size [cm] with NRCS in the range of -40 to -30 dB.

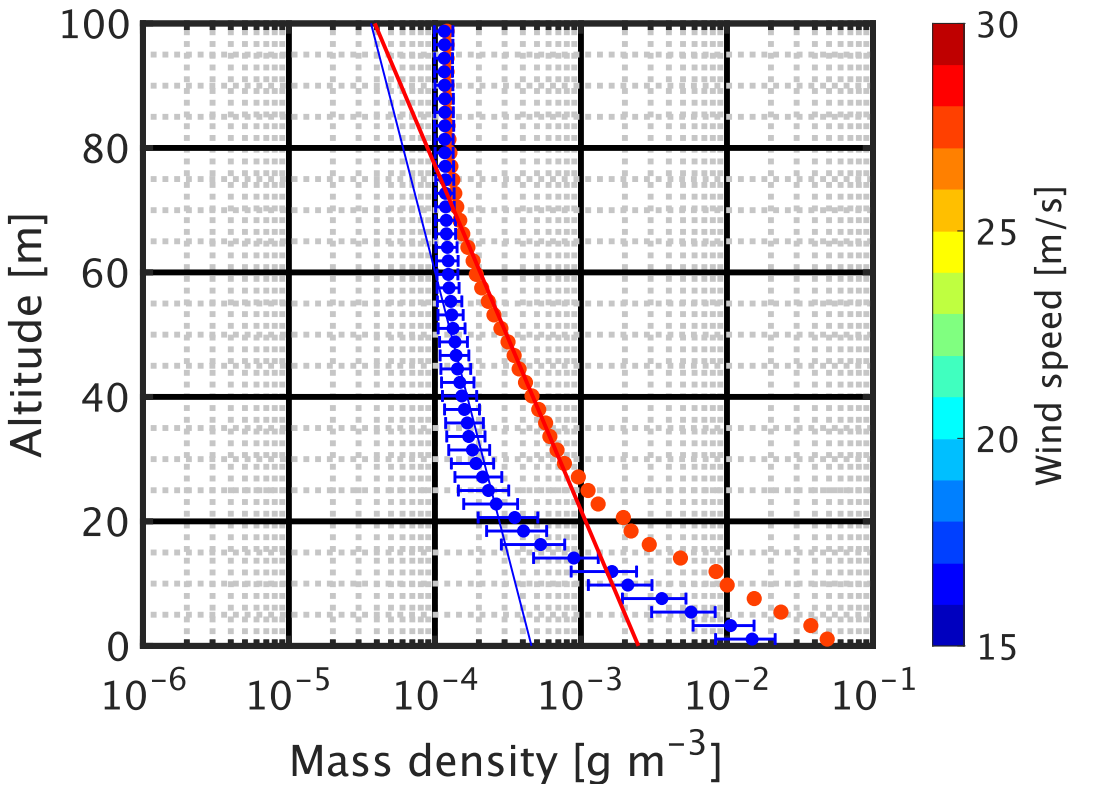

Figure 5.13: Vertical profiles of mass density for each wind speed when it is no rainfall. - Color shows 10-minutes horizontal wind speed. Lines are fitting curves.

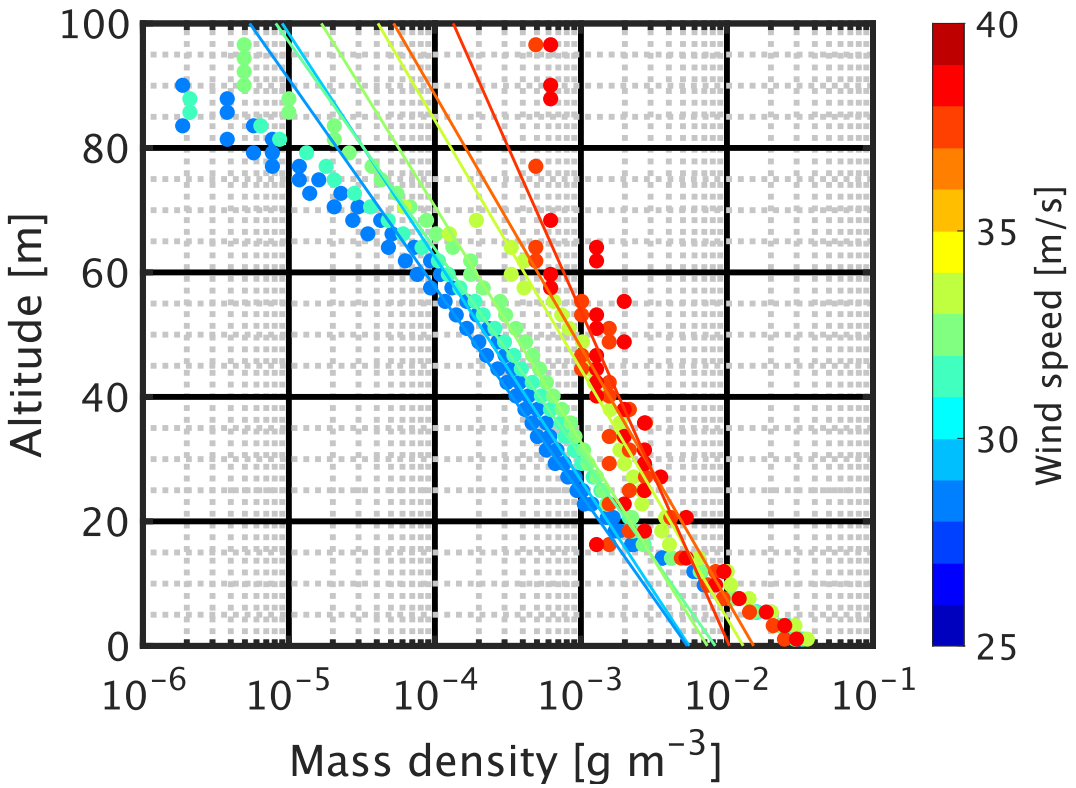

Figure 5.14: Vertical profiles of mass density for each wind speed when it is no rainfall. - Color shows 10-minutes horizontal wind speed. Lines are fitting curves.

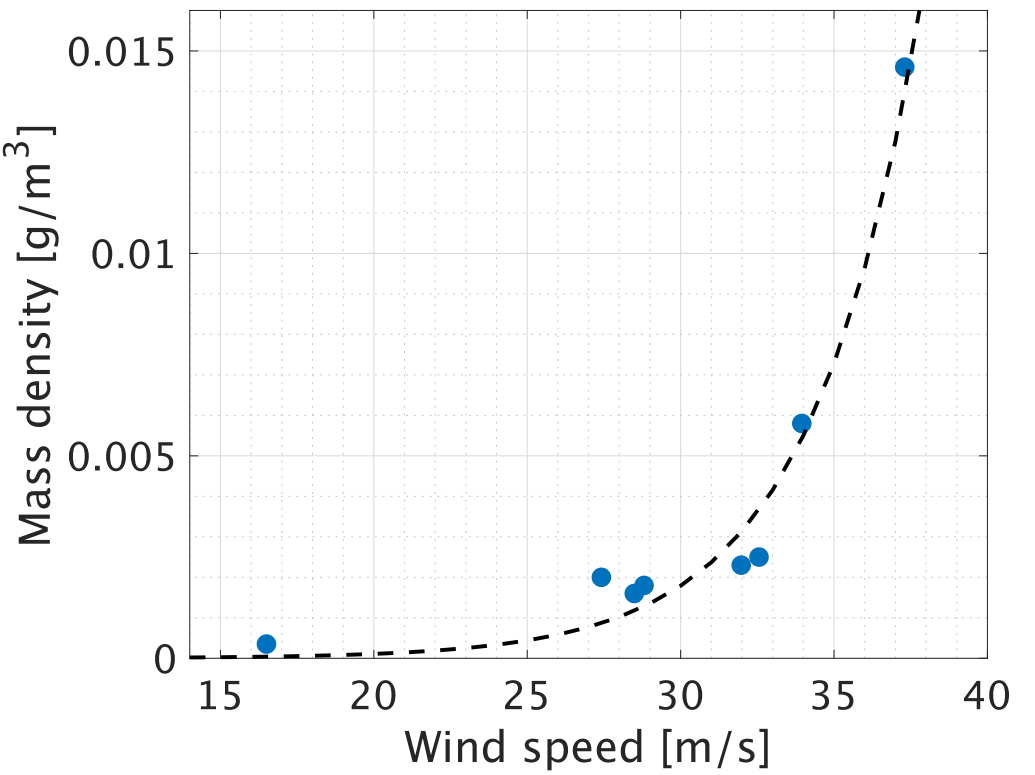

Figure 5.15: Relationship between horizontal wind speed and mass density - Mass densities are extracted from **Figure 5.13**, **5.14** at 20-m height.

6

Summary and Conclusions

6. SUMMARY AND CONCLUSIONS

This thesis summarized the drag coefficient which is an important parameter to express the drag between the air and sea and evaluated roles of sea spray and rain in the surface boundary layer that how the amount of rain and sea spray affected the drag coefficient. Also, this thesis showed the methods to observe sea spray generated from wave breaking under severe wind conditions with disdrometer and ship radar.

First, the author investigated the drag coefficient under strong winds , which is an indicator of friction between the air and sea. The friction is the result of several phenomena: wave breaking, sea spray generation, relationship between wind direction and wave direction, and rainfall. Under strong wind speed conditions like typhoon, the coefficient decreases or is saturated against the increase of wind speed. The author also explored how and to what degree rainfall has an effect on drag coefficient with simple assumptions. The drag coefficient may vary as a result of shear stress of rain drops on the ocean surface. Under high wind speed conditions, the effect of shear stress of rain decreases, on the other hands, under low wind speeds, the effect increases. This investigation shows possibility of effect of rain on the drag. However, the concentration profiles of sea spray which is the fundamental information to understand the situation near surface layer is still unknown, and it it difficult to observe sea spray under storm conditions. Because of that, the purpose of this doctoral thesis is to develop a method for estimating the concentration distribution of sea spray.

In the third chapter, the author conducted field observations at the observation tower of Shirahama Oceanographic Observatory, located 1.8 km off the coast of Wakayama Prefecture, using a disdrometer, anemometer, and wave height meter. Previous studies that detected the drop size distribution of sea spray directly. However, these data have limitations based on their respective situations, such as wind speed and the height of observation. The first observations used a disdrometer because of the robustness and wide range of detected parameters from its diameter. From this observation, the following characteristics were obtained. 1) Observed data at a lower height exhibited a larger amount of sea spray than that observed at a greater height. 2) Sea spray drop size distribution increases with an increase in wind speed. Basically, the disdrometer observed rainfall as well. Thus, two algorithms are established in the chapter. The first

method uses radar-AMeDAS analyzed rainfall data to estimate the time when it was no-rainfall. The second uses the characteristics of drop size distribution for rainfall. Both methods have a robustness because two different methodologies suggested the same characteristics mentioned in (2).

The second set of observations were conducted at the same site using a different observational instrument in Chapter 3. This instrument can detect smaller diameters. Small droplets also increased with an increase in wind speed. These exhibited almost the same rain drop size distribution and sea spray distribution. This means this observation data can be recognized as rain and sea spray: this is an uncertainty of this observation. Of course, if we can detect the salinity of each droplet, these droplets can be classified into both droplets. However, in field observations, it is impossible to detect the salinity of each droplet. Thus, this uncertainty is important in this study. Assuming the obtained data was recognized as sea spray, drop size distributions of sea spray for each wind speed were obtained in this study. Furthermore, the rate of sea spray against total rainfall was estimated which showed decay curves for each wind speed. From both observations, rain and sea spray can be classified with a certain accuracy and obtained sea spray drop size distribution.

In Chapter 4, ship radar observation was conducted. Target of this observation was spatial distribution of rain and sea spray. The ship radar observation with vertical rotation detected sea spray and rainfall in the lower atmospheric boundary layer under three severe typhoon events. These events caused record maximum wind speed at Nanki-Shirahama AMeDAS station from 2006 to 2020. The maximum 10-minute averaged wind speed reached 39.5 ms^{-1}. The images obtained from ship radar were converted into physical quantities as backscattering radar cross section by calibration with neighboring meteorological radar and related algorithms proposed in this chapter. Furthermore, a method to estimate a profile of horizontal wind speeds and drag coefficient was proposed in this chapter. The vertical profile and the drag coefficient were calculated for each observed wind speed (20, 25, 30 and 40 ms^{-1}) at the observational tower.

In Chapter 5, the author proposed a conversion method for the number and mass concentration of sea spray using the backscattering radar cross section obtained from Chapter 4. The sensitivity analysis for several parameters

is conducted, related to the scattering phenomena which is the basic phenomena of radar observation. Wavelength and diameter, relative refractivity, and the number of terms are changed to reveal how many differences exist between Mie scattering and Rayleigh scattering. For rain and sea spray droplets, Mie scattering theory can be applied. Further investigation for volume scattering is conducted. The threshold of both scatterings is governed by the relationship between the distance of particles and wavelength. The distances of rain were calculated based on the drop size distribution results of previous studies. In this thesis, the volume scattering is represented as single scattering. Based on the algorithm, the author proposed a method to estimate concentration of sea spray for each height. The method represents the scattering by multiple particles in a unit volume (volume scattering) by combining individual scattering expressed by Mie theory in a unit volume. It is shown that the existing mass concentration distribution equation for suspended sediment in river can be applied to the obtained vertical distribution of mass concentration of sea spray, and an equation for the vertical distribution of mass concentration of sea spray depending on the wind speed is proposed. Furthermore, by using the vertical distribution of mass concentration, the amount of sea spray generated from the sea surface, which cannot be captured by radar due to sea clutter, is estimated and shown as a function of wind speed.

From the 1990s to present, numerous researchers have investigated the effects of sea spray and its drop size distribution through field observations and wind tunnel experiments. However, it is still difficult to observe sea spray itself because such severe conditions are often accompanied with rainfall. This thesis conducted three types of observations in the field and proposed new methodologies for each observational instrument. In the case of radar observation, scattering by sea spray was investigated because scattering phenomena are highly dependent on several parameters. This process have great significance for radar observation and it is also highly versatile. It is also possible that this method could be applied for other radars to observe different targets, such as a X-MP radar. These methods proposed in this thesis make radar observation possible to observe profiles of horizontal wind speed and profiles of concentration of sea spray simultaneously. To the author's great satisfaction, the knowledge gained in this study may help

elucidate a method for sea spray observations and improve the understanding of mass density profile of sea spray and wind speed profiles under severe weather conditions like typhoons.

7

Appendix

7.1 Scattering theorem of electro-magnetic wave: Mie scattering and Rayleigh scattering

The following derivation is based on Bohren and Huffman (1983)(24) and Matsuyama (2006)(53). These two documents explained the Mie theory well. The theory of scattering of electromagnetic waves by small particles is a fundamental problem. When considering electromagnetic waves, we use the Maxwell equations, which are the fundamental and the most beautiful equations of classical electromagnetism shown in **Eq**.(7.1)

$$\begin{aligned} \nabla \cdot \mathbf{D} &= \rho_F, \\ \nabla \times \mathbf{E} + \frac{\partial \mathbf{B}}{\partial \mathbf{t}} &= 0, \\ \nabla \cdot \mathbf{B} &= 0, \\ \nabla \times \mathbf{H} &= \mathbf{J_F} + \frac{\partial \mathbf{D}}{\partial \mathbf{t}}. \end{aligned} \tag{7.1}$$

where, $\mathbf{E}$ is electric field [N/C], $\mathbf{B}$ is magnetic induction [T] (Tesla), $\mathbf{D}$ is electric flux density [C m^{-2}], $\mathbf{H}$ is magnetic field [A m^{-1}]. The electric flux density and magnetic field are defined as following equations with using electric polarization $\mathbf{P}$ [C m^{-2}], maginetization $\mathbf{M}$[T], dielectric constatnt ϵ_0[F m^{-1}], permeability of vacuum μ_0[H m^{-1}]. Additionally, conductivity σ [S m^{-1}], permeability, electric susceptibility χ[-] are used these equations.

$$\mathbf{J_F} = \sigma \mathbf{E},$$

$$\mathbf{B} = \mu \mathbf{H},$$

$$\mathbf{P} = \epsilon_\mathbf{0} \chi \mathbf{E}.$$

Consider **Eq.** (7.1) and **Eq. Eq.4.2** in a vacuum and harmonic field. In other words, if we consider an electromagnetic wave oscillating at a single frequency,

the equation **Eq** (7.1) becomes

$$\nabla \cdot \epsilon_0 \mathbf{E} = 0,$$

$$\nabla \cdot \mathbf{H} = 0,$$

$$\nabla \times \mathbf{E} = i\omega\mu\mathbf{H},$$

$$\nabla \times \mathbf{H} = -i\omega\mu\mathbf{E}.$$

The scattered waves based on Mie scattering are obtained using Maxwell's equations in this vacuum and harmonic field.

Consider the situation where a spherical particle is placed in a vacuum and an electromagnetic wave is incident on it. Firstly, calculating curl of Maxwell's equation in a vacuum, then the third and fourth equations are

$$\nabla \times (\nabla \times \mathbf{E}) = i\omega\mu\nabla \times \mathbf{H} = \omega^{\mathbf{2}}\epsilon\mu\mathbf{E},$$

$$\nabla \times (\nabla \times \mathbf{H}) = i\omega\mu\nabla \times \mathbf{E} = \omega^{\mathbf{2}}\epsilon\mu\mathbf{H}.$$

With following vector formula,

$$\nabla \times (\nabla \times \mathbf{A}) = \nabla(\nabla \cdot \mathbf{A}) - \nabla \cdot (\nabla\mathbf{A}),$$

following vector wave equations are obtained.

$$\begin{aligned} \nabla^2\mathbf{E} + \mathbf{k}^{\mathbf{2}}\mathbf{E} &= \mathbf{0}, \\ \nabla^2\mathbf{H} + \mathbf{k}^{\mathbf{2}}\mathbf{H} &= \mathbf{0}. \end{aligned} \tag{7.2}$$

Here, $k^2 = \omega^2\epsilon\mu$, $\nabla^2\mathbf{A} = \nabla \cdot (\nabla\mathbf{A})$. For Mie scattering, the wave equation is transformed into a spherical coordinate system which has the origin at the center of a sphere and solved under the boundary condition that the electric and magnetic fields are continuous at the spherical surface.

The following vector functions is defined using arbitrary constant-valued vectors in terms of certain scalar functions.

$$\mathbf{M} = \nabla \times (\mathbf{c}\psi)$$

Here, the vector function $\mathbf{M}$ satisfies the following equation.

$$\nabla \cdot \mathbf{M} = \mathbf{0} \tag{7.3}$$

Furthermore, by using the following equation, which is a formula for vectors, we can obtain the relationship between the vector wave equation and the scalar wave equation using vector functions.

$$\begin{aligned} \nabla \times (\mathbf{A} \times \mathbf{B}) &= \mathbf{A}(\nabla \cdot \mathbf{B}) - \mathbf{B}(\nabla \cdot \mathbf{A}) + (\mathbf{B} \cdot \nabla)\mathbf{A} - (\mathbf{A} \cdot \nabla)\mathbf{B}, \\ \nabla(\mathbf{A} \cdot \mathbf{B}) &= \mathbf{A} \times (\nabla \times \mathbf{B}) + \mathbf{B} \times (\nabla \times \mathbf{A}) + (\mathbf{B} \cdot \nabla)\mathbf{A} + (\mathbf{A} \cdot \nabla)\mathbf{B}, \\ \nabla^2\mathbf{M} + \mathbf{k^2}\mathbf{M} &= \nabla \times [\mathbf{c}(\nabla^2\psi + \mathbf{k^2}\psi)]. \end{aligned} \tag{7.4}$$

This equation (7.4) is a vector wave equation, and comparing it with (7.2) leads to a scalar wave equation.

$$\nabla^2\psi + k^2\psi = 0$$

If we define the vector function $\mathbf{M}$ and the orthogonal vector function $\mathbf{N}$ as follows

$$\begin{aligned} \mathbf{N} &= \frac{\nabla \times \mathbf{M}}{\mathbf{k}}, \\ \nabla \cdot \mathbf{N} &= \mathbf{0}. \end{aligned} \tag{7.5}$$

The vector function $\mathbf{N}$ satisfies following vector function as well.

$$\nabla^2\mathbf{N} + \mathbf{k^2}\mathbf{N} = 0$$

Thus, both vector function $\mathbf{M}$ and $\mathbf{N}$ satisfy the orthogonality between electric field and magnetic field and are described as both of vector wave equation and scalar wave equation. In the Laplacian in the spherical coordinate system, then we obtained,

$$\nabla^2 = \frac{1}{r^2}\frac{\partial}{\partial r}\left(r^2\frac{\partial}{\partial r}\right) + \frac{1}{r^2\sin\theta}\frac{\partial}{\partial\theta}\left(\sin\theta\frac{\partial}{\partial\theta}\right) + \frac{1}{r^2\sin^2\theta}\frac{\partial^2}{\partial\phi^2}$$

is applied for scalar wave equation, then

$$\frac{1}{r^2}\frac{\partial}{\partial r}\left(r^2\frac{\partial\psi}{\partial r}\right) + \frac{1}{r^2\sin\theta}\frac{\partial}{\partial\theta}\left(\sin\theta\frac{\partial\psi}{\partial\theta}\right) + \frac{1}{r^2\sin^2\theta}\frac{\partial^2\phi}{\partial\psi^2} + k^2\psi = 0$$

Assuming this scalar equation is a separable equation, we obtain

$$\psi(r,\theta,\phi) = R(r)\Theta(\theta)\Phi(\phi).$$

Eq.7.1 and **Eq**.7.1, following three differential equations, noting that the partial derivative is in full differential notation since the variables have already been separated,

$$\begin{aligned} \frac{d^2\Phi}{d\phi^2} + m^2\Phi = 0, \\ \frac{1}{\sin\theta}\frac{d}{d\theta}\left(\sin\theta\frac{d\Theta}{d\theta}\right) + \left[n(n+1) - \frac{m^2}{\sin^2\theta}\right]\Theta = 0, \\ \frac{d}{dr}\left(r^2\frac{dR}{dr}\right) + [(k^2r^2 - n(n+1)]R = 0. \end{aligned} \tag{7.6}$$

Here, m, n are splitting constants. Considering the first differential equation in **Eq**.(7.7), the solution is

$$\Phi_e = \cos m\phi, \Phi_o = \sin m\phi. \tag{7.7}$$

The index of e, o represent even and odd. Since the scalar function is a function around the sphere, the function for the angle ϕ needs to be the same value by going around the circle. That is, the splitting constan m is integer or 0. Next, with $\eta = \cos\theta$ the second differential equation is

$$(1-\eta^2)\frac{d^2\Theta}{d\eta^2} - 2\eta\frac{d\Theta}{d\eta} + \left[n(n+1) - \frac{m^2}{1-\eta^2}\right]\Theta = 0.$$

This differential equation is Legendre's differential equation.

The only solution to this equation that does not diverge at $\eta = \pm(\theta = 0, \pi)$ is the Legendre function of the first kind,

$$\Theta = P_n^m(\eta) = P_n^m(\cos\theta), (m, n = 0, 1, 2, ...). \tag{7.8}$$

When $m = 0$, this becomes the Legendre polynomials of the first kind. Finally, about the third differential equation, with $kr = \rho$, $Z = R\sqrt{\rho}$, then this equation is

$$\rho\frac{d}{d\rho}\left(\rho\frac{dZ}{d\rho}\right) + [(\rho^2 - (n+\frac{1}{2})^2]Z = 0. \tag{7.9}$$

This is the Bessel's differential equation. The solution is defined as the Bessel function of the first kind J_v when $n + \frac{1}{2}$ in the equation is positive or negative, and the solution is defined as the Bessel function of the second kind Y_n when it is zero and independent of the Bessel function of the first kind. Followings are the equations,

$$j_n(\rho) = \sqrt{\frac{\pi}{2\rho}} J_{n+1/2}(\rho),$$
$$y_n(\rho) = \sqrt{\frac{\pi}{2\rho}} Y_{n+1/2}(\rho).$$

Spherical Bessel function satisfies the following asymptotic equations,

$$z_{n-1}(\rho) + z_{n+1}(\rho) = \frac{2n+1}{\rho} z_n(\rho),$$
$$(2n+1)\frac{d}{d\rho}(\rho) = n z_{n-1}(\rho) - (n+1) z_{n+1}(\rho),$$

where z_n is spherical Bessel function of j_n and y_n. Using following equations, solutions for high order spherical Bessel functions are obtained.

$$j_0(\rho) = \frac{\sin\rho}{\rho}, \quad j_1(\rho) = \frac{\sin\rho}{\rho^2} - \frac{\cos\rho}{\rho},$$
$$y_0(\rho) = -\frac{\cos\rho}{\rho}, \quad y_1(\rho) = -\frac{\cos\rho}{\rho^2} - \frac{\sin\rho}{\rho},$$

The solution of **Eq.**(7.9) also includes a linear combination of solutions of the spherical Bessel functions.

$$h_n^{(1)}(\rho) = j_n(\rho) + i y_n(\rho),$$
$$h_n^{(2)}(\rho) = j_n(\rho) - i y_n(\rho).$$

Since three solutions for all differential equations are obtained in above processes, solutions of scalar wave equation in polar coordinate systems are

$$\psi_{emn} = \cos m\phi P_n^m(\cos\theta) z_n(kr),$$
$$\psi_{omn} = \sin m\phi P_n^m(\cos\theta) z_n(kr).$$

Here, z_n represents four spherical Bessel function $j_n, y_n, h_n^{(1)}, h_n^{(2)}$. Furthermore, since the solution of vector wave equation satisfies **Eq**.(7.3), (7.5), then we obtain

$$\mathbf{M_{emn}} = \nabla \times (\mathbf{r}\psi_{\mathbf{emn}}), \quad \mathbf{M_{omn}} = \nabla \times (\mathbf{r}\psi_{\mathbf{omn}}),$$
$$\mathbf{M_{emn}} = \frac{\nabla \times \mathbf{M_{emn}}}{\mathbf{k}}, \quad \mathbf{N_{omn}} = \frac{\nabla \times \mathbf{M_{omn}}}{\mathbf{k}}.$$

The each vector can be represented as

$$\begin{aligned}
\mathbf{M_{emn}} =& \frac{-m}{\sin\theta}\sin m\phi P_n^m(\cos\theta) z_n(\rho)\hat{\mathbf{e}_\theta} \\
& - \cos m\phi \frac{dP_n^m(\cos\theta)}{d\theta} z_n(\rho)\hat{\mathbf{e}_\phi}, \\
\mathbf{M_{omn}} =& \frac{m}{\sin\theta}\cos m\phi P_n^m(\cos\theta) z_n(\rho)\hat{\mathbf{e}_\theta} \\
& - \sin m\phi \frac{dP_n^m(\cos\theta)}{d\theta} z_n(\rho)\hat{\mathbf{e}_\phi}, \\
\mathbf{N_{emn}} =& \frac{z_n(\rho)}{\rho}\cos m\phi n(n+1) P_n^m(\cos\theta)\hat{\mathbf{e}_\mathbf{r}} \\
& + \cos m\phi \frac{dP_n^m(\cos\theta)}{d\theta}\frac{1}{\rho}\frac{d}{d\rho}[\rho z_n(\rho)]\hat{\mathbf{e}_\theta} \\
& - m\sin m\phi \frac{P_n^m(\cos\theta)}{\sin\theta}\frac{1}{\rho}\frac{d}{d\rho}[\rho z_n(\rho)]\mathbf{e}_\phi, \\
\mathbf{N_{omn}} =& \frac{z_n(\rho)}{\rho}\sin m\phi n(n+1) P_n^m(\cos\theta)\hat{\mathbf{e}_\mathbf{r}} \\
& + \sin m\phi \frac{dP_n^m(\cos\theta)}{d\theta}\frac{1}{\rho}\frac{d}{d\rho}[\rho z_n(\rho)]\hat{\mathbf{e}_\theta} \\
& + m\cos m\phi \frac{P_n^m(\cos\theta)}{\sin\theta}\frac{1}{\rho}\frac{d}{d\rho}[\rho z_n(\rho)]\hat{\mathbf{e}_\phi}.
\end{aligned} \tag{7.10}$$

These solutions describe general solution of electro-magnetic wave in the spherical vector harmonic. Here, the characteristics of Bessel function are introduced. Bessel functions of the first and second kind expand into power series,

$$\begin{aligned}
j_n(z) =& (2z)^n \sum_{m=0}^{\infty} \frac{(-1)^m (n+m)!}{m!(2n+2m+1)!} z^{2m}, \\
y_n(z) =& -\frac{1}{2^n z^{n+1}}\Big[\sum_{m=0}^{n}\frac{(2n-2m)!}{m!(n-m)!}z^{2m} + (-1)^n \sum_{m=n+1}^{\infty}\frac{(-1)^m (m-n)!}{m!(2m-n)!}z^{2m}\Big].
\end{aligned}$$

Here, approximation is investigated when z asymptotes to zero. This asymptote means that electro-magnetic wave approaches the center of a sphere. Since the higher-order terms are sufficiently small that the first term is used to approximate, the equation is

$$j_n(z) \sim \frac{z^n}{(2n+1)!!},$$
$$y_n(z) \sim -\frac{(2n+1)!!}{z^{n+1}}.$$

In this case, spherical Hankel function is

$$\begin{aligned} h_n^{(1)}(z) &= j_n(z) + iy_n(z) \sim \frac{z^n}{(2n+1)!!} - i\frac{z^n}{(2n+1)!!}, \\ h_n^{(2)}(z) &= j_n(z) - iy_n(z) \sim \frac{z^n}{(2n+1)!!} + i\frac{z^n}{(2n+1)!!}. \end{aligned} \tag{7.11}$$

The only function that does not diverge to infinity is Bessel function of the first kind when z→0. Thus, Bessel function of the first kind is used to represent electro-magnetic wave approaching the center of the particle.

Hankel function of the first and second kind are described as,

$$h_n^{(1)}(z) = (-i)^{n+1}\frac{e^{iz}}{z}\sum_{r=0}^{n}\frac{(n+r)!}{r!(n-r)!}\Big(\frac{i}{2z}\Big)^r,$$
$$h_n^{(2)}(z) = i^{n+1}\frac{e^{-iz}}{z}\sum_{r=0}^{n}\frac{(n+r)!}{r!(n-r)!}\Big(\frac{-i}{2z}\Big)^r.$$

When z→ ∞, it is enough small to neglect the higher-order terms.

$$h_n^{(1)}(z) \sim (-i)^{n+1}\frac{e^{iz}}{z},$$
$$h_n^{(2)}(z) \sim i^{n+1}\frac{e^{-iz}}{z}.$$

When the exponent is negative, it represents a wave traveling toward the center with respect to the z-axis, and when it is positive, it represents a wave traveling outward from the center. Considering waves scattered from the center of a particle, the Hankel function of the first kind is the appropriate function. As the exponent is negative, it represents a wave traveling toward the center following the z-axis, and when it is positive, it represents a wave traveling outward from

the center. When considering waves scattered from the center of a particle, the Hankel function of the first kind is the appropriate function.

Next, we examine the orthogonality of functions. When we consider the functions of f and g, the products of f and g multiplied together and integrated over a certain interval is called the inner product of the function. When f and g are multiplied by a different function h and integrated over a certain interval, it is called the inner product weighted with h. If this value is zero, then f and g are orthogonal with h as the weight. The orthogonality of this function simplifies the calculations in the following paragraphs. We examine the orthogonality between each vector. First of all, the trigonometric functions $\sin m\phi$ and $\cos m'\phi$ are orthogonal in all combinations in the interval $(0,\ 2\ \pi)$ when m and m' are integers and $m \neq m'$. Thus,

$$\int_0^{2\pi} \sin m\phi \cos m'\phi d\phi = \int_0^{2\pi} \sin m\phi \sin m'\phi d\phi = \int_0^{2\pi} \cos m\phi \cos m'\phi d\phi = 0.$$

The vector in **Eq**.(7.11) becomes

$$\begin{aligned}\mathbf{M}_{em'n'} \cdot \mathbf{M}_{omn} \sin\theta \mathbf{d}\theta\mathbf{d}\phi &= \mathbf{N}_{omn} \cdot \mathbf{N}_{emn} \sin\theta \mathbf{d}\theta\mathbf{d}\phi \\ &= \mathbf{M}_{omn} \cdot \mathbf{N}_{omn} \sin\theta \mathbf{d}\theta\mathbf{d}\phi \\ &= \mathbf{M}_{emn} \cdot \mathbf{N}_{emn} \sin\theta \mathbf{d}\theta\mathbf{d}\phi.\end{aligned}$$

The orthogonality of the other combinations ($\mathbf{M}_{emn}$, $\mathbf{M}_{emn'}$) and ($\mathbf{N}_{emn}$, $\mathbf{N}_{emn'}$) is also investigated. The following integral values are obtained by calculating each vector element.

$$\begin{aligned}&\int_0^{2\pi}\int_0^{\pi} \mathbf{M_{emn}} \cdot \mathbf{M_{emn'}} \sin\theta \mathbf{d}\theta\mathbf{d}\phi \\ =& \int_0^{2\pi}\int_0^{\pi} \mathbf{M_{omn}} \cdot \mathbf{M_{omn'}} \sin\theta \mathbf{d}\theta\mathbf{d}\phi \\ &= m\int_0^{\pi} z_n z_{n'} \left(\frac{dP_n^m}{d\theta}\frac{dP_{n'}^m}{d\theta} + m^2 \frac{P_n^m P_{n'}^m}{\sin^2\theta}\right) \sin\theta d\theta\end{aligned} \tag{7.12}$$

Here,

$$\int_0^\pi \left(\frac{dP_n^m}{d\theta}\frac{dP_{n'}^m}{d\theta} + m^2\frac{P_n^m P_{n'}^m}{\sin^2\theta}\right)\sin\theta d\theta = \begin{cases} 0 & (n \neq m') \\ \frac{2n(n+1)(n+m)!}{(2n+1)(n-m)!} & (n = m'). \end{cases} \tag{7.13}$$

Therefore, ($\mathbf{M}_{emn}$, $\mathbf{M}_{emn'}$) and ($\mathbf{N}_{emn}$, $\mathbf{N}_{emn'}$) are orthogonal when $n \neq n'$.
The next step is to derive the plane wave in the spherical coordinate system. We assume that a plane wave is incident on a particle at the origin of the coordinates. The plane wave travels in the z direction, and the direction of displacement of the electric field is in the x direction. The incident electric-magnetic wave vector is,

$$\mathbf{E_i} = \mathbf{E_0 e^{ikz}}\hat{\mathbf{e_x}} = \mathbf{E_0 e^{ikr\cos\theta}}\hat{\mathbf{e_x}},$$

where

$$\hat{\mathbf{e_x}} = \sin\theta\cos\phi\hat{\mathbf{e_r}} + \cos\theta\cos\phi\hat{\mathbf{e}}_\theta - \sin\phi\hat{\mathbf{e}}_\phi.$$

This plane wave is expanded into a spherical coordinate system. That is, using the general solution for electro-magnetic wave in a spherical coordinate system, **Eq**.(7.10),

$$\mathbf{E_i} = \sum_{\mathbf{m=0}}^{\infty}\sum_{\mathbf{n=0}}^{\infty}(\mathbf{B}_{emn}\mathbf{M}_{emn} + \mathbf{B}_{omn}\mathbf{M}_{omn} + \mathbf{A}_{emn}\mathbf{N}_{emn} + \mathbf{A}_{omn}\mathbf{N}_{omn}). \tag{7.14}$$

Aforementioned, since the incident wave is finite at the origin, only Bessel function of the first kind can be used. Superscript (1) means the first kind. Also, comparing with the equation **Eq**.(7.14), we can only choose terms including $\cos\phi\hat{\mathbf{e}}_\phi$ and $\sin\phi\hat{\mathbf{e}}_\phi$ as terms of the function of ϕ. This means that plane wave can be described by only terms of $m_o^{(1)}$, $n_e^{(1)}$ when $m = 1$.

$$\mathbf{E_i} = \mathbf{E_0 e^{ikr\cos\theta}}\hat{\mathbf{e_x}} = \sum_{\mathbf{n=1}}^{\infty}(\mathbf{B_{oln}}\mathbf{M_{oln}^{(1)}} + \mathbf{A_{eln}}\mathbf{N_{eln}^{(1)}}).$$

Here, multiplying $\mathbf{M_{oln}^{(1)}} \sin\theta \mathbf{d}\theta\mathbf{d}\phi$ to obtain the coefficient B_{oln} and A_{eln} and integrating them, it becomes zero except terms $\mathbf{M_{oln}^{(1)}} \cdot \mathbf{M_{oln}^{(1)}}$ because of the orthogonality of functions. Then, we obtain following equation.

$$\begin{aligned} &\int_0^{\pi}\int_0^{2\pi} \mathbf{M_{oln}^{(1)}} \cdot \hat{\mathbf{e}}_\mathbf{x} \mathbf{e}^{\mathbf{ikr}\cos\theta} \sin\theta \mathbf{d}\theta\mathbf{d}\phi \\ =&\int_0^{\pi}\int_0^{2\pi} B_{oln}\mathbf{M_{oln}^{(1)}} \cdot \mathbf{M_{oln}^{(1)}} \sin\theta \mathbf{d}\theta\mathbf{d}\phi \end{aligned} \tag{7.15}$$

Expanding the left hand side,

$$\begin{aligned} &\int_0^{\pi}\int_0^{2\pi} \mathbf{M_{oln}^{(1)}} \cdot \hat{\mathbf{e}}_\mathbf{x} \mathbf{e}^{\mathbf{ikr}\cos\theta} \sin\theta \mathbf{d}\theta\mathbf{d}\phi \\ &\quad =\pi j_n(rk)\int_0^{\pi} e^{ikr\cos\theta}(\cos\theta P_n^1(\cos\theta) + \sin\theta \frac{d}{d\theta} P_n^1(\cos\theta) d\theta \\ &\quad =\pi j_n(kr)\int_0^{\pi} \frac{d}{d\theta}(\sin\theta P_n^1(\cos\theta)) e^{ikr\cos\theta} d\theta \end{aligned}$$

Here, Legendre function can be expressed by differentiation of Legendre polynomials.

$$P_n^m(\eta) = (1-\eta^2)^{m/2}\frac{d^m P_n(\eta)}{d\eta^m},$$

with $\eta = \cos\theta$

$$P_n^1 = -\sin\theta \frac{dP_n(\cos\theta)}{d\theta}.$$

P_n is the solution of Legendre function, the second differential equation, **Eq**.(7.7),

$$\frac{d}{d\theta}\left(\sin\theta \frac{dP_n(\cos\theta)}{d\theta}\right) = -n(n+1)P_n(\cos\theta)\sin\theta.$$

Then, the left hand side of **Eq**.(7.15) is

$$= \pi j_n(\rho) n(n+1)\int_0^{\pi} e^{ikr\cos\theta} P_n(\cos\theta)\sin\theta d\theta.$$

This integration is called as Gegenbauer's integral representation and giving

$$j_n(\rho) = \frac{(-i)^n}{2}\int_0^{\pi} e^{i\rho\cos\theta} P_n(\cos\theta)\sin\theta.$$

Thus, right hand side is

$$\pi(j_n(\rho))^2 \frac{2n(n+1)}{(-i)^n}.$$

Next, we expand the right hand side. From **Eq**.(7.12), (7.13)

$$M_{oln}^{(1)} \pi(j_n(\rho))^2 \frac{2n^2(n+1)^2}{2n+1}$$

Thus, the coefficient is derived as

$$B_{oln}^{(1)} = i^n \frac{2n+1}{n(n+1)}.$$

In the same way, the another coefficient is derived as

$$A_{eln}^{(1)} = -i^{n+1} \frac{2n+1}{n(n+1)}$$

Then, the plane wave of electro-magnetic wave in polar coordinate system is described as

$$\mathbf{E}_i = \mathbf{E}_0 \sum_{n=1}^{\infty} i^n \frac{2n+1}{n(n+1)} (\mathbf{M}_{oln}^{(1)} - i\mathbf{N}_{eln}^{(1)})$$

The magnetic field which is equivalent to this electric field is

$$\begin{aligned} \mathbf{H}_i &= \frac{1}{i\omega\mu} \nabla \times \mathbf{E_0} \\ &= \frac{-k}{\omega\mu} \sum_{n=1}^{\infty} i^n \frac{2n+1}{n(n+1)} (\mathbf{M}_{oln}^{(1)} + i\mathbf{N}_{eln}^{(1)}), \end{aligned}$$

where μ is magnetic permeability. Up to this point, we have been able to express the electric field E_0 and magnetic field H_0 of the incident plane wave in the spherical coordinate system.

Next, the electric field E_s and magnetic field H_s of the scattered light from the particle and inner electric and magnetic fields E_p, H_p are expressed as follows

when this electromagnetic wave is irradiated to the particle.

$$\begin{aligned}
\mathbf{E}_s &= -\sum_{n=1}^{\infty} i^n \frac{2n+1}{n(n+1)} (a_n \mathbf{M}_{oln}^{(3)} - i b_n \mathbf{N}_{eln}^{(3)}) \\
\mathbf{H}_s &= \frac{ik}{\omega\mu} \sum_{n=1}^{\infty} i^n \frac{2n+1}{n(n+1)} (b_n \mathbf{M}_{oln}^{(3)} - i a_n \mathbf{N}_{eln}^{(3)}) \\
\mathbf{E}_p &= \sum_{n=1}^{\infty} i^n \frac{2n+1}{n(n+1)} (c_n \mathbf{M}_{oln}^{(1)} - i d_n \mathbf{N}_{eln}^{(1)}) \\
\mathbf{E}_p &= \frac{-ik_p}{\omega\mu_p} \sum_{n=1}^{\infty} i^n \frac{2n+1}{n(n+1)} (d_n \mathbf{M}_{oln}^{(1)} + i c_n \mathbf{N}_{eln}^{(1)})
\end{aligned} \tag{7.16}$$

,where the subscript s and p represent scattering and inner particle. Also, (1) is Bessel function of the first kind and (3) is Hankel function of the first kind. The boundary condition to derive the coefficient for outer and inner scattering wave is continuity of electric field at the surface of a particle ($r = a$) and magnetic wave as well. Because of this condition, in the outer field of a particle there are incident and scattering electric field $E_{i\theta}, E_{s\theta}$ and in inner field of a particle, there is inner electric field $E_{p\theta}$.

$$\begin{aligned}
E_{i\theta} + E_{s\theta} = E_{i\theta}, \;\; E_{i\phi} + E_{s\phi} = E_{i\phi}, \\
H_{i\theta} + H_{s\theta} = H_{i\theta}, \;\; H_{i\phi} + H_{s\phi} = H_{i\phi}.
\end{aligned} \tag{7.17}$$

The size parameter x and relative refractivity m are defined as

$$x = ka = \frac{2\pi N a}{\lambda}, \;\; m = \frac{k_1}{k} = \frac{N_1}{N}.$$

Here, N and N_1 are complex refractivity of a particle and surrounding medium. Riccati-Bessel functions are described as

$$\begin{aligned}
\psi_n(\rho) = \rho j_n(\rho), \;\; \xi(\rho) = \rho h_n^{(1)}(\rho), \\
\psi_n^{'}(x) = \frac{d}{d\rho}\psi_n(\rho) \mid_{\rho=\alpha}, \;\; \xi_n^{'}(\alpha) = \frac{d}{d\rho}\xi_n \mid_{\rho=x},
\end{aligned}$$

and based on four boundary conditions, following equations are obtained.

$$\psi_n(x) - a_n\xi_n(x) = \frac{c_n}{m}\psi_n(mx)$$
$$\psi_n^{'}(x) - b_n\xi_n^{'}(x) = \frac{d_n}{m}\psi_n^{'}(mx)$$
$$\psi_n(x) - b_n\xi_n(x) = d_n\psi_n(mx)$$
$$\psi_n^{'}(x) - a_n\xi_n^{'}(x) = c_n\psi_n^{'}(mx)$$

Deriving each coefficient,

$$a_n = \frac{\mu m^2 j_n(mx)[xj_n(x)]' - \mu_1 j_n(x)[mxj_n(mx)]'}{\mu m^2 j_n(mx)[xh_n^{(1)}(x)]' - \mu_1 h_n^{(1)}(x)[mxj_n(mx)]'}$$
$$b_n = \frac{\mu_1 j_n(mx)[xj_n(x)]' - \mu j_n(x)[mxj_n(mx)]'}{\mu_1 j_n(mx)[xh_n^{(1)}(x)]' - \mu h_n^{(1)}(x)[mxj_n(mx)]'}$$
$$c_n = \frac{\mu_1 j_n(x)[xh_n(x)]' - \mu_1 h_n^{(1)}(x)[xj_n(x)]'}{\mu_1 j_n(mx)[xh_n^{(1)}(x)]' - \mu h_n^{(1)}(x)[mxj_n(mx)]'}$$
$$d_n = \frac{\mu_1 m j_n(x)[xh_n^{(1)}(x)]' - \mu_1 m h_n^{(1)}(x)[xj_n(x)]'}{\mu_1 m^2 j_n(mx)[xh_n^{(1)}(x)]' - \mu_1 h_n^{(1)}(x)[mxj_n(mx)]'}$$

Here, we obtained all coefficients in **Eq.**(7.17) and derived outer scattering wave and inner wave.

Next, we calculate the scattering efficiency and absorption efficiency of electromagnetic waves. Find the ratio of scattering W_s and the ratio of extinction W_{ext} of electromagnetic waves. Here, the ratio of absorption is $W_a = W_{ext} - W_s$.

$$W_{ext} = 1/2R_e \int_0^{2\pi}\int_0^{\pi} (\mathbf{E_{i\phi}H_{s\theta}} - \mathbf{E_{i\theta}H_{s\phi}} - \mathbf{E_{s\theta}H_{i\theta}H_{i\phi}} + \mathbf{E_{s\phi}H_{i\theta}})r^2 \sin\theta d\theta d\phi$$
$$W_s = 1/2R_e \int_0^{2\pi}\int_0^{\pi} (\mathbf{E_{s\theta}H_{s\theta}H_{s\phi}} + \mathbf{E_{s\phi}H_{s\theta}})r^2 \sin\theta d\theta d\phi \tag{7.18}$$

To derive each efficiency, following equation is shown.

$$\pi_n = \frac{P_n^1}{\sin\theta}, \quad \tau_n = \frac{dP_n^1}{d\theta}$$

The each incident wave in the equation is

$$E_{i\theta} = \frac{\cos\phi}{\rho}\sum_{n=1}^{\infty} E_n(\psi_n\pi_n - i\psi'_n\tau_n), \quad H_{i\theta} = \frac{k}{\omega\mu}\tan\phi E_{i\theta},$$
$$E_{i\phi} = \frac{\sin\phi}{\rho}\sum_{n=1}^{\infty} E_n(i\psi'_n\pi_n - \psi_n\tau_n), \quad H_{i\phi} = -\frac{k}{\omega\mu}\cos\phi E_{i\phi},$$

The scattering waves are

$$\begin{aligned}
E_{s\theta} &= \frac{\cos\phi}{\rho}\sum_{n=1}^{\infty} E_n(ia_n\xi'_n\tau_n - b_n\xi_n\pi_n),\\
E_{s\phi} &= \frac{\sin\phi}{\rho}\sum_{n=1}^{\infty} E_n(b_n\xi_n\tau_n - ia_n\xi'_n\pi_n),\\
H_{s\theta} &= \frac{k}{\omega\mu}\frac{\sin\phi}{\rho}\sum_{n=1}^{\infty} E_n(ib_n\xi'_n\tau_n - a_n\xi_n\pi_n),\\
H_{s\phi} &= \frac{k}{\omega\mu}\frac{\cos\phi}{\rho}\sum_{n=1}^{\infty} E_n(ib_n\xi'_n\pi_n - a_n\xi_n\tau_n).
\end{aligned} \tag{7.19}$$

Using Eq. **Eq**.(7.19), the scattering rate in **Eq**.(7.18) can be expressed as the following infinite series

$$W_s = \frac{\pi \mid E_0 \mid^2}{k\omega\mu}\sum_{n=1}^{\infty}(2n+1)\mathbf{R_e}(g_n)(\mid a_n \mid^2 + \mid b_n \mid^2),$$

where, g_n is

$$g_n = (\chi_n\psi'_n - \psi_n\chi'_n) - i(\psi_n\psi'_n + \chi_n\chi'_n).$$

Using Riccati-Bessel function χ_n and Ronski determinant,

$$\chi_n\psi'_n - \psi_n\chi'_n = 1,$$

scattering coefficient is

$$C_{sca} = \frac{W_s}{I_i} = \frac{2\pi}{k^2}\sum_{n=1}^{\infty}(2n+1)(\mid a_n \mid^2 + \mid b_n \mid^2).$$

Extinction coefficient is same as well,

$$C_{ext} = \frac{W_{ext}}{I_i} = \frac{2\pi}{k^2}(2n+1)\mathbf{R_e}(a_n + b_n).$$

This is the scattering wave and scattering cross section based on Mie's theory. To describe Rayleigh scattering, the size parameter x becomes less than 1. Thus, the first order of Mie coefficient a_n and b_n is only considered. In the case of that, scattered light intensity is

$$I_s = \frac{8\pi^4 N a^6}{\lambda^4 r^2} \mid \frac{m^2 - 1}{m^2 + 2} \mid^2 (1 + \cos^2\theta) I_i.$$

Furthermore, the backscattered wave is the one that is 180 degrees opposite to the direction of the incident wave, and the backscattering cross section is

$$C_b = \frac{W_b}{I_i} = \frac{2\pi}{k^2} \mid \sum_n (2n+1)(-1)^n (a_n - b_n) \mid^2 \tag{7.20}$$

Mie scattering theory represents scattering of electromagnetic waves by a single spherical particle, as mentioned above.

References

[1] 2

[2] Zhuang B. Li M. Lu Y. An, N. and Z. G. Wang. Combined theoretical and experimental study of refractive indices of water-acetonitrile-salt systems. The Journal of Physical Chemistry B, Vol. 119, No. 33, pp. 10701–10709, 2015. 121

[3] E. L. Andreas. Sea spray and the turbulent air-sea heat fluxes. J. Geophys. Res., Vol. 97, No. C3, pp. 11429–11441, 1992. 21, 52, 58

[4] E. L. Andreas. The temperature of evaporating sea spray droplets. J. Atmos. Sci., Vol. 52, No. 7, pp. 852–862, 1995. 52

[5] E. L. Andreas. A new sea spray generation function for wind speeds up to 32 m s − 1. J. Phys. Oceanogr., Vol. 28, No. 11, pp. 2175–2184, 1998. 8, 17, 42, 52, 58

[6] E. L. Andreas. Spray stress revisited. Journal of Physical Oceanography, Vol. 34, pp. 1429–1440, 2004. 13, 16, 23, 28, 41

[7] E. L. Andreas and J. Decosmo. The signature of sea spray in the hexos turbulent heat flux data. Boundary-layer meteorology, Vol. 103, No. 2, pp. 303–333, 2002. 21

[8] E. L. Andreas and K. A. Emanuel. Effects of sea spray on tropical cyclone intensity. Journal of the atmospheric sciences, Vol. 58, No. 24, pp. 3741–3751, 2001. 16, 17

[9] Edson J. B. Monahan E. C. Rouault M. P. Andreas, E. L. and S. D. Smith. The spray contribution to net evaporation from the sea: A review of recent progress. Boundary-Layer Meteorology, Vol. 72, No. 1, pp. 3–52, 1995. 5, 6, 10, 31

[10] Mahrt L. Andreas, E. L. and D. Vickers. An improved bulk air-sea surface flux algorithm, including spray- mediated transfer. Quart. J. Roy. Meteor. Soc., Vol. 141, No. 687, pp. 642–654, 2016. 50

[11] G. I. Barenblatt. Scaling, self-similarity, and intermediate asymptotics. Cambridge Univ. Press, 1996. 18

[12] G. I. Barenblatt. The 1999 james lighthill memorial paper: Scaling laws for turbulent wall-bounded shear flows at very large reynolds numbers. Journal of engineering mathematics, Vol. 36, No. 4, pp. 361–381, 1999. 21

[13] G. I. Barenblatt, A. J. Chorin, and V. M. Prostokishin. A note concerning the lighthill "sandwich model" of tropical cyclones. The National Academy of Sciences of the USA, No. 32. 14, 21

[14] Chorin A. J. Goldenfeld N. Bertsch, M. and J. L. Vázquez. G.i. barenblatt in memoriam (1927-2018). EMS Newsletter, Vol. 9, No. 109, pp. 33–38, 2018. 21

[15] P. G. Black, E. A. D'Asaro, W. M. Drennan, J. R. French, P. P. Niiler, T. B. Sanford, E. J. Terrill, E. J.and Walsh, and J. A. Zhang. Air-sea exchange in hurri- canes: Synthesis of observations from the coupled boundary layer air-sea transfer experiment. Bull. Amer. Soc., Vol. 88, No. 3, pp. 357–374, 2007. 3

[16] W. L. Peirson W. Asher C. W. Fairall, M. L. Banner and R. P. Morison. Investigation of the physical scaling of sea spray spume droplet production. Journal of Geophysical Research, Vol. 114, No. C10001. 3

[17] D. R. Caldwell and W. P. Elliott. Surface stresses produced by rainfall. Journal of Physical Oceanography, Vol. 1, No. 2, pp. 145–148, 1971. 24, 25, 28, 50

[18] D. R. Caldwell and W. P. Elliott. The effect of rainfall on the wind in the surface layer. Bound.-Layer Meteor., Vol. 3, pp. 146–151, 1972. 24, 25, 28, 50

[19] A. H. Callaghan. 52

[20] L. Cavaleri, L. Bertotti, and J.R. Bidlot. 51

[21] H. Charnock. Wind stress on a water surface. Q.J.R. Meteorol. Soc., Vol. 81, pp. 639–640, 1955. 17

[22] D. G. Crighton. Sir james lighthill. Journal of Fluid Mechanics, Vol. 386, pp. 1–3, 1999. 21

[23] K. A. Emanuel. The behavior of a simple hurricane model using a convective scheme based on subcloud-layer entropy equilibrium. Journal of Atmospheric Sciences, Vol. 52, No. 22. 3, 14

[24] Bohren C. F. and D. R. Huffman. Absorption and Scattering of Light by Small Particles. John Wiley, New York, NY, 1983. 152

[25] Edson J. B. FairalI, C. W. and M. A. Miller. Heat fluxes, whitecaps, and sea spray. in G. L. Geernaert and W. J. Plant (eds.), Surface Waves and Fluxes, Vol. 1, No. Kluwer, Dordrecht,, pp. 173–208, 1990. 6

REFERENCES

[26] C. W. Fairall, J. D. Kepert, and G. J. Holland. The effect of sea spray on surface energy transports over the ocean. Global Atmos. Ocean Syst., Vol. 2, No. 2-3, pp. 121–142, 1994. 6, 8, 13, 21, 42

[27] E. J. Førland and I. Hanssen-Bauer. Increased precipitation in the norwegian arctic: True or false? Clim. Chang., Vol. 46, pp. 485–509, 2000. 55

[28] K. Friedrich, S. Higgins, F. J. Masters, and C. R. Lopez. Articulating and stationary parsivel disdrometer measurements in conditions with strong winds and heavy rainfall. Journal of Atmospheric and Oceanic Technology, Vol. 30, No. 9, pp. 2063–2080, 2013. 41, 46

[29] K. Friedrich, E. A. Kalina, F. J. Masters, and C. R. Lopez. Drop-size distributions in thunderstorms measured by optical disdrometers during vortex2. Monthly Weather Review, Vol. 141, No. 4, pp. 1182–1203, 2013. 44, 45, 48

[30] Harald T. Friis. A note on a simple transmission formula. Proceedings of the IRE, Vol. 34, No. 5, pp. 254–256, 1946. 86

[31] Y. Fujiyoshi. 名古屋大学水圏科学研究所と北海道大学低温科学研究所の気象レーダー観測 (気象レーダー 60 年の歩みと将来展望) – (大学における気象レーダーの研究・利用. 気象研究ノート, Vol. 237, pp. 84–93, 2018. 79

[32] B. E. Gelfand. Droplet breakup phenomena in flows with velocity lag. Energy Combust. Sci., Vol. 22, No. 3, pp. 201–265, 1996. 52

[33] R. Gunn and G. D. Kinzer. The terminal velocity of fall for water droplets in stagnant air. Journal of Atmospheric Sciences, Vol. 6, No. 4, pp. 243–248, 1949. 27, 44

[34] L. Hasse, M. Grossklaus, K. Uhlig, and P. Timm. A ship rain gauge for use in high wind speeds. Journal of Atmospheric and Oceanic Technology, Vol. 15, No. 2, pp. 380–386, 1998. 49

[35] A. J. Illingworth and C. J. Stevens. An optical disdrometer for the measurement of raindrop size spectra in windy conditions. Journal of Atmospheric and Oceanic Technology, Vol. 4, No. 3, pp. 411–421, 1987. 41

[36] S. A. Michlson J.-W. Bao, C. W. Fairall and L. Bianco. Parameterizations of sea-spray impact on the air-sea momentum and heat fluxes. Monthly Weather Review, Vol. 139, pp. 3781–3797, 2011. 3, 14

[37] J. Jaffrain and A. Berne. Experimental quantification of the sampling uncertainty associated with measurements from parsivel disdrometers. Journal of Hydrometeorology, Vol. 12, No. 3, pp. 352–370, 2011. 45

[38] Japan Meteorological Agency (JMA). Available online:, 2020. http://www.jma.go.jp/en/amedas (accessed on 5 November 2020. 53

[39] I. S. F. Jones and Y. Toba. Wind stress over the ocean. Cambridge Univ. Press, 2001. 18

[40] Smith S. D. Katsaros, K. B. and W. A. Oost. Hexos—humidity exchange over the sea a program for research on water-vapor and droplet fluxes from sea to air at moderate to high wind speeds. Bulletin of the American Meteorological Society, Vol. 68, No. 1, pp. 466–476, 1987. 6

[41] O. Kazuo. Principles of synthetic aperture radar for remote sensing. Tokyo Denki University Press, 2009. 86, 87

[42] T. Kimura, T. Maruyama, and T. Ishimaru. Spc-iii no sekkei to seisaku. Proc. Cold Reg. Technol. Conf., Vol. 19, pp. 665–670, 1993. 53, 54

[43] W. G. Large and S. Pond. Open ocean momentum flux measurements in moderate to strong winds. Journal of physical oceanography, Vol. 11, No. 3, pp. 324–336, 1981. 13

[44] Dominique Baillis Leonid A. Dombrovsky. Thermal radiation in disperse systems: An engineering approach. begell house, 2010. 82, 121, 125, 130

[45] E. R. Lewis, R. Lewis, K. E. Karlstrom, E. R. Lewis, and S. E. Schwartz. Sea salt aerosol production: mechanisms, methods, measurements, and models, Vol. 152. American Geophysical Union, 2004. 52

[46] J. Lighthill. Ocean spray and the thermodynamics of tropical cyclones. Journal of Engineering Mathematics, Vol. 35, pp. 11–42, 1999. 7, 14, 18

[47] B. Liu, C. Guan, and Xie L. The wave state and sea spray related parameterization of wind stress applicable from low to extreme winds. J. Geophys. Res., Vol. 117, No. C11, pp. 1429–1440, 2012. 18

[48] Davidson N. E. Xiao Y. Ma, Y. and J. W. Bao. Revised parameterization of air-sea exchanges in high winds for operational numerical prediction: Impact on tropical cyclone track, intensity, and rapid intensification. Weather and Forecasting, Vol. 32, No. 3, pp. 821–848, 2017. 3

[49] V. K. Makin. A note on the drag of the sea surface at hurricane winds. Boundary-Layer Meteorology, Vol. 115, pp. 169–176, 2005. 18, 19

[50] R. Marks. 51, 53

[51] P. Markuszewski, Z. Klusek, E. D. Nilsson, and T. Petelski. Observations on relations between marine aerosol fluxes and surface-generated noise in the southern baltic sea. Oceanologia, Vol. 62, No. 4, Part A, pp. 413–427, 2020. 52

[52] J. S. Marshall and W. M. Palmer. The distribution of raindrops with size. Journal of Meteorology, Vol. 5, pp. 165–166, 1948. 27, 28, 40, 46, 48, 50, 51

[53] T. Matsuyama. Derivation of mie theory of light scattering. J. Soc. Powder Technol., Vol. 43, No. 2, pp. 115–124, 2006. 152

[54] A. A. Maur. Statistical tools for drop size distributions: Moments and generalized gamma. Journal of the atmospheric sciences, Vol. 58, No. 4, pp. 407–418, 2001. 50

[55] M. Mikami, Y. Yamada, M. Ishizuka, T. Ishimaru, W. Gao, and F. Zeng. Measurement of saltation process over gobi and sand dunes in the taklimakan desert, china, with newly developed sand particle counter. J. Geophys. Res. Atmos., Vol. 110, No. D18, 2005. 54

[56] E. C. Monahan. 8, 21, 42, 51

[57] J. A. Mueller and F. Veron. A sea state-dependent spume generation function. J. Phys. Oceanogr., Vol. 39, No. 9, pp. 2363–2372, 2009. 52, 58

[58] K. Nishimura. Measurement of blowing snow. J. Fluid Mech., Vol. 28, No. 6, pp. 455–460, 2009. 54

[59] S. J. Norris, I. M. Brooks, M. K. Hill, B. J. Brooks, M. H. Smith, and D. A. Sproson. Eddy covariance measurements of the sea spray aerosol flux over the open ocean. J. Geophys. Res. Atmos., Vol. 117, No. D7, 2012. 52

[60] T. Ozeki, T. Shiga, J. Sawamura, Y. Yashiro, S. Adachi, and Hajime Y. Development of sea spray meters and an analysis of sea spray characteristics in large vessels. Paper presented at the The 26th International Ocean and Polar Engineering Conference, Rhodes, Greece, Vol. 1, pp. 1335–1340, 2016. 54

[61] T. Ozeki, S. Toda, and H. Yamaguchi. Field investigation of impinging seawater spray on the r/v mirai using spray particle counter type sea spray meter. In Proceedings of the 33rd International Symposium on Okhotsk Sea and Polar Oceans, Hokkaido, Japan, Vol. 5, pp. 93–96, 2018. 54

[62] M. D. Powell, P. J. Vickery, and T. A. Reinhold. Reduced drag coefficient for high wind speeds in tropical cyclones. Nature, Vol. 422, pp. 279–283, 2003. 7, 13, 14, 15, 18, 20, 28, 29, 50

[63] M.D. Powell. New findings on hurricane intensity, wind field extent, and surface drag coefficient behavior. Tenth international workshop on wave hindcasting and forecast- ing and coastal hazard symposium, North Shore, Oahu, Hawaii, 1988. 18, 28

[64] H. R. Pruppacher and J. D. Klett. Microphysics of Clouds and Precipitation. Springer Science & Business Media, 2012. 40

[65] V. Raizer. Microwave scattering model of sea foam. 2012 IEEE International Geoscience and Remote Sensing Symposium, pp. 5836–5839, 2012. 121, 125, 126

[66] V. Raizer. Radar backscattering from sea foam and spray. 2013 IEEE International Geoscience and Remote Sensing Symposium - IGARSS, pp. 4054–4057, 2013. 121, 125, 126

[67] Hachani S, Boudevillain B, Delrieu G, and Bargaoui Z. 51

[68] M. E. Salter, E. D. Nilsson, A. Butcher, and M. Bilde. On the seawater temperature dependence of the sea spray aerosol generated by a continuous plunging jet. J. Geophys. Res. Atmos., Vol. 119, pp. 9052–9072, 2014. 52

[69] A. Sato. Calculation of size-effect of blowing snow particles on the snow particle counter (first report). 54

[70] R. A. Schmidt. A system that measures blowing snow, Vol. 194. Department of Agriculture, Forest Service, Rocky Mountain Forest and Range Experiment Station, 1977. 54

[71] R. A. Schmidt, M. Roland, and G. Hansueli. Comparison of snow drifting measurements at an alpine ridge crest. Cold Reg. Sci. Technol., Vol. 9, No. 2. 54

[72] M.A. Serio, F.G. Carollo, and V. Ferro. 48, 51

[73] Alan Shapiro. Drag-induced transfer of horizontal momentum between air and raindrops. Journal of the atmospheric sciences, Vol. 62.7, pp. 2205–2219, 2005. 28

[74] J. Skaar. On the measurement of precipitation at sea. J. Griegs boktr.; I kommisjon hos J. Dybwad, Oslo, 1955. 49, 50

[75] P. M. Park Smith, M. H. and I. E. Consterdine. Marine aerosol concentrations and estimated fluxes over the sea. Quart. J. Roy. Meteor. Soc., Vol. 119, pp. 809–824, 1993. 8, 42

[76] S.D. Smith. Coefficients for sea surface wind stress, heat flux, and wind profiles as a function of wind speed and temperature. Journal of Geophysical Research, Vol. 93, No. 12, pp. 15467–15472, 1988. 12

[77] A. Soloviev and R. Lukas. Effects of bubbles and sea spray on air-sea exchange in hurricane conditions. Boundary Layer Meteorol., Vol. 136, pp. 365–376, 2010. 13, 14

REFERENCES

[78] Lukas R. Donelan M. A. Haus B. K. Soloviev, A. V. and I. Ginis. The air-sea interface and surface stress under tropical cyclones. Scientific reports., Vol. 4, No. 1, pp. 1–6, 2014. 14

[79] K. Sugiura, K. Nishimura, N. Maeno, and T. Kimura. Measurements of snow mass flux and transport rate at different particle diameters in drifting snow. 54

[80] M. Thurai and V. N. Bringi. Application of the generalized gamma model to represent the full rain drop size distribution spectra. Journal of Applied Meteorology and Climatology, Vol. 57, No. 5, pp. 1197–1210, 2018. 50

[81] Iida N. Kawamura H. Ebuchi N. Toba, Y. and I. S. Jones. Wave dependence of sea-surface wind stress. Journal of Physical Oceanography, Vol. 20, No. 5, pp. 705–721, 1990. 18

[82] Y. Toba. Local balance in the air-sea boundary processes. Journal of the Oceanographical Society of Japan, Vol. 28, pp. 109–120, 1972. 19

[83] Ezhova E. Soustova I. Troitskaya, Y. and S. Zilitinkevich. On the effect of sea spray on the aerodynamic surface drag under severe winds. Ocean Dynamics, Vol. 66, No. 5, pp. 659–669, 2016. 23

[84] S. Tsuchiya, H. Yamaji, and M. Kawasaki. Xrain 雨量観測の実用化技術に関する検討資料. 国土技術政策総合研究所資料, p. 10.264, 2016. 87

[85] C. W. Ulbrich. Natural variations in the analytical form of the raindrop size distribution. Journal of Applied Meteorology and Climatology, Vol. 22, No. 10. 40, 46, 48, 50, 51

[86] F. Veron. Ocean spray. Annual Review of Fluid Mechanics, Vol. 47, No. 1, pp. 507–538, 2015. 5, 6, 17, 52

[87] Li L. Wu Z. Chen J. Wan, Z. and X. Lu. The impact of ocean waves on spray stress and surface drag coefficient. International Journal of Numerical Methods for Heat and Fluid Flow, 2019. 17, 21, 22, 23, 28

[88] J. Wu. Production of spume drops by the wind tearing of wave crests: The search for quantification. J. Geophys. Res., Vol. 98, No. 18, pp. 18 221–18 227, 1993. 8, 42

[89] H. Yamamoto, K. Sakamoto, K. Iwaya, E. Kawamoto, M. Nasu, and Y. Watanabe. Characteristics of meteorological and salt damage by typhoon no.24 in 2018 (trami). J. JSNDS, Vol. 37, No. 4, pp. 365–382, 2019. (in Japanese). 50

[90] S. E. Yuter and W. S. Parker. Rainfall measurement on ship revisited: The 1997 pacs tepps cruise. Journal of Applied Meteorology, Vol. 40, No. 6, pp. 1003–1018, 2001. 49, 50

[91] 稲垣達弘建設部 菅原庸平. 乙部岳 c バンド mp レーダの冬季観測仰角の検討. 第 63 回 (2019 年度) 北海道開発技術研究発表会論文, 2019. 88

[92] 合田良実. 極値統計における異常値の棄却基準とその応用. 土木学会論文集, Vol. 417, pp. 245–254, 1990. 95

[93] 上野誠松尾稔. 構造物の耐用期間内に生起する外力の不確実性を考慮した信頼性設計法. 土木学会論文報告集, Vol. 289, pp. 89–98, 1979. 95